Dissertation zur Erlangung des Doktorgrades
der Fakultät für Chemie und Pharmazie
an der Ludwig-Maximilians-Universität München

Molecular force analysis of the vertebrate kinetochore protein CENP-T

Andrea Katharina Freikamp
aus Frankfurt/Main, Deutschland

2017

Erklärung

Diese Dissertation wurde im Sinne von § 7 der Promotionsordnung vom 28. November 2011 von Herrn Prof. Dr. Klaus Förstemann betreut.

Eidesstattliche Versicherung

Diese Dissertation wurde eigenständig und ohne unerlaubte Hilfe erarbeitet.

München, den 4.9.2017

Andrea Freikamp

Dissertation eingereicht am 5.9.2017
Erstgutachter: Prof. Dr. Klaus Förstemann
Zweitgutachter: PD Dr. Günther Woehlke
Mündliche Prüfung am 18.10.2017

Contents

Abstract

Mitosis is one of the most fundamental processes of life and critically depends on mechanical forces. Forces are not only essential to segregate sister chromatids towards the spindle poles, but also play an important role already during spindle formation. As initial contacts between spindle microtubules and kinetochores are established stochastically, incorrect attachments have to be dismantled, while correctly bi-oriented attachments are selectively stabilized.

In vitro data demonstrated that kinetochore–microtubule attachments are stabilized by forces in the single pico-Newton (pN) range. Indirectly, this effect has been observed as early as in the 1960$^{\text{th}}$ by Bruce Nicklas during his pioneering microneedle studies on grasshopper spermatocytes. The molecular details of force propagation during mitosis *in vivo*, however, remained elusive because suitable methods to measure force transduction directly at the relevant subcellular structures have been missing.

In recent years, the development of genetically encoded Förster resonance energy transfer (FRET) based tension sensor modules (TSMs) closed this gap by allowing force measurements across distinct molecules in living cells. By the time this project was initiated, three single molecule calibrated TSMs were available in our group. Two of them, namely the F40 and HP35 modules sensitive forces between 1–6 and 6–8 pN, respectively, were integrated into the kinetochore protein centromere protein T (CENP-T); furthermore, image analysis procedures based on custom written Matlab software were established. Expression and analysis of these two biosensors in chicken DT40 CENP-T knockdown cells demonstrated that CENP-T indeed experiences mechanical force during metaphase. Combination of the two sensors further suggested that these forces do not exceed 6 pN; however, no statement could be made about the lower limit due to the gradual response characteristics of the F40 TSM.

To analyze CENP-T force transduction in more detail, new potential TSMs with increased sensitivity in the lower single pN force range were engineered and analyzed. The most promising results were obtained using a previously designed ferredoxin-like (FL) peptide. Single molecule calibration of the new TSM confirmed reversible unfolding at forces of 3–5 pN; furthermore, the new probe displayed the sharpest force response and highest sensitivity of all calibrated TSMs reported thus far.

Applied to CENP-T, the new sensor revealed that the protein experiences forces of at least 3 pN, suggesting a role of CENP-T as mechanical force coupler during cell division.

Zusammenfassung

Die Teilung einer Zelle durch Mitose ist einer der grundlegendsten Prozesse allen Lebens. Mechanische Kräfte spielen dabei eine entscheidende Rolle, und zwar nicht erst beim Transport der zovor separierten Schwesterchromatiden zu den Spindelpolen. Schon der Aufbau der mitotischen Spindel selbst wird entscheidend durch mechanische Feedback-Loops beeinflusst, wodurch fehlerhafte Verbindungen zwischen Mikrotubuli und Kinetochor selektiv eliminiert und korrekte erhalten werden.

In vivo Daten zeigten, dass Bindungen zwischen Kinetochor und Mikrotubuli direkt durch Kräfte im einstelligen pico-Newton (pN) Bereich verstärkt werden. Bruce Nicklas hat dieses Phänomen bereits in den 1960er Jahren indirekt in Grashüpfer-Spermatozyten entdeckt. Dennoch blieben die dafür verantwortlichen molekularen Mechanismen lange Zeit unbekannt, da geeignete Techniken zu ihrer Erforschung fehlten.

Diese Lücke wurde vor einigen Jahren durch die Entwicklung genetisch kodierter molekularer Kraftsensoren geschlossen. Diese auf Förster Resonanz Energietransfer (FRET) basierenden Sensoren können direkt in das zu untersuchende Protein eingebaut und in lebenden Zellen analysiert werden. Zu Beginn der hier vorliegenden Arbeit standen in unserem Labor drei kalibrierte Kraftsensoren zur Verfügung, von denen zwei im Rahmen des Projekts verwendet wurden, nämlich der F40 Sensor mit einer Sensitivität von 1–6 pN und der HP35 Sonsor, welcher Kräfte von 6–8 pN misst. Beide Module wurde in das Kinetochor Protein CENP-T eingebaut und mikroskopisch ausgewertet. Die Analyse der Sensoren mit eigens dafür entwickelter Software zeigte, dass CENP-T während der Metaphase tatsächlich unter mechanischer Kraft steht, welche jedoch 6 pN nicht übersteigt. Aufgrund des breiten durch F40 abgedeckten Kraftspektrums konnte jedoch keine Aussage über einen unteren Schwellenwert getroffen werden.

Um die Kräfte über CENP-T noch besser auflösen zu können, wurden mehre potentielle neue Sensormodule entwickelt und analysiert. Die besten Resultate lieferte ein bereits in anderem Kontext verwendetes artifizielles Peptid, welches einer Ferredoxin-like (FL)-Domäne ähnelt. Die Kalibrierung des neuen Sensors zeigte eine reversible Entfaltung des Peptids im Bereich von 3–5 pN und ein sehr scharfes Sensitivitätsprofil.

Angewendet in CENP-T konnte mit dem neuem Sensor gezeigt werden, dass die Kräfte während der Metaphase Werte von 3 pN überschreiten und CENP-T somit eine aktive Rolle bei der Krafübertragung während der Mitose spielt.

List of Figures

List of Tables

Abbreviations

aa	amino acid
AFM	atomic force microscopy
bp	base pair
CCAN	constitutive centromere assiciated network
CD	circular dichroism
CDK 1	cyclin B–dependent protein kinase 1
cDNA	complementary DNA
CENP-C	centromere protein C
CENP-T	centromere protein T
CH	calponin homology
CI	confidence interval
CLSM	confocal laser scanning microscope
ConA	Concanavalin A
DNA	deoxyribonucleic acid
ECM	extracellular matrix
EM	electron microscopy
EMT	epithelial-mesenchymal transition
FA	focal adhesion
FL	ferredoxin-like fold
FLIM	fluorescence-lifetime imaging microscopy
FRET	Förster resonance energy transfer
F40	flagelliform
G418	geneticin
HP35	villin headpiece
HP35st	stable villin headpiece
kb	kilo base/kilo bases
KT	kinetochore
kMT	kinetochore microtubule

KT–TS	kinetochore–tension sensor
MCS	multiple cloning site
Mb	Mega base/Mega bases
MT	microtubule
MS	mass spectrometry
NA	numerical aperture
NaCl	sodium chloride
NE	nuclear envelope
NMR	nuclear magnetic resonance
o/n	over night
PCR	polymerase chain reaction
pN	pico Newton
POI	protein of interest
RFP	red fluorescent protein
RNA	ribonucleic acid
ROI	region of interest
RT	room temperature
SAC	spindle assembly checkpoint
SD	standard deviation
SEM	standard error of the mean
siRNA	small interfering RNA
TEM	transmission electron microscopy
tet	tetracycline
TS	tension sensor
TSM	tension sensor module
WLC	worm-like chain
wt	wild type

1 Introduction

1.1 Mechanobiology: Omnipresent, yet long neglected

Being constantly subjected to mechanical forces such as gravity is an integral part of our lives, and yet usually evades our consciousness. Moreover, we take it for granted that not only animals, but also single-cell organisms and plants have the ability to change shape or move through the environment. This ability to produce, sense, and respond to mechanical stimuli is a fundamental property of life and has been connected to physiological processes such as development and homeostasis, as well as to pathological processes and disease.

One of the most obvious examples of mechanobiology is active force generation by skeletal, striated, and smooth muscle tissues [Ross and Pawlina, 2006]. On smaller scale, individual cells or small groups of cells can migrate by remodeling their cytoskeleton, as for example seen during gastrulation, wound healing, leukocyte extravasation, or tumor metastasis [Freikamp et al., 2017]. Going one step deeper into the cell, vesicles and molecules are actively transported by a multitude of molecular motors of the myosin, kinesin, and dynein families [Alberts et al., 2007]. And last but not least, cell division requires active separation of the duplicated deoxyribonucleic acid (DNA) and all intracellular content as well as constriction and fission of the plasma membrane.

Alongside active force generation as described above, tissues and organs need to withstand externally applied forces such as shear stress at the skin, hydrostatic pressure within the cardiovascular system, or compression of bones and joints during physical activity. Interestingly, the molecular structures mediating robustness towards these external forces are no mere passive complexes but dynamic and active structures with the ability to adapt to their environment. Examples include the thickening of the skin on our hands and feet, but even seemingly "dead" tissues like bone get denser upon physical activity [Fredericson et al., 2007].

Cells not only adapt to passively applied forces in order to obtain appropriate resistance and maintain tissue integrity, but also actively probe the mechanical properties of their environment. Furthermore, mechanical forces are critical regulators of gene expression and tissue development. Substrate stiffness alone can influence the lineage specification of mesenchymal stem cells [Engler et al., 2006] and increased matrix stiffness in the tumor

environment promotes epithelial-mesenchymal transition (EMT) and metastasis [Wei and Yang, 2016]. Even though cause and consequence cannot always be determined as clearly as in the previous examples, a wide spectrum of (patho-)physiological processes and diseases are correlated with altered mechanical properties – amongst them asthma, atherosclerosis, hypertension, muscular dystrophy, pulmonary fibrosis and rheumatoid arthritis [Ingber, 2003]. Furthermore, also the process of aging is accompanied by significant changes in cell and tissue mechanics [Phillip et al., 2015]. Together, these examples demonstrate the long neglected omnipresence of mechanics in biology.

1.1.1 Mechanotransduction at the molecular level

Two types of mechanical processes can be distinguished at the cellular and molecular level: mechano-*transmission* and mechano-*transduction*. Even though both terms are sometimes used interchangeably, mechanotransmission describes the passive force coupling of two molecules, whereas mechanotransduction refers to the transformation of mechanical information into biochemical signals.

One of the most straight forward examples of mechanotransduction are mechanosensitive ion channels. While most readers will immediately think of the inner ear's hair cells [Ross and Pawlina, 2006], stretch-gated ion channels are far more ubiquitous and can be found in the membranes of bacteria, archaea, and eukarya [Pivetti et al., 2003].

Less direct mechanosensing pathways typically start with a small conformational change within a protein that is directly exposed to force. A subsequent signaling cascade then amplifies the small initial change and activates effector molecules. These signaling cascades apply the same principles as other commonly know intracellular signaling pathways, e.g. allosteric regulation, phosphorylation, or the involvement of GTP-binding proteins and GTPases.

Focal adhesions are one of the best studied examples of mechanotransduction. They apply a wide range of different molecular mechanisms (reviewed by Sun et al. [2016] and Ringer et al. [2017a]) and shall therefore serve as example to highlight how a single mechanical stimulus can be translated into diverse intracellular signals.

Integrins are important transmembrane receptors that mediate cellular adhesions to the extracellular matrix (ECM). Before integrins can establish the initial ECM contact, they are activated through talin and kindlin binding by an *allosteric signaling* mechanism [Hynes, 2002]. This process is followed by engagement of the complex with the F-actin cytoskeleton and initial force generation. If high enough, this initial tension unfolds helical bundles within the talin rod and leads to the exposure of *cryptic binding sites* for vinculin. Vinculin is a molecule that establishes additional linkages between talin and F-actin. Forces along

talin thus form a positive *feedback loop*. In addition, the tails of activated integrins serve as *docking hubs*, that bring numerous other proteins (including *kinases* and *small GTPases*) into close vicinity and thus enable their interaction [Ringer et al., 2017a, Sun et al., 2016]. Another typical example of molecular mechanotransduction that was observed for some integrin isoforms is the formation of so called *catch bonds*, which are protein-protein interactions that are stabilized under force and show a prolonged lifetime when under load [Sun et al., 2016, Thomas, 2008].

Catch bonds have also been observed in the context of chromosome transport during cell division and will be discussed in more detail in section 1.5.1.

Another common mechanism for mediating cellular effects based on mechanotransductive signaling is the translocation of transcriptional co-factors such as MRTFs, YAP, and TAZ, recently reviewed by Finch-Edmondson and Sudol [2016].

Even though several years of research shed some light on how cells process mechanical information, our knowledge of the molecular mechanisms that underlie mechanotransduction is still rather limited in relation to its wide abundance and relevance. This is to a large extend caused by the inherent difficulty to study mechanotransduction on a molecular level and in – ideally – living cells. Only since the beginning of the 21st century, suitable techniques (see sec. 1.3.1) have been developed or became accessible to a wider range of researchers, resulting in a steep increase of articles indexed under "mechanotransduction" on PubMed (from < 50 before the year 2000 to 758 in 2015).

1.2 Biological fundamentals: Cell division and the kinetochore

Replication is one of the most fundamental aspects of life and follows a regular pattern of events commonly referred to as cell cycle or cell-division cycle. The cell cycle of eukaryotes can be divided into two phases named interphase (which typically last for at least 90 % of the cell cycle) and mitosis (the phase of actual cell division). Both phases can be divided into several sub-phases (fig. 1.1) [Alberts et al., 2007, Lodish et al., 2007].

Interphase starts with a first "gap phase" called G_1, during which the cell resumes biosynthetic activities that were slowed down during the preceding division and increases the number of organelles and total size. The start of DNA replication marks the beginning of Synthesis (S) phase. With the exception of histone proteins, RNA transcription and protein synthesis rates are low during S phase, setting the requirement for a second growth phase G_2 before the actual process of cell division begins. Differentiated or resting cells that do not undergo active replication can enter a resting phase called G_0 instead of entering G_1.

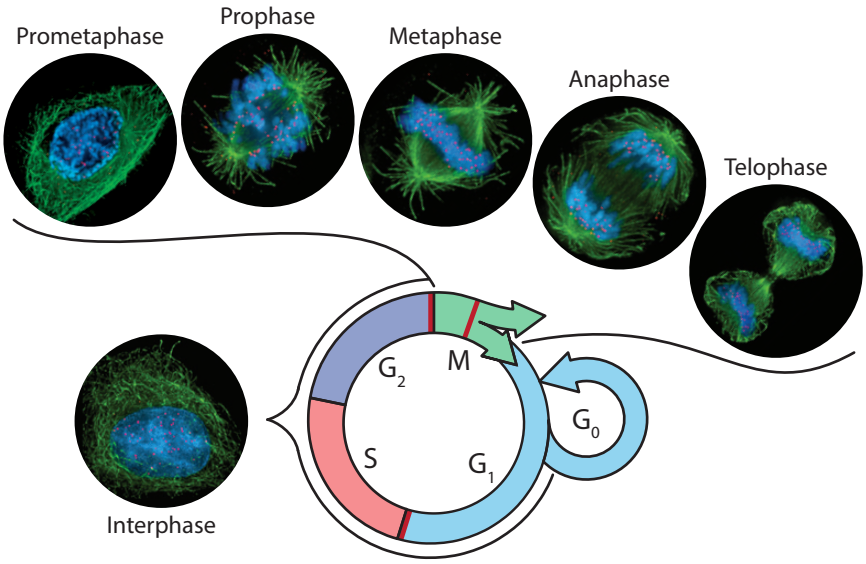

Figure 1.1: The cell cycle. A complete cell cycle covers four phases. The first three phases, namely gap phase 1 (G_1), synthesis phase (S) and gap phase 2 (G_2), are also summarized as interphase. The mitotic phase (M) is the shortest, but most active of all phases and can be subdivided into six individual steps itself (see also fig. 1.2). Quiescent and senescent cells enter a resting stage G_0. The three cell cycle checkpoints are indicated by red lines. Immunofluorescence images are reproduced with permission from Cheeseman et al. [2008] and show DNA (blue), microtubules (green) and kinetochores (red).

Despite lasting much shorter than interphase, mitosis requires a series of precisely timed and coordinated events that are described in more detail in section 1.2.1.

Within a full cell cycle, cells have to pass three checkpoints at which the internal state of the cell is monitored. Progression to the next step of division will only occur if all conditions are favorable.

The G_1 checkpoint (also known as start point in yeast and the restriction point in mammalian cells) ensures that all prerequisites for replication are met. While the checkpoint is active, cells monitor their size and energy status and check for DNA damage (which could cause mutations during genome replication). Once the G_1 checkpoint is passed, the cell irreversibly commits to the cell division process and enters S phase.

The function of the G_2 or DNA damage checkpoint is quite similar to that of the G_1 checkpoint: The cell again assesses its size as well as energy and protein reserves. However, the most important role of the G_2 checkpoint is to ensure that all chromosomes have been accurately replicated without mistakes or damage. If all conditions are favorable, cells proceed to mitosis, the actual phase of division.

A third checkpoint called spindle assembly checkpoint (SAC) has to be passed during mitosis, just before sister chromatid separation. Due to its importance for this thesis, it will be described in more detail after discussing the process of mitosis itself (see sec. 1.2.5).

1.2.1 Mitosis

Eukaryotic cells are highly complex machineries and the division of such a system into two functional units requires the coordinated completion of many diverse processes [McIntosh, 2016]. The following paragraphs will briefly summarize the main steps of cell division (also depicted in fig. 1.1 and 1.2).

The first phase of mitosis, called prophase, begins with the condensation of DNA into compact chromosomes. While the nuclear envelope (NE) is still intact, the by that time duplicated centrosomes move apart and start nucleating microtubules (MTs) to form a precursor of the mitotic spindle [Cheeseman et al., 2008]. As soon as chromosome condensation

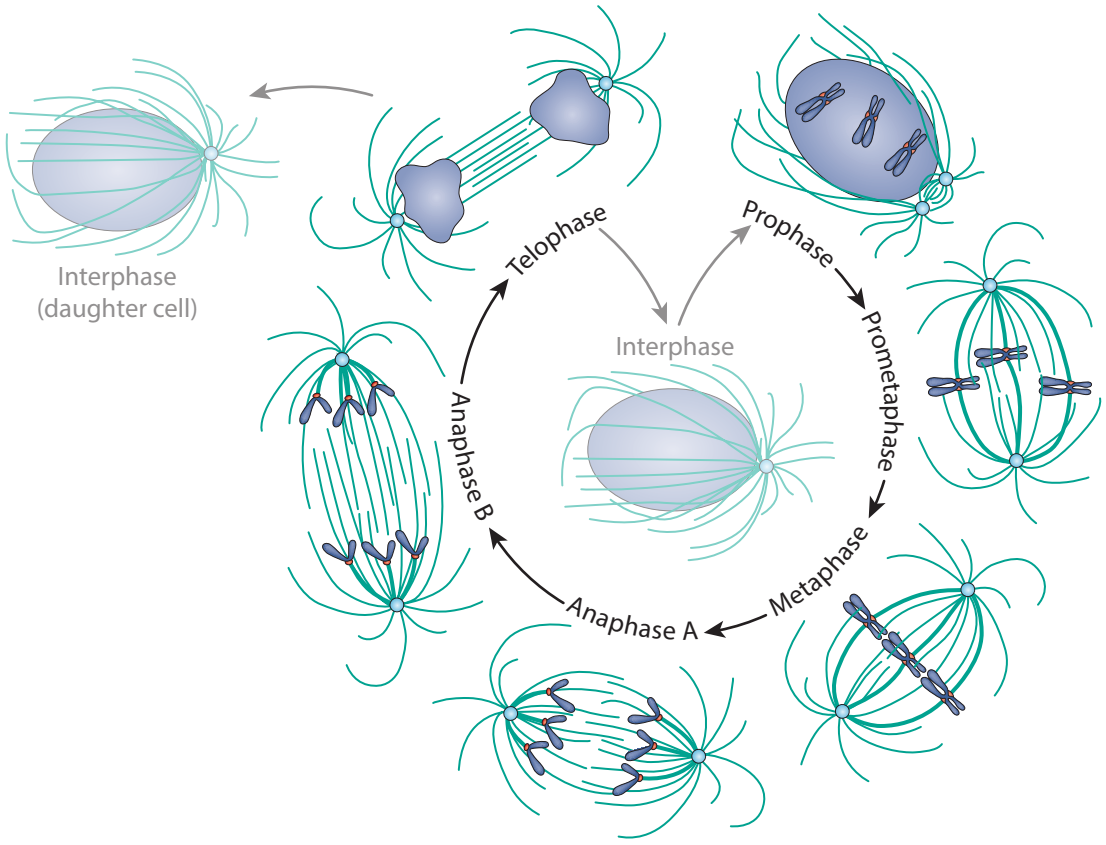

Figure 1.2: Mitotic phases. Mitosis is a series of processes that can be staged into individual phases. In interphase cells (not part of mitosis itself), the DNA is decompacted and a single centrosome organizes the MT cytoskeleton. During prophase, chromosomes become highly condensed and the duplicated centrosomes separate. Nuclear envelope breakdown marks the transition to prometaphase and the actual spindle is formed. The alignment of all chromosomes at the spindle equator marks metaphase. Cohesins are cleaved at the transition to anaphase and sister chromatids move apart by a combination of k-fiber shortening (anaphase A) and spindle elongation (anaphase B). The nuclear envelope is reformed around the decondensing chromosomes during telophase. Cytokinesis finally separates both daughter cells, which marks the beginning of a new interphase. Images are reproduced with permission and modified from Walczak et al. [2010].

is completed, abrupt breakdown of the NE marks the beginning of prometaphase. Spindle MTs can now attach to chromosomes at the meanwhile assembled kinetochore (KT) (see sec. 1.2.3) and chromosomes are subsequently transported to the equatorial plane, a process called chromosome congression [Maiato et al., 2017]. At metaphase, all chromosomes are aligned at the equator and bioriented, i.e. kinetochore microtubules (kMTs) attach the two sister KTs of one chromosome to opposite spindle poles. With the beginning of anaphase, sister chromatids are physically discoupled by the cleavage of cohesin. Chromatids are then separated through a combined action of shortening kMTs and elongation of the spindle itself (details in sec. 1.5) [Asbury, 2017, Scholey et al., 2016]. The very short anaphase smoothly transits to telophase, during which the chromosomes are pulled even closer to the spindle poles. In addition, the NE starts to reassemble around each set of chromosomes and division of the cytoplasm begins with the contraction of an actin ring that is assembled at the plasma membrane [McIntosh, 2016]. Cytokinesis marks the final step of mitosis by actually creating two daughter cells [Glotzer, 2016]. In parallel, chromosomes decondense within the newly formed nuclei and the mitotic spindle disassembles [McIntosh, 2016].

1.2.2 The mitotic spindle – Part I: Morphology

The mitotic spindle is a self-organizing micro-machine that ensures proper segregation of the sister chromatids into the two daughter cells [Pavin and Tolić, 2016]. Even though not all MTs of the spindle make contact with the centrosomes directly [Burbank et al., 2006,

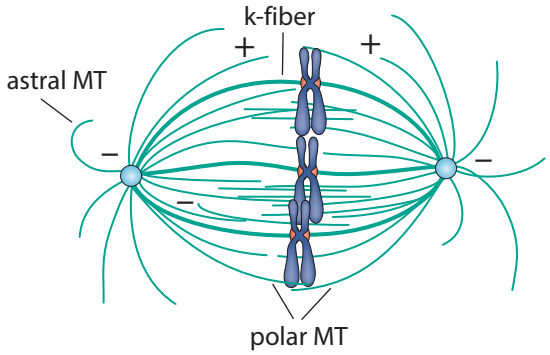

Figure 1.3: Spindle morphology. Three types of MTs are found in the mitotic spindle, all of them pointing with their minus-ends towards the spindle poles. Kinetochore MTs connect the KTs to the spindle poles. In most organisms, multiple kMTs bind a single KT, and bundles of kMTs are called k-fibers. Polar MTs run parallel to k-fibers but cross the spindle equator instead of attaching to chromosomes. Astral MTs anchor the spindle at the cell cortex and are usually embedded directly into centrosome. On the contrary, not all kMTs and polar MTs extend to the centrosomes but some are crosslinked with their minus-ends to other spindle MTs. The image is reproduced with permission and modified from Walczak et al. [2010].

Sikirzhytski et al., 2014], they arrange in the pattern of a double-aster with their minus-ends typically pointing towards the nearest centrosome [Pavin and Tolić, 2016].

Three different types of MTs coexist within the mitotic spindle (fig. 1.3): kinetochore MTs (kMTs) are MTs that actually bind KTs. While only a single MT binds per KT in *S. cerevisiae*, most other organisms form bundles of 15 – 25 parallel MTs, called k-fibers [Cheeseman, 2014, Forth and Kapoor, 2017]. Astral MTs, which typically originate at the centrosome and extend to the cell cortex, are involved in initial chromosome capture and play an important role in positioning of the spindle. The third type of MTs are so called polar or interpolar MTs. They run parallel to k-fibers, but instead of attaching to KTs, they form antiparallel overlaps with MTs emerging from the opposite pole [Forth and Kapoor, 2017, Pavin and Tolić, 2016].

A wide variety of cross-linking proteins belonging to either of the following three classes have been found in mitotic spindles: (1) plus-end directed motor proteins, (2) minus-end directed motor proteins, and (3) cross-linking proteins without motor activity [Pavin and Tolić, 2016]. Notably, many motor proteins are also able to manipulate MT dynamics, e.g. trough the stabilization of MT plus-ends or the promotion of MT catastrophe [Musacchio and Desai, 2017].

The broad abundance of motor proteins within the spindle may suggest a simple mitotic mechanism, in which chromosomes are attached laterally to MTs and transported by classical motor proteins, very much like vesicular transport. A closer look into the molecular structure of KTs and their interactions with MTs, however, will reveal a different and unique type of MT-mediated transport. Central feature of this transport are end-on attachments, in which KTs directly bind to the plus-end tips of MTs (see also sec. 1.5.1).

1.2.3 Kinetochore composition and function

1.2.3.1 The centromere

Kinetochores are macromolecular structures of more than 100 different proteins that assemble during mitosis and mediate binding of chromosomal DNA to spindle MTs [Cheeseman, 2014]. The KT itself does not assemble on chromosomal DNA directly, but instead recognizes a specific region known as centromere. While many features of the mitotic machinery are highly conserved across eukaryotes [van Hooff et al., 2017], the nature and size of centromeric DNA varies dramatically between organisms and can be broadly classified into three types: point centromeres, regional centromeres, and holocentromeres [McKinley and Cheeseman, 2016, Musacchio and Desai, 2017, Nagpal and Fukagawa, 2016].

Point centromeres are found in the budding yeast *Saccharomyces cerevisiae* and consist of a highly specific, 125 base pair (bp) long DNA sequence which is recognized by the CBF3

protein complex exclusively found in this species [Biggins, 2013]. Regional centromeres are the most abundant and also most heterogeneous centromere type, and their size varies from tens of kilobases (kb) in *Schizosaccharomyces pombe* to several megabases (Mb) in humans. Regional centromeres often contain repetitive DNA sequences, but these lack sequence conservation between species [Cheeseman, 2014, Nagpal and Fukagawa, 2016]. Some insects and plants as well as the nematode *Caenorhabditis elegans* have holocentric chromosomes, in which the entire length of the chromosome acts as centromere [McKinley and Cheeseman, 2016, Nagpal and Fukagawa, 2016].

Due to the lack of specific centromere sequence motives, it is believed that centromeres are defined epigenetically by specific histones, such as the H3 variant centromere protein A (CENP-A) [McKinley and Cheeseman, 2016, Valente et al., 2012].

1.2.3.2 Kinetochore ultrastructure in electron microscopy

Early electron microscopy (EM) images revealed a trilaminar KT morphology with two clearly distinguishable electron-dense layers (referred to as the inner and outer KT) separated by an electron-translucent middle layer [McEwen et al., 2007]. Sample preparation in these studies, however, followed conventional chemical fixation procedures and thin-section transmission electron microscopy (TEM). More recently, PtK1 (rat kangaroo) cells were analyzed by high-pressure freezing electron tomography. In these images, the translucent middle layer was absent and the outer plate appeared as a fibrous mesh in which MTs embedded (fig. 1.4) [Dong et al., 2007, McEwen et al., 2007]. Nevertheless, due to the historical

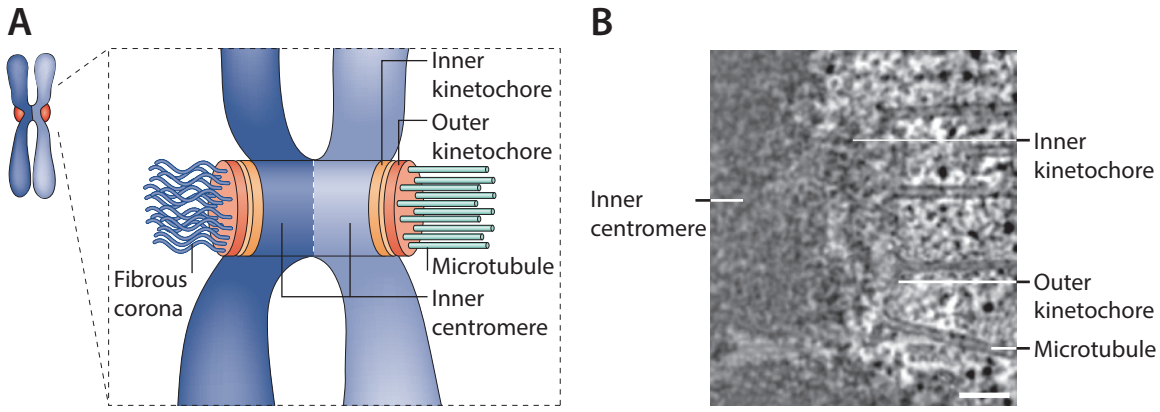

Figure 1.4: Ultrastructure of the vertebrate kinetochore. A) The KT is typically subdivided into an inner and outer plate. EM images of unattached KTs show a fibrous corona adjacent to the outer KT, which is build of MT binding proteins and molecular motors as well as proteins implicated in SAC signaling [Musacchio and Desai, 2017, Perpelescu and Fukagawa, 2011]. **B)** The historically observed trilaminar structure with clearly distinct inner and outer plates is absent in electron micrographs if obtained after sophisticated sample preparation. Scalebar 100 nm. Images are reproduced with permission from Cheeseman et al. [2008].

influence of the early EM studies, KTs are often still divided into an inner kinetochore that binds chromatin, and an outer layer, which mediates binding to MTs [Cheeseman, 2014, Nagpal and Fukagawa, 2016].

1.2.3.3 Molecular composition of the inner kinetochore

The inner KT is closely intertwined with centromeric chromatin. The so called constitutive centromere assiciated network (CCAN) is built by a group of 16 "CENtromere Proteins" (CENPs), which localize to centromeres throughout the entire cell cycle. These proteins are widely conserved from yeast to human; however, few but notable exceptions including *Drosophila melanogaster* and *Caenorhabditis elegans* have been identified that lack most CCAN components [Musacchio and Desai, 2017, van Hooff et al., 2017]. Based on *in vitro* reconstitution experiments and *in vivo* co-depletion, the 16 CCAN members are typically sub-categorized into the following complexes: (1) CENP-C, (2) the CENP-T complex made of CENP-T-W-S-X, (3) the CENP-H complex (CENP-H-I-K-M), (4) the CENP-L complex (CENP-L-N; note that CENP-M is sometimes also seen as part of this group), and (5) the CENP-O complex (CENP-O-P-Q-R-U(50)) (fig. 1.5) [Musacchio and Desai, 2017, Nagpal and Fukagawa, 2016, Perpelescu and Fukagawa, 2011, Pesenti et al., 2016].

The best studied CCAN components are CENP-C and the CENP-T group, which are both directly involved in connecting to the outer KT and thus finally to MTs. All four subunits of the CENP-T complex possess histone fold domains and the complex directly binds DNA *in vitro*. CENP-C and CENP-N have been found to interact with the centromere

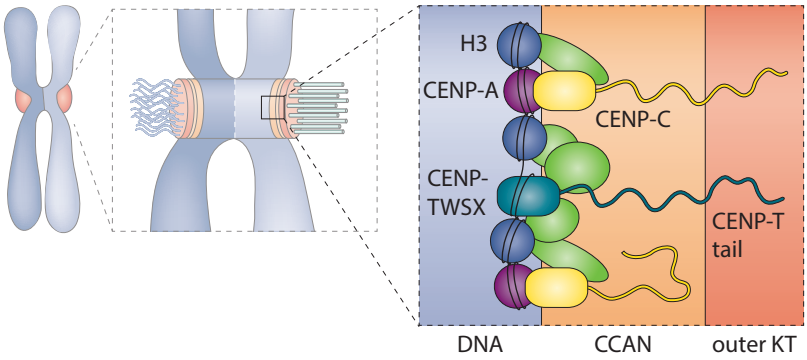

Figure 1.5: Molecular composition of the inner kinetochore. The centromeric region is epigenetically defined by the histone variant CENP-A. The tetrameric CENP-TWSX complex directly binds to centromeric DNA via histone-fold domains, and the elongated tail of CENP-T reaches towards the outer KT. CENP-C localizes trough interactions with CENP-A. If not bound to outer KT proteins, the CENP-C tail shows a bent conformation [Suzuki et al., 2014]. The precise localization of CENP-H–, CENP-L– and CENP-O–complexes (all indicated in green) is not yet known, but they are important for stabilizing the localization of CENP-C and CENP-T to the centromere [Musacchio and Desai, 2017]. Left part of the image is reproduced with permission from Cheeseman et al. [2008].

defining histone variant CENP-A. *In vitro*, these interactions are rather weak and show low selectivity for CENP-A over H3; however, their localization is presumably stabilized by the CENP-L and CENP-H complexes *in vivo* [Musacchio and Desai, 2017].

While the loss of most CCAN members severely affects the formation of KT–MT contacts, the consequence of CENP-O complex knock down on initial attachment is rather mild. Its precise function is not yet well understood, but the complex has been shown to play a role in chromosome congression, recovery from spindle damage, and the recruitment of a number of additional KT components [Musacchio and Desai, 2017, Nagpal and Fukagawa, 2016, Perpelescu and Fukagawa, 2011].

A number of studies analyzed the hierarchy of protein recruitment within the CCAN, however with partially divergent results for different species. Yet, the underlying consensus of these studies is that the members of the CCAN (with the exception of the CENP-O complex) tightly work together in forming the "bottom layer" of the KT [Takeuchi and Fukagawa, 2012].

1.2.3.4 Molecular composition of the outer kinetochore

Most of the >100 identified KT proteins localize to the outer plate, which (in contrast to the CCAN) assembles only during mitosis. Proteins of the outer KT are less conserved than the CENP family; yet, conservation is still remarkably high compared to other classes of proteins and homologs of many vertebrate proteins have been found in other organisms [Meraldi et al., 2006, Perpelescu and Fukagawa, 2011, van Hooff et al., 2017, Westermann and Schleiffer, 2013].

Outer KT proteins can be roughly separated into three categories: (1) proteins that establish the mechanical linkage between DNA and MTs, (2) proteins with a regulatory function like kinases and phosphatases, and (3) proteins that are part of the SAC signaling machinery [Nagpal and Fukagawa, 2016]. Individual sections are attributed to these functions and relevant outer KT proteins will be introduced in the respective paragraphs.

1.2.4 Molecular structure of kinetochore–microtubule attachments

1.2.4.1 The Ndc80 complex is the major MT binding protein

The highly conserved Ndc80 complex is the primary MT receptor at the KT and its name is derived from the Ndc80 subunit, which is also known as Hec1 in vertebrates [Cheeseman et al., 2004, Musacchio and Desai, 2017, Perpelescu and Fukagawa, 2011]. The dumbbell-shaped Ndc80 complex assembles through the formation of extensive coiled-coils between the four subunits Hec1, Nuf2, Spc24, and Spc25 (fig. 1.6). MT-binding is mediated by the

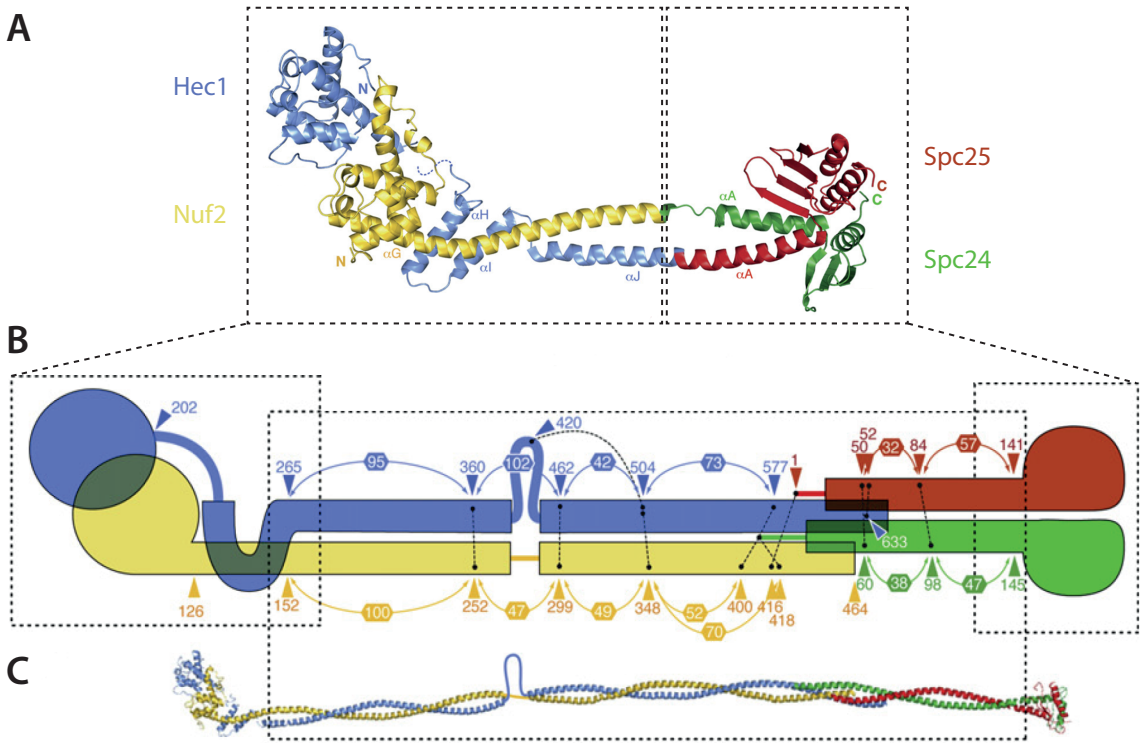

Figure 1.6: Structure of the Ndc80 complex. A) Crystal structure of $Ndc80^{bonsai}$, a shortened human Ndc80 construct that lacks most of the coiled-coil region. Note that the 80 most N-terminal amino acids of Hec1 form a disordered tail and have been removed for crystallization. **B)** Summary of crosslinking mass spectrometry (MS) analysis. Connected black dots mark crosslinked residues; numbers with arrows amino acids positions; numbers in hexagons define distances between pairs of interacting residues. **C)** Model of the full length Ndc80 complex, based on the $Ndc80^{bonsai}$ structure, combined with information obtained by crosslinking MS and structural prediction. images are reproduced with permission and modified from Ciferri et al. [2008].

globular N-termini of the Hec1/Nuf2 dimer, and kinetochore targeting is mediated by the C-terminal globular domains of the two Spc subunits [Ciferri et al., 2008].

The head domains of Hec1 and Nuf2 contain calponin homology (CH) domains, which are known MT-interacting motives. In addition, the very N-terminal part of Hec1 remains unstructured and forms a basic, positively charged tail (not shown in figure 1.6), that is subjected to a differential pattern of phosphorylation throughout mitosis [DeLuca et al., 2011, Zaytsev et al., 2015]. siRNA knockdown combined with co-expression of mutant variants in HeLa cells revealed that a charge reversal point mutation within the CH domain of Hec1 caused the most severe defects, followed by phospho-mimicking mutations in the Hec1 tail. Mutating the CH domain of Nuf2, on the contrary, had comparatively mild effects. Cells expressing this mutant were still able to form stable KT–MT attachments; however, they failed to generate wild type (wt) levels of inter-KT stretch and delayed anaphase onset [Sundin et al., 2011]. These experiments suggest that Hec1 plays the major role in KT–MT

attachments; a theory that is supported by EM images which suggest that only the Hec1 but not the Nuf2 head directly interacts with MTs [Alushin et al., 2010, Wilson-Kubalek et al., 2008].

In vitro studies demonstrated that the Ndc80 complex alone is sufficient to create load-bearing attachments to MTs [Powers et al., 2009] (details in sec. 1.5.2). *In vivo*, however, MTs are very dynamic and constantly switch between polymerization and depolymerization. This so called dynamic instability occurs mainly at the KT-binding plus-end, raising the question of how KTs are able to efficiently stay connected to the tip of a dynamic MT. Part of the answer is given by the presence of Dam1 in yeast and the ternary Ska complex in vertebrates, which both have been shown to stabilize KT attachments to dynamic MTs by the formation of MT encompassing rings (Dam1) or oligomerization (Ska complex) [Abad et al., 2016, Auckland et al., 2017, Jeyaprakash et al., 2012, Lampert et al., 2010]. For a more detailed description of force-generating and -coupling mechanisms between MT and KT see sections 1.5.1 and 1.5.2.

MT-binding activity was also observed for other KT components. Most of them (e.g. CENP-H, -I, and -Q [Amaro et al., 2010] or the outer KT protein Knl1 (see following section) [Cheeseman et al., 2006]) are believed to have regulatory functions on MT dynamics and SAC signaling rather than directly contributing to force transduction at the KT [Amaro et al., 2010, Espeut et al., 2012]. In addition, molecular motors were found at the kinetochore and their roles are discussed in section 1.5.

1.2.4.2 CENP-C and CENP-T form two distinct routes that connect the CCAN to microtubules

Two parallel pathways for Ndc80 complex recruitment to the CCAN have been identified in vertebrates and many other eukaryotes (fig. 1.7). The one discovered first is established by CENP-C and the so called KMN network, which is an assembly of the Ndc80 complex and the Mis12 and Knl1 complexes [Nishino et al., 2013]. The Mis12 complex is composed of the four proteins Mis12, Dsn1, Nsl1, and Pmf1 and its main function is the formation of a bridge between the Ndc80 complex and CENP-C [Petrovic et al., 2016]. The Knl1 complex, comprising Knl1 and Zwint, establishes an interaction hub for a number of proteins that are, for example, important regulators of the SAC [Musacchio and Desai, 2017].

Despite being discovered many years after the CENP-C–KMN linkage, the second link between the Ndc80 complex and the CCAN is of a much simpler nature, as it is established by direct binding of the Ndc80 complex to the CCAN protein CENP-T [Nishino et al., 2013, Schleiffer et al., 2012]. Even though this linkage can be established in the absence

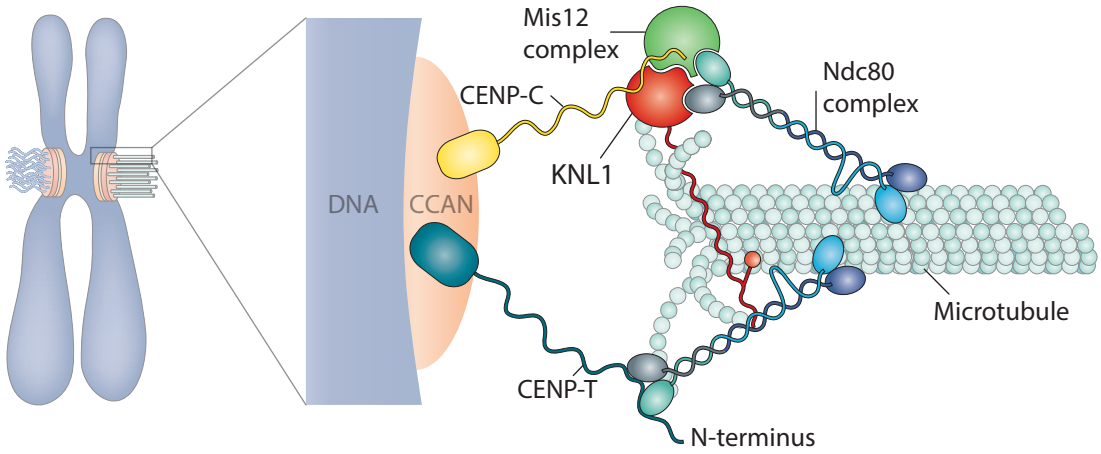

Figure 1.7: Molecular structure of kinetochore–microtubule attachments. The Ndc80 complex is the major MT binding element of the KT. It is linked to the constitutive centromere associated network (CCAN) either directly through CENP-T, or via CENP-C and the KMN network. The KMN network itself comprises the Mis12 complex, the Knl1 complex and the Ndc80 complex. Note that the orientation of the Hec1 loop within the Ndc80 complex towards the MT is speculative.

of Mis12 complex, recent studies showed that human CENP-T recruits a complete KMN network (including an additional copy of the Ndc80 complex) to a binding site distinct from the site for direct Ndc80 binding [Huis in 't Veld et al., 2016, Rago et al., 2015, Suzuki et al., 2015a]. Interestingly, KMN recruitment to CENP-C is promoted by Aurora B kinase activity, while KMN recruitment to CENP-T requires phosphorylation by cyclin B–dependent protein kinase 1 (CDK 1) [Rago et al., 2015], suggesting that both pathways can be regulated independently of each other and may fulfill different functions in human cells.

While first analyses pointed towards phosphorylation of CENP-T threonine-195 as regulator of KMN recruitment to the human CENP-T tail [Rago et al., 2015], Huis in 't Veld et al. [2016] showed that phosphorylation of serine-201 is necessary and sufficient for KMN binding. This serine is part of a recently defined minimal CDK1 consensus sequence S/T–X–X–R/K, but it was also shown that phosphorylation at this minimal motive is rather weak and depends on other residues surrounding the Ser/Thr-phosphoacceptor [Suzuki et al., 2015b]. In accordance with these findings, threonine-195 in human CENP-T could act as such an enhancing residue.

Notably though, clustering of the KMN network and CENP-T could not be seen in a whole-proteome genetic analysis of chicken DT40 cells [Samejima et al., 2015], raising the question whether CDK1 phosphorylation of the CENP-T tail and/or binding of the KMN complex is a conserved feature.

1.2.4.3 Kinetochore size and protein copy numbers

The aim of this thesis is the analysis of molecular KT forces with a fluorescent tension sensor. It is therefore interesting to look at the size of KTs and the number of protein copies localizing to each KT.

EM images revealed a diameter of ∼250 nm per vertebrate KT [Dong et al., 2007]. This value is just below the practical resolution limit of a confocal laser scanning microscope (CLSM) [Wilson, 2016], and KTs are therefore projected as nearly diffraction-limited spots in fluorescence microscopy.

Two studies by Johnston et al. [2010] and Suzuki et al. [2015a] embarked on the quantification of protein copy numbers at vertebrate KTs by measuring the fluorescence intensities of GFP-fused KT proteins and comparing those to the intensity of a single GFP molecule. Relevant results of both studies are summarized in table 1.1. Strikingly, the numbers differ quite significantly between the two studies with respect to absolute numbers as well as in their relative ratios. Such differences, however, are not surprising, considering that the reported numbers result from measurements and calculations with multiple free parameters. Most importantly, two different cell types have been used, namely DT40 cells by Johnston et al. [2010] and HeLa cells by Suzuki et al. [2015a]. Previously performed EM analysis of these cell lines already revealed a striking difference in the number of MTs per KT, which was reported to be 4.3 ± 1.1 in DT40 cells [Ribeiro et al., 2009] vs. 17.1 ± 0.6 in HeLa cells [Wendell et al., 1993]. Other sources of variation are experimental errors due to correction for background fluorescence and photobleaching, expected inaccuracies in the determination of the intensity of a single GFP molecule, and expression of the GFP-fusion proteins from a non-endogenous locus. (Expression levels of wt and tagged proteins were analyzed by Western blot and if both levels differed, fluorescent intensities were corrected accordingly. Western blots, however, analyze the mean expression level of an entire cell line, and individual cells may have divergent levels.) Interestingly though, protein copy numbers per kMT in DT40 cells fit very well to the number of 8 Ndc80 complexes that has been determined for the budding yeast point centromere, which binds only a single kMT [Joglekar et al., 2006].

Besides all the differences, two important conclusions can be drawn from these studies: First, the number of protein copies per KT is comparatively low in both systems, and second, the data of these studies support the hypothesis that human, but not chicken CENP-T is able to recruit a complete KMN network (additional data supporting KMN recruitment by human CENP-T are published in Suzuki et al. [2015a], but not listed in table 1.1).

Table 1.1: Protein copy number at kinetochores

	Johnston et al. [2010]		Suzuki et al. [2015a]	
	# per KT	# per MT	# per KT	# per MT
Hec1	33 ± 6[a]	7.7 ± 1.4	244.0 ± 31.8	14.3 ± 1.9
Mis12	39 ± 9	9.0 ± 2.1	151.1 ± 20.6[b]	8.8 ± 1.2
CENP-C	39 ± 10	9.2 ± 2.4	215.4 ± 33.2[c]	12.6 ± 1.9
CENP-T	28 ± 4	6.5 ± 0.9	71.6 ± 8.4[d]	4.2 ± 0.5

[a] The study did not analyze through which pathway Hec1 was recruited.
[b] The number reported by the authors is an average number obtained by individual measurements of three different members of the Mis12 complex (Mis12, Dsn1 and $Pmf1^{Nnf1}$).
[c] Additional measurement performed after knockdown of individual KT components revealed that only ∼40 % of all CENP-C molecules recruit a KMN network, explaining the high number of CENP-Cs in relation to Hec1 and Mis12.
[d] Additional measurements demonstrated that each CENP-T recruits ∼2 Ndc80 complexes.

1.2.4.4 Spacial organization of the kinetochore–microtubule binding interface

The budding yeast KT assembles onto a single Cse4-containing nucleosome and binds only one kMT [Cieśliński and Ries, 2014]. Nevertheless, its organization is remarkable similar to KTs that assemble on regional centromeres of higher eukaryotes [Musacchio and Desai, 2017]. It is therefore a plausible hypothesis, that regional KTs are an assembly of multiple units that each resemble the budding yeast KT. In such a model, an individual kMT would bind to a predefined set of clustered adapters. However, no such structurally repeated units could be seen in EM [Dong et al., 2007, McIntosh et al., 2013]. Zaytsev et al. [2014] therefore proposed that KTs on regional centromeres resembles a "lawn" with unrestricted molecular interaction between individual Ndc80 complexes and kMTs. To test their model, they embarked on an elaborate comparison of *in vivo* data and *in silico* simulations. Based on multiple parameters like the size of k-fibers, kinetics of MT acquisition, distribution of the number of MTs per k-fiber, mean half-life per kMT, different degrees of Hec1 tail phosphorylation, and the consequence of Ndc80 complex depletion (amongst others), they found that a lawn model, but not a model assuming predefined clustered repeats was successful in describing the experimental data.

1.2.5 Spindle assembly checkpoint

Initial KT–MT attachments are established by a stochastic search-and-capture process. Consequently, amphitelic attachments as seen in correctly bi-orientated chromosomes are rarely established at first contact [Lampson and Grishchuk, 2017]. Instead, three types of erroneous KT–MT attachments are frequently observed (fig. 1.8) [Walczak et al., 2010].

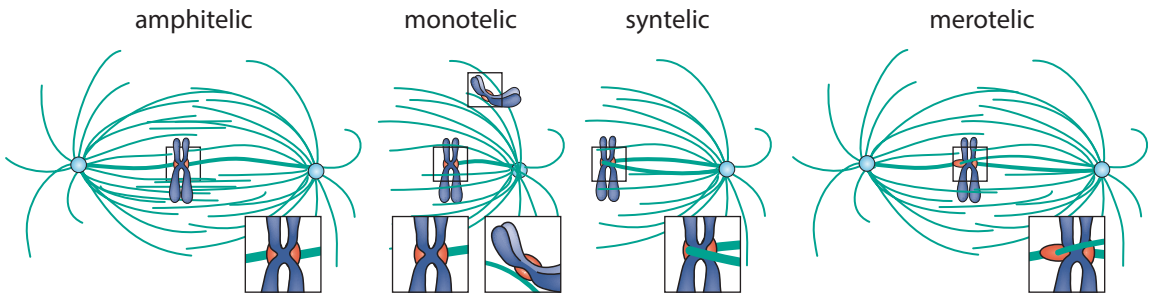

Figure 1.8: Correct and erroneous kinetochore–microtubule attachments. Chromosomes that formed end-on attachments and obtained bi-orientation are called amphitelic. However, initial contacts between MTs and KTs are formed at random and biorientation is rarely established directly. Monotelic chromosomes are attached with only one KT, either laterally or end-on oriented. Syntelic chromosomes established two end-on attachments, but both k-fibers connect to a single centrosome. In merotelic attachments, a single KT is attached to MTs extending from both sites of the spindle. Images are reproduced with permission and modified from [Walczak et al., 2010].

Monotelic chromosomes are connected to the spindle at only one KT, either laterally or by an end-on attachment. Syntelic chromosomes established two end-on attachments, but to k-fibers from the same spindle pole. In a merotelic attachments, one KT is correctly attached to a single spindle pole, but the sister KT makes contact to MTs extending from both poles. As cell division in the presence of improperly attached chromosomes drives aneuploidy and thus severely effects the health of both daughter cells, it is important to correct these attachments before sisterchromatid separation.

The SAC transduces mechanical cues from KTs into a mechanochemical signaling cascade, thus inhibiting cell division until all chromosomes are properly attached. Extensive investigations of the molecular mechanisms underlying SAC signaling have yielded a comprehensive understanding of the events that cause cell cycle arrest once the SAC is activated (recently reviewed by London and Biggins [2014], Musacchio [2015] and Joglekar [2016]). Central matter of a longstanding debate, however, is the molecular identity of the signal that triggers SAC activation in first place, or (if seen from the other direction) what has to be achieved to satisfy the SAC. The two mechanisms under debate are either direct monitoring of tension at the KT, or the attachment status alone (irrespective of the amount of tension generated) [Joglekar, 2016].

1.2.5.1 Indications for tension-dependent SAC satisfaction

Pioneering experiments by Nicklas [1969] revealed that syntelic attachments during meiosis I in grasshopper spermatocytes are unstable, unless tension is artificially applied via a microneedle. Inspired by these (and subsequent) experiments, McIntosh [1991] postulated that the centromeric region of unattached chromosomes generates a "wait-anaphase" signal, which is directly dependent on the mechanic state of centromeric chromatin. Di-

rect verification of Nicklas' observation in other cell types and during mitosis, however, remained difficult, as they are not amenable to manipulation with microneedles [Lampson and Grishchuk, 2017]. Only 46 years later, Drpic et al. [2015] reported an elegant genetic variant of this experiment by the generation of *Drosophila* S2 cells undergoing mitosis with unreplicated genomes (SMUGs). Due to the absence of sister KTs, these cells never experienced bi-orientation but yet were able to satisfy the SAC, however with pronounced delay. Interestingly, this delay was significantly reduced after KT tension was increased through the elevation of polar ejection forces. This was obtained by overexpression of plus-end directed kinesin motors called chromokinesins, that act on chromosome arms and push them away from the poles.

Aurora B, a kinase that localizes to the midzone of centromeres, was postulated as the key regulator of tension-dependent SAC silencing. A gradient of decreasing Aurora B activity towards the periphery of KTs had been detected. Furthermore, an increased distance between sister KTs was observed in metaphase when chromosomes are presumably under tension [Maresca and Salmon, 2009]. Combination of these observations lead to the hypothesis that tension across the centromere silences the SAC by spatially separating Aurora B from its targets, which localize to the outer KT [Foley and Kapoor, 2013].

1.2.5.2 Indications for attachment dependent SAC satisfaction

Despite the striking observations discussed in the previous paragraph, increasing evidence against the tension theory accumulated over the years [Khodjakov and Pines, 2010]. Laser ablation of the last unattached KT, for example, stopped SAC activation [Rieder et al., 1995]. Furthermore, cells with monopolar spindles (obtained by inhibition of centrosome separation with an Eg5 inhibitor) and thus exclusively merotelic and syntelic attachments satisfied the SAC if MT-binding to Hec1 was stabilized by expression of a phosphoresistant Hec1 mutant [Etemad et al., 2015, Tauchman et al., 2015]. Mitotic arrest upon treatment with the MT stabilizing drug taxol has been commonly used as argument against the attachment-only theory. A recent study, however, revealed that besides overall stabilization of the spindle, unattached KTs can still be found in taxol treated cells [Magidson et al., 2016].

The molecular mechanism proposed for an attachment-only theory is based on the competitive binding of MTs and the SAC activator Mps1 to the CH domain within the Hec1 head [Joglekar, 2016]. It was shown that, at least in budding yeast, the kinetochore encodes a mechanical switch to disrupt SAC signaling upon MT binding via a molecular replacement mechanism [Aravamudhan et al., 2015]. In addition, dynein-mediated stripping of checkpoint proteins away from the kinetochore plays an important role in SAC silencing after MT attachment [London and Biggins, 2014].

It should be noted that advocates of the attachment-only theory do not deny the existence of an error correction pathway. But they assume that a machinery independent of the SAC itself promotes error correction by the disassembly of incorrect attachments, which leads to SAC only as a secondary effect due to the generation of unattached KTs [Khodjakov and Pines, 2010, Lampson and Grishchuk, 2017, Maresca and Salmon, 2010].

1.2.5.3 Tension and attachment closely intertwine

How is it possible that – despite many years of combined effort of even more researchers – the primary source of SAC activation is still contentious? The experimental discrimination of tension and attachment is hampered by two main difficulties: First, methods that allowed direct tension measurements have been missing for many years (see also sec. 1.2.6, 1.5.2, and 1.5.3). And second, it became evident that tension and attachment closely intertwine and, therefore, are extremely difficult to investigate independently of each other. Obviously, tension cannot be established without attachment, but strikingly, tension itself increases not only the strength and duration of KT–MT attachments, but also the stability of MTs themselves [Akiyoshi et al., 2010, Franck et al., 2007, Miller et al., 2016]. Interestingly, this increased affinity and attachment stability was directly caused by physical tension and independent of Aurora B kinase activity [Akiyoshi et al., 2010].

1.2.6 Kinetochore stretch as surrogate marker of tension

Direct force measurements at distinct molecules within living cells have been out of reach for many years due to the lack of suitable techniques [Freikamp et al., 2017], and researchers had to rely on indirect markers of tension. The first such marker was an increased distance between sister KTs (also called inter-KT stretch), that was observed in bi-oriented chromosomes [Maresca and Salmon, 2010]. However, Rieder's laser ablation experiments [Rieder et al., 1995] together with subsequent work by others demonstrated that the SAC can be satisfied even in the absence of inter-KT stretch [Khodjakov and Pines, 2010]. Yet, this did not extinguish, but rather shift the tension versus attachment debate to a new kind of tension that had meanwhile been identified, namely intra-KT stretch [Maresca and Salmon, 2010]. Technical advancements in fluorescence microscopy facilitated distance measurements between distinct proteins or protein domains within one KT, and thus allowed the construction of a molecular map of yeast and HeLa KTs [Joglekar et al., 2009, Wan et al., 2009]. Maps generated at different stages of the cell cycle revealed that yeast KTs show larger intra-KT stretch in metaphase as compared to anaphase [Joglekar et al., 2009], and that the compliant linkages of HeLa cells localized to the inner rather than the outer KT [Wan et al., 2009]. In the same year, Maresca and Salmon [2009] and Uchida et al.

[2009] published that the SAC is satisfied under low concentrations of taxol, which abolish inter-KT stretch while preserving intra-KT stretch.

The molecular nature of this intra-KT stretch was further analyzed by a combination of immuno-EM and dual color fluorescent tagging of DT40 kinetochore components [Suzuki et al., 2011]. These experiments revealed that the inner KT region, represented by CENP-A, -C, -R, and -T is deformed in the presence of tension, while the outer KT (Hec1/Ndc80, Mis12 and CENP-E) showed no deformation. Furthermore, the compliant region of CENP-T could be mapped to its C-terminal domain.

The simple theory of the KT being stretched by pulling forces is appealing, but a more sophisticated analysis in life cells correlated intra-KT stretch with the direction of chromosome oscillation, and revealed that the leading (poleward moving) KT is rather compressed than stretched, while the trailing KT shows larger intra-KT stretch [Dumont et al., 2012]. The authors explained this counterintuitive observation with the coexistence of a proximally located active force-generating interface and a separated, more distally located passive MT-binding interface. Alternatively, these observation can be also explained by growing MT tips that push against the inner layer of the KT [Khodjakov and Pines, 2010].

Intra-KT stretch has received broad attention as a marker of KT tension, but two important shortcomings of this concept have to be noted: First, intra-KT stretch is usually measured between domains that are, from a mechanical perspective, not directly linked (though exceptions like the two termini of CENP-T exist). It is thus possible that spacial rearrangement rather than actual force causes intra-KT stretch [Joglekar, 2016]. And second, intra-KT stretch has been traditionally measured in 2D. A recent study that analyzed KT stretch in 3D still found evidence of intra-KT stretch, but to a significantly lower extend than inferred from 2D imaging techniques [Smith et al., 2016]. Instead, the authors observed a rotational rearrangement upon MT binding that projects as reduced distance when viewed in 2D.

All attributes used in the past to infer KT tension sooner or later proved to be inapplicable, but the interest in KT forces, and with it the demand for a technique to measure these forces, is persistently high. The development of molecular tension sensors that can be applied in life cells will hopefully help to shed light on one of the most fundamental and long-standing mysteries of biology.

1.3 Biophysical fundamentals: Molecular force measurements and FRET-based tension sensors

Classical methods in biology and biochemistry, such as genetic screens, helped to identify a wide range of proteins involved in mechanobiological processes. Precise localization and quantification of the relevant forces, however, was a difficult task in the early years of mechanobiological research. The development of single-molecule force spectroscopy opened ample opportunities to study protein mechanics *in vitro*, but the development of techniques that were applicable in living cells or even in whole organisms lagged many years behind [Freikamp et al., 2017]. In the following sections, I will shortly describe the most abundant methods for molecular tension measurements with a particular focus on genetically encoded tension sensors for life-cell applications.

1.3.1 Methods for measuring molecular tension

One way of grouping methods that are used in the field of mechanobiology is to distinguish between those that actively apply forces onto the molecule of interest while monitoring its response (fig. 1.9), and those that measure forces generated or experienced by the molecule by the probe itself (fig. 1.10). Optical and magnetic tweezers together with atomic force microscopy (AFM) are the most widespread examples of the first group. Sensors of the latter group can be further sub-classified into extracellular and intracellular sensors; in both cases, the readout is typically a change in fluorescence intensity or Förster resonance energy transfer (FRET). As changes in FRET can be more reliably detected and quantified than changes in fluorescence intensity or emission spectrum, FRET-based tension sensors (TSs) form the most widespread class of tension sensor modules (TSMs) and will be described in more detail in section 1.3.3.

1.3.2 Förster resonance energy transfer

Förster resonance energy transfer (FRET) (comprehensively reviewed by Lakowicz [2006]) describes a photophysical process, during which the energy of an excited donor chromophore is transferred to an acceptor chromophore, which finally releases the energy by light emission. FRET is sometimes spelled out as *fluorescence* resonance energy transfer, which is misleading because the energy transfer between the fluorophores itself is a nonradiative process (i.e. without the emission of light). Instead, energy is transferred via long range dipole–dipole interactions, which require an overlap of the donor emission and the acceptor absorption spectrum. In addition, the rate of energy transfer depends on the quantum yield (i.e. brightness) of the donor, the relative orientation of the donor and acceptor chro-

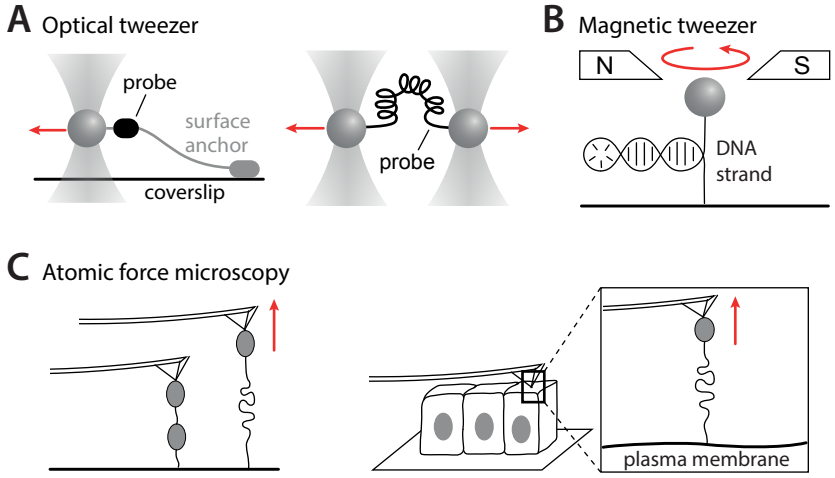

Figure 1.9: Methods probing effects of externally applied forces. A) Optical tweezers have been used to study binding strength of two interacting proteins, e.g. between the Ndc80 kinetochore complex and microtubules. Dual optical tweezers allow the application of sub-piconewton forces and have been also used to study the mechanics of isolated proteins. **B)** Magnetic tweezers have been applied to study the stiffness and unwinding behavior of DNA strands. **C)** Atomic force microscopy can be used to stretch individual proteins on immobilized surfaces or cell surface receptors on cells. (Images are modified reproductions from Freikamp et al. [2017]).

mophores, and the distance between the two molecules. As the relative orientation of the two fluorophores is not known in most applications, it is commonly assumed that both fluorophores can freely rotate [Lakowicz, 2006].

In all practical cases, only a fraction of the total energy that has been absorbed by the donor will be transferred to the acceptor, while the remaining energy will be released as donor fluorescence. The term FRET efficiency E refers to the fraction of energy absorbed by the donor and then transferred to the acceptor. Given a particular pair of fluorophores (and under the assumption that these can freely rotate), E solely depends on the distance between the two fluorophores, and the distance at which $E = 0.5$ is known as *Förster distance* or R_0.

The relation between the energy transfer rate E and the distance between the fluorophores r is described by

$$E = \frac{R_0^6}{R_0^6 + r^6}. \tag{1.1}$$

As consequence of this distance dependency to the 6^{th} power and the properties of currently available fluorophores, FRET virtually only occurs at distances $< 10\,\text{nm}$, which is approximately $30\times$ less than the resolution limit of a fluorescence microscope. This feature makes FRET a unique tool for life cell microscopy, as it allows the analysis of molecular interactions at distances that are impossible to resolve by normal imaging or even by most superresolution microscopy techniques.

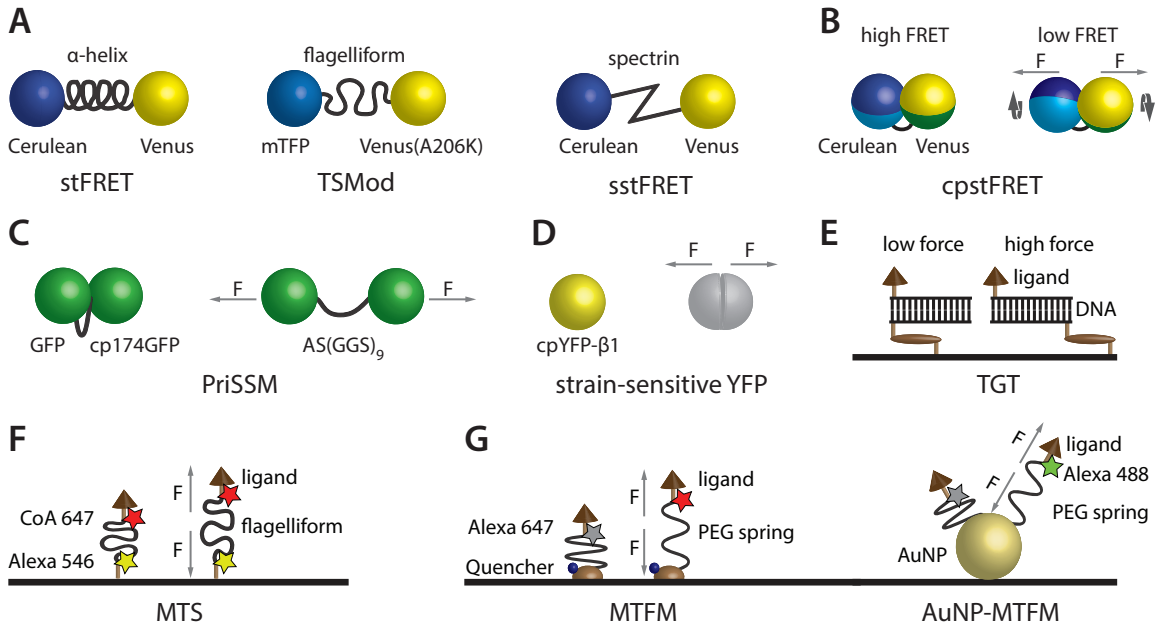

Figure 1.10: Methods measuring forces generated by cells. A) Most intracellular tension sensor modules comprise a FRET pair connected by an flexible linker that extends under force. **B)** An exception is the cpstFRET module, which shows a change in FRET upon fluorophore rotation. **C)** The PriSSM module reports forces by a distance-dependent change in the GFP emission spectrum. **D)** Strain-sensitive YFP looses its fluorescence when under force. **E)** The tension gauge tether (TGT) differs from other modules in the sense that the ligand is irreversibly detached from the surface if applied forces are high enough to unzip the DNA oligomer, thus preventing cellular adhesion. Rupture forces can be tuned by changing the relative position of the surface- and ligand-attachment sites. **F)** The MTS module is a version of the TSMod that applies organic dies instead of fluorescent proteins and can be used to measure forces that cells exert on the matrix. **G)** MTFM modules are similar to MTS, but apply a fluorophore and quencher instead of a FRET pair. For more detailed information, see Cost et al. [2015]. Images are reproduced with permission and modified from Cost et al. [2015].

1.3.3 FRET-based tension sensors

The development of genetically encoded FRET-based TSMs allowed, for the first time, direct force measurements across distinct molecules within living cells. While initially different types of modules have been developed (fig. 1.10, [Cost et al., 2015]), FRET-based modules that functionally resemble a molecular spring scale became prevalent [Freikamp et al., 2016]. The core of these TSMs is a mechanosensitive linker peptide that responds to mechanical load by a well defined length increase, resulting in decreased FRET efficiency.

1.3.3.1 Theoretical description of linker peptides

A comprehensive understanding of the linker peptide's properties is a crucial prerequisite for meaningful interpretation of TS experiments and a number of criteria have to be met by a

peptide to be suitable as force sensor [Freikamp et al., 2016, 2017]. First, the resting length must be short enough to ensure high FRET efficiency at zero force, while the force-induced length increase must be sufficient to cause significant loss in FRET. Second, forces of a few pico Newton (pN) must be sufficient to elongate the linker peptide. Third, elongation of the peptide must be reversible and should, fourth, be free of hysteresis (i.e. the behavior of the peptide at a given force should not depend on the forces previously experienced by the peptide). Finally, peptide unfolding should be insensitive to the velocity at which mechanical force is applied (i.e. loading rate).

Force dependent elongation of the linker peptide can follow two modes: either, the linker elongates gradually upon increasing forces and thus behaves very much like a mechanical spring, or it undergoes a defined unfolding event if a certain force threshold is exceeded.

1.3.4 Calibrated tension sensor modules

Similar to a normal spring scale, the sensitivity of each FRET-based TSM is limited to a specific force range and single molecule calibration is a crucial step in the development of a new TSM. As relevant forces are typically $< 50\,\mathrm{pN}$, optical tweezers (see fig. 1.9 A) are the preferred tool for such calibrations.

By the time this project was initiated, three single molecule calibrated TSMs were available in our lab, covering a total force range from 1 to 11 pN. The first calibrated TSM was published by Grashoff et al. [2010] and made use of the F40 peptide which is sensitive at 1–6 pN (fig. 1.11 A). In addition, two at that time still unpublished sensors had been developed in our lab, which both apply variants of the villin headpiece peptide HP35 as force sensitive linker (meanwhile published in Austen et al. [2015]). While the wt HP35 peptide is most sensitive to forces between 6 and 8 pN, a stabilized mutant HP35st requires 9–11 pN to unfold. The three sensors, their sensitivity–force correlation and the corresponding FRET–force correlations are shown in figure 1.11.

1.4 Biosensors in cells

1.4.1 Important considerations during experimental design and data evaluation

The first question that needs to be addressed when generating a new biosensor (i.e. a hybrid molecule that was generated by insertion of a TSM into the protein of interest (POI)), is the identification of an appropriate target site. The chosen insertion site must locate between two protein domains that experience forces with opposite directionality. Furthermore, the tertiary and quarternary protein structure must allow that region to elongate if under force.

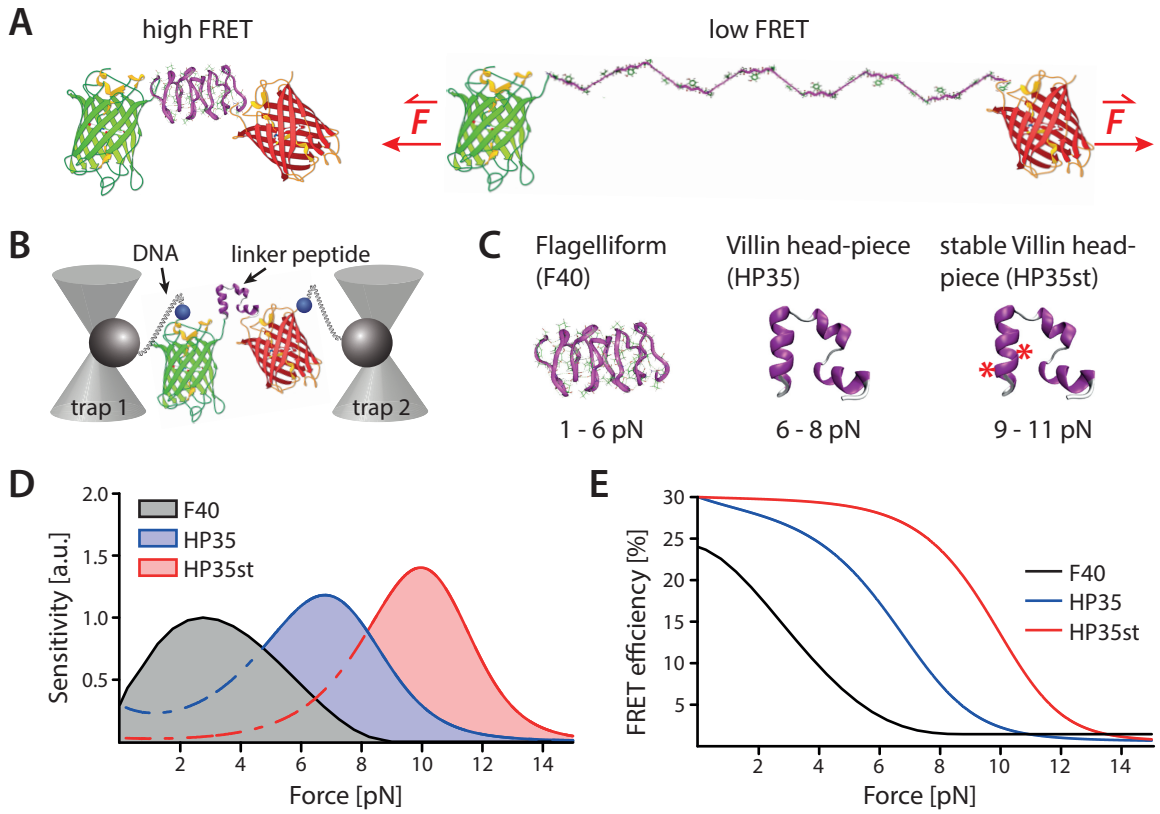

Figure 1.11: Calibration of pre-existing tension sensor modules. A) In the relaxed state, both fluorophores of the TSM are close together and FRET is high. If the module experiences linear force, the linker peptide as the weakest element elongates and FRET efficiency ceases. **B and C)** Calibration of the three TSMs by single molecule force spectroscopy as shown in B (see also [Austen et al., 2015]) revealed that all three modules together cover a force range from 1-11 pN. **D)** Sensitivity-force correlation for the three sensor modules as obtained by calibration. **E)** FRET-force correlation of the three modules calculated with the data shown in D and zero-force FRET efficiencies measured after cytosolic expression of the tension sensor module.

Before inference about actual forces can be made from a new biosensor, a number of biological parameters needs do be tested (reviewed by Cost et al. [2015]). The two most critical ones are (1) if the targeted molecule is still functional after TSM integration and (2) how much of the total FRET observed is due to inter-molecular FRET occurring between adjacent copies of the biosensor.

After data collection and evaluation, additional questions have to be kept in mind during data interpretation [Freikamp et al., 2016]. Most important is a careful reflection of the average FRET value. Relevant questions are: Could the total force be underestimated due to the co-expression of endogenous POI? Could it be that some molecules experienced forces that were below or above the dynamic range of the chosen TSM, both again resulting in an underestimation of the average force? And is the total force distributed equally across molecules, or do only a few molecules experience very high forces, while others are not under force at all?

1.4.2 FRET measurements

Four different methods are commonly used for the quantification of FRET: Sensitized emission, acceptor photobleach, ratiometric FRET and fluorescence-lifetime imaging microscopy (FLIM)-FRET; each with its own advantages and disadvantages [Gadella, 2009]. During the course of this project, FRET measurements of KTs were performed with the ratiometric method and FLIM was used for the characterization of new TSM candidates.

1.4.2.1 Ratiometric FRET

Ratiometric FRET is the fastest method for FRET quantification. Only two images are sufficient for the calculation of FRET ratios, namely donor emission after donor excitation and acceptor emission after donor excitation. The FRET ratio is then calculated as the quotient of acceptor to donor intensity.

As major advantage, ratiometric FRET can be quantified with only a single round of excitation, if performed on a system that allows simultaneous detection of two separated channels. This requirement is met by every CLSM, as this type of microscope is typically equipped with multiple detectors. On camera-based systems, a beam-splitter and a second camera can be introduced into the light-path.

The requirement to take only a single image is particularly advantageous if a sample moves fast (resulting in imperfect overlay of subsequently recorded images) or bleaches quickly. As a disadvantage, absolute FRET efficiencies cannot be directly determined by ratiometric FRET as acceptor bleedthrough and donor crosstalk are not separately quantified. Furthermore, ratiometric FRET critically relies on invariant relative concentrations of donor and acceptor fluorophore; however, this requirement is automatically met by TSMs due to the direct coupling of the donor and acceptor fluorophore.

1.4.2.2 FLIM-FRET

The term "fluorescence lifetime" refers to the time-delay between fluorophore excitation and photon emission. This stochastic process follows an exponential decay with a half-life τ that is highly specific for a particular fluorophore in a constant environment. If a fluorophore undergoes FRET, however, the alternative decay pathway leads to a reduction of τ [Austen et al., 2013]. After measuring the lifetime of the donor fluorophore alone (i.e. in the absence of an acceptor) τ_D and within the FRET construct τ_{DA}, the FRET efficiency can be directly calculated as

$$E = 1 - \frac{\tau_{DA}}{\tau_D}. \tag{1.2}$$

1.5 Cell division from a mechanical perspective

The first question that arises when looking at cell division from a mechanical perspective is: At which stages do KTs experience the highest force? During metaphase, when both sites of the mitotic spindle simultaneously pull at bi-oriented chromosomes? Or during anaphase, when the separated sister chromatids rapidly move apart? These considerations soon lead to follow-up questions, such as: Which parts of the mitotic spindle actually produce force and how are these forces distributed along the spindle? And is chromosome movement always a consequence of pulling forces, or are pushing forces involved as well?

Nicklas' pioneering experiments in meiotic grasshopper spermatocytes showed that the spindle machinery is capable of excreting forces of up to 700 pN during anaphase [Nicklas, 1983, 1988]. On the contrast, calculations based on the speed of chromosomes and their size suggest that only $\sim$0.1 pN are required to move chromosomes through a viscous environment like the cytoplasm [Nicklas, 1965]. Even though a more recent study that used a trapping laser to stop chromosome movement in *Mesostoma* and *crane-fly* spermatocytes determined the required forces to be approx. 100$\times$ lower than the value measured by Nicklas [Ferraro-Gideon et al., 2013], a remarkable discrepancy between experimental data and theoretical models remains. This suggests that the spindle produces not only the forces that actually move chromosomes in space, but also isostatic forces within the spindle. This idea is supported by the observation that MTs in the spindle periphery are curved in most cell types [Pavin and Tolić, 2016]. Considering the high persistence length of MTs, such an arrangement can only be explained with a model that includes compressing forces generated within the spindle by motorprotein mediated sliding of antiparallel polar MTs (see sec. 1.2.2) [Rubinstein et al., 2009]. Laser cutting experiments revealed that these compressing forces are balanced by bridging MTs, emerging from the k-fibers of two sisterchromatids but (similar to interpolar MTs) interacting with each other instead of binding the KT [Kajtez et al., 2016, Simunić and Tolić, 2016].

1.5.1 The mitotic spindle – Part II: Mechanisms of force generation

Chromosomes fulfill three types of movement during mitosis [Pavin and Tolić, 2016]. First, they are transported to the spindle equator (called chromosome congression), a process that goes in parallel with chromosome bi-orientation. Bi-oriented chromosomes that reached the equatorial plane exhibit oscillatory movements that are characteristic for metaphase. Finally, at anaphase, the separated sister chromatids are transported to opposite spindle poles by a combination of k-fiber shortening (anaphase A, [Asbury, 2017]) and spindle elongation (anaphase B [Scholey et al., 2016]).

1.5.1.1 Motor proteins versus dynamic microtubules

Motor proteins that directly slide chromosomes laterally along MTs play an important role during chromosome congression. Involved motors can be either minus- or plus-end directed and they act at kinetochore as well as on chromosome arms (comprehensively review by Maiato et al. [2017]). Different posttranslational tubulin modifications of astral, polar, and and KT–MTs serve as guiding tracks to direct the respective motors in the right direction [Barisic et al., 2015].

When KT–MT attachments mature, they are remodeled from lateral to end-on attachments [Maiato et al., 2017]. This tip-coupling is one of the most conserved features of mitosis [McIntosh et al., 2013], but the exact nature of these bonds and how they produce force is not yet well understood [Asbury, 2017]. It was shown that dynamic instability of MTs emerges as an important contributor of metaphase chromosome oscillations and anaphase transport of end-on attached chromosomes [Armond et al., 2015, Civelekoglu-Scholey et al., 2013, Pavin and Tolić, 2016]; but this alone does not rule out a persistent importance of KT-coupled motors as they could still connect to MT via long tethers [Asbury, 2017]. Injection of anti-dynein antibodies indeed slows down anaphase movements by ∼75 % in *Drosophila* embryos [Sharp et al., 2000] and ∼33 % in mammalian PtK1 cells [Howell et al., 2001]. Furthermore, free MT minus-ends generated by laser ablation are rapidly recognized as cargo by dynein/dynactin and pulled towards the spindle pole [Elting et al., 2014], demonstrating a general role of molecular motors for spindle organization.

More strikingly, however, are experiments that have been performed in budding and fission yeasts: after deletion of all KT-localized minus-end-directed motors, poleward KT movement could still be observed and was directly coupled to MT disassembly [Grishchuk and McIntosh, 2006, Tanaka et al., 2007]. These experiments in combination with the finding that the Ndc80 complex is essential for proper KT function and cell viability in all tested organisms [McCleland et al., 2003] clearly demonstrate that molecular motors are modulators of chromosome transport along MTs, but not the major generators of force.

1.5.1.2 Push or pull

Because chromatids move towards the spindle poles during anaphase, the responsible forces are intuitively expected to be pulling forces. However, polar MTs form dense networks that can – in extreme cases such as in *Xenopus laevis* egg extracts – contribute to more than 90 % of the total spindle mass [Forth and Kapoor, 2017]. Additionally, antiparallel MTs assemble between separating chromosomes during anaphase to form a central spindle. Together, these networks possess all mechanical properties that are required to push chromosomes during metaphase as well as during anaphase.

The dominant role of pulling forces during metaphase, however, could be demonstrated with laser microsurgery experiments. While sisterchromatid separation had no effect on the poleward moving KT, the trailing kinetochore abruptly stopped and, after a short delay, eventually reversed its original directionality and moved poleward [Khodjakov and Rieder, 1996].

On the contrary, pushing of chromosomes by the central spindle was found to be an important driver for anaphase chromosome segregation in *Caenorhabditis elegans* mitosis and meiosis [Laband et al., 2016, Yu et al., 2016], and preliminary results indicated that the same process could also be relevant in human mitotic tissue culture cells [Yu et al., 2016]. Pushing and pulling mechanisms, however, are not mutually exclusive. In the vast majority of cell types, KTs lead anaphase movements while the chromosome arms follow [Asbury, 2017]. In such a constellation, pushing forces could reduce DNA strain by helping the chromosome arms to follow the centromere.

1.5.1.3 Dynamic instability and microtubule flux

Even though plus-ends of MTs reveal higher dynamics than minus-ends, polymerization and depolymerization can occur at either end. In the light of sustained end-on attachments to dynamic MTs, the question arises if MT dynamics primarily occur at the KT-embedded plus-end, or at the minus-end, which either connects to the centrosome or laterally to other MTs within the spindle. Notably, net depolymerization can occur even in phases of active polymerization at the plus-end, as long as the rate does not exceed the depolymerization rate at the minus-end. As individual segments of the polymer flow backward in such a dynamic, this behavior is termed "MT flux".

Photoconvertible fluorescent proteins enabled the marking of defined MT segments in life cells and thus the analysis of MT flux in k-fibers. Experiments in different organisms revealed that the contribution of flux to poleward KT movement varies widely in different cell types [Asbury, 2017]. These results are of great interest in the context of putative molecular mechanisms for harnessing the force that is produced by shrinking MTs. In particular, two mechanisms have been proposed (fig. 1.12). The "conformational wave" hypothesis assumes binding of KTs to the curved protofilaments, enabling the KT to literally surf along the peeling MT. The "biased diffuse" hypothesis requires a cluster of multiple MT-binding proteins. Within the cluster, each individual molecule stochastically binds and unbinds while undergoing thermal diffusion during unbound phases; simultaneous MT disassembly then leads to biased diffusion [Asbury et al., 2011].

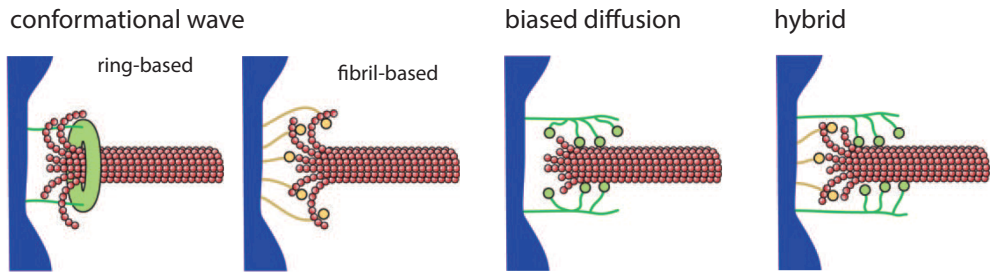

Figure 1.12: Force generation by microtubule depolymerization. Kinetochores directly harness the energy delivered by MT dynamics, without the necessity for conventional motor proteins. A ring-based and a fibril-based version of the conformational wave mechanism have been postulated. Both assume a mechanism of force generation that is directly coupled to the curved protofilament tips of depolymerizing MTs. The biased diffusion mode requires the cooperative action of multiple fibrils that rapidly bind and unbind to straight MTs. Thermal fluctuations of the chromosome combined with MT depolymerization produces a pulling force. The two mechanisms are not mutually exclusive. Images are reproduced with permission from Asbury [2017].

1.5.2 Molecular force measurements *in vitro*

Laser traps have been used to study the interaction of KT proteins or protein complexes with MTs *in vitro*, with a particular focus on the yeast proteins Ndc80(Hec1) and Dam1. When immobilized on beads at sufficiently high concentration, both Ndc80 and Dam1 alone can form load bearing attachments to MTs that support forces up to 3 pN, but showed rather low processivity [Asbury et al., 2006, Powers et al., 2009]. Combining both proteins, however, greatly enhanced processivity and increased the tolerated force to 4.4 pN on average with an observed maximum of 9 pN [Tien et al., 2010]. Even grater forces were observed when pure Dam1 was coupled to beads not directly but via 100 nm long tethers. Such a connection allowed the formation of true end-on attachments that withstood loads of up to 30 pN [Volkov et al., 2013].

In another study that used whole KT particles obtained from budding yeast, load-bearing attachments of individual particles with dynamic MTs sustained for > 30 minutes. A catch-bond behavior between 1 and 5 pN was observed, and the maximal tension measured was 11 pN [Akiyoshi et al., 2010]. They further found a stabilizing effect of load-bearing KT particles on MTs through inhibited catastrophe and promoted rescue.

Even though structurally unrelated, the human Ska complex is seen as a functional homologue of the yeast Dam1 complex [Musacchio and Desai, 2017]. Kinetochore-bound Ska1 complex preferentially binds to curved protofilaments and tracks depolymerizing MTs Schmidt et al. [2012]. Ska depletion increased the frequency of force dependent detachments from KTs to MTs [Auckland et al., 2017], but direct force measurements have not yet been undertaken.

A kinetochore component that attracted attention only recently is the 400 kDa protein CENP-F, that localizes to the fibrous corona [Musacchio and Desai, 2017]. Besides its role in chromosome congression, it has been associated with a number of functions during interphase [Pfaltzgraff et al., 2016]. After discovering that CENP-F binds with high preference to curved tubulin oligomers, Volkov et al. [2015] analyzed its role as potential KT force coupler. Indeed, they found that CENP-F can follow disassembling MTs and transduce forces of 3–5 pN on average, with peak forces of 10 pN. Unfortunately, not much is known about CENP-F's conformation and interactions with other proteins *in vivo*, but future analysis will hopefully reveal interesting insights about this newly discovered component of the KT force generating machinery.

An entirely different approach for the calculation of KT forces was followed by Chacón et al. [2014]: Fluorescent markers were used to measured pericentromere stiffness and stretch by tracking thermal movements in yeasts. With these data, the authors calculated that pericentromere tension lies in the range of 4–6 pN.

1.5.3 Molecular force measurements *in vivo*

During the course of this project, two studies were published that used FRET-based sensors to analyze the yeast Ndc80 complex [Suzuki et al., 2016] and *Drosophila* CENP-C [Ye et al., 2016].

Suzuki et al. [2016] report that forces across the Ndc80 complex increase between interphase and metaphase, with intermediate levels during prometaphase. FRET ratios of early and mid anaphase as well as telophase were comparable to those measured in interphase; however, the highest FRET ratios (and therefore lowest force) was detected at late anaphase. This observation is interpreted by the authors such that yeast KTs remain under tension at interphase, mediated by maintained Ndc80-dependent attachments to ∼50 nm long MTs. The study further correlated Ndc80 tension to MT dynamics. In line with the delta-measurements by Dumont et al. [2012], they found forces to be higher in polymerizing than in depolymerizing MTs and postulate that Ndc80 and Dam1 act together as a dual force coupler. This hypothesis is supported by *in silico* simulations and *in vivo* experiments using a Dam1 mutant with reduced MT binding ability.

Unfortunately, the study used an entirely uncalibrated sensor module, comprising an mYPet–mECFP pair connected by a 12 amino acid (aa) linker resulting from translation of the expression vector's multiple cloning site (MCS). The authors argue that these 12 aa together with 5 and 11 unstructured aa from the N and C termini of the fluorophores form an entropic spring that serves as force sensitive linker, but this assumption has not been ex-

perimentally tested. Furthermore, the sensor module was incorporated into the Ndc80/Nuf2 coiled-coil region. It is therefore questionable, if the observed changes in FRET are indeed due to a length increase, or rather caused by rotational confinement. Unfortunately, also effects of protein conformation on the sensor's FRET efficiency was not investigated. It has to be noted, however, that the data obtained from wtNdc80 and Ndc80 tail mutants together with Dam1 mutants form a conclusive picture. It can therefore be assumed that the sensor indeed monitors changes in Ndc80 tension – either by elongation, or by a conformational change that (by coincidence) affects FRET efficiencies in the same manner as expected for length-dependent effects.

The second study by Ye et al. [2016] incorporated the F40 TSM into *Drosophila* CENP-C. As mentioned in section 1.2.3.3, *Drosophila* KTs are rather unusual in the sense that most CENPs, and in particular CENP-T, are missing, making CENP-C the main connector between inner and outer KT [Musacchio and Desai, 2017]. The authors found a statistically significant decrease of FRET efficiency from 23.6 % at interphase to 20.7 % during metaphase, which was dependent on MT dynamics but not o the minus-end directed motor dynein. To generate a second, independent sensor, a part of the talin rod domain including five cryptic vinculin binding sites was inserted into the CENP-C tail. Single molecule experiments had shown a force dependent recruitment of vinculin to the binding sites that gradually became accessible. After co-expression of this sensor and GFP-tagged vinculin in S2 cells, the fluorescence intensity of vinculin was used as readout for CENP-C tension. Using these two sensors, the authors calculated average forces of 1.2–1.4 pN and < 2 pN for the F40 and talin/vinculin sensor, respectively. However, it has to be noted that these values might underestimate CENP-C forces, as both sensors were expressed on top of endogenous (and thus possibly shorter) CENP-C.

1.6 Aim of the thesis

The forces that drive cell division have been the focus of researchers for many decades, but yet, a comprehensive picture remains elusive. A major reason for our limited knowledge is the lack of techniques that allow direct and quantitative tension measurements at the KTs of living cells. A number of indirect indicators for KT tension have been proposed over the years, but doubts about the validity of these surrogate markers have been raised. The most widely used marker is intra-KT stretch, but due to a proposed combination of passive and active force generating sites, these experiments are difficult to interpret [Dumont et al., 2012]. Furthermore, it has been questioned if intra-KT stretch is indeed due to tension-dependent stretch, or rather caused by local rearrangement [Joglekar, 2016] and insufficient 2D projections [Smith et al., 2016].

The development of a method that allows the direct investigation of molecular forces at the KT is particularly interesting with regard to the longstanding debate about the initial signal that activates the SAC as well as error correction mechanisms within the mitotic spindle. The central aim of this thesis was thus the development of a FRET-based molecular biosensor and corresponding data analysis procedures for KT tension measurements. As currently available sensors showed a very limited resolution for forces in the lower single pN regime, a new sensor module with greatly enhanced resolution between 3–5 pN was developed and characterized. Existing and newly developed sensors were then applied to analyze forces across the KT protein CENP-T.

2 Methods

2.1 Molecular biology methods

2.1.1 Buffer and media for molecular biology

2.1.1.1 Bacterial growth media

Liquid broth (LB) medium and LB-agar plates were either prepared according to the recipe in tbl. 2.1, or with granulated LB Broth from Carl Roth (LB-Medium, Cat.# 6673.2, 10 g/400 mL; LB-Agar, Cat.# 6675.2, 16 g/400 mL).

Table 2.1: LB medium

NaCl	10 g
Tryptone-peptone	10 g
Yeast extract	5 g
ddH_20	*ad* 1 L
For plates, add 15 g agarose per 1 L	

Table 2.2: Antibiotics for LB medium

Ampicillin (Amp)	50 µg/mL
Kanamycin (Kana)	25 µg/mL
Tetracycline (Tet)	10 µg/mL

Table 2.3: TSS buffer for competent bacteria

Component	Final concentration	Amount
Tryptone-peptone	1.0 % (w/v)	5.0 g
Yeast extract	0.5 % (w/v)	2.5 g
NaCl	100 mM	2.5 g
PEG[a]	10 % (w/v)	50 g
DMSO[b]	5 % (v/v)	25 mL
1 M $MgCl_2$	50 mM	25 mL
ddH_2O (to pH 6.5)		*ad* 500 mL
Sterile filtrate and store at 4 °C		

[a] Polyethylenglycol, MW 3000/3500

[b] Dimethylsulfoxid

2.1.1.2 Buffer for molecular biology

Table 2.4: 50× TAE buffer

Tris-base	242 g
Glacial acetic acid	57.1 mL
EDTA	37.2 g
ddH_20	*ad* 1 L

Table 2.5: 1× TE buffer

Tris (bring to pH 8)	10 mM
EDTA	1 mM

Table 2.6: 6× DNA loading buffer

Glycerole ($\geq$ 99 %)	60 % (v/v)
EDTA	60 mM
Bromphenole blue	0.1 % (w/v)
Orange G	0.2 % (w/v)
Xylene cyanol FF	0.1 % (w/v)
Tris-HCl, pH 7.6	10 mM

2.1.2 Generation of recombinant DNA and expression constructs

2.1.2.1 cDNA, plasmids, and oligonucleotides

cDNA sources

Table 2.7: Origin of cDNA constructs

Gene	GenBank code or source
human Hec1	NM_006101.2
human Nuf2	AB050577.1
human Spc25	NM_020675.3
human talin-1	NM_006289.3
chicken CENP-T	Gift from T. Fukagawa
YPet [a]	pCEP4YPet-MAMMP
mCherry	AY678264
mCerulean3	AFR60232.1
mRuby2	AFR60232.1

[a] A shortened YPet lacking the last 11 amino acids has been used in order to increase the resting FRET efficiency of tension sensor modules.

Linker peptide sequences

F40 (flagelliform)

```
5'- GGG CCA GGT GGA GCA GGG CCA GGT GGT GCA GGG CCA GGT GGT GCA GGG CCA GGT
     G   P   G   G   A   G   P   G   G   A   G   P   G   G   A   G   P   G

    GGT GCA GGG CCC GGT GGT GCA GGT CCA GGT GGT GCA GGT CCA GGT GGT GCT GGT
     G   A   G   P   G   G   A   G   P   G   G   A   G   P   G   G   A   G

    CCA GGT GGT GCT -3'
     P   G   G   A
```

HP35 (villin headpiece)

```
5'- CTG AGC GAT GAG GAC TTC AAA GCT GTG TTT GGC ATG ACC AGG TCC GCA TTT GCC
     L   S   D   E   D   F   K   A   V   F   G   M   T   R   S   A   F   A

    AAT CTT CCT CTG TGG AAA CAA CAG AAC CTG AAG AAG GAA AAG GGA CTC TTC -3'
     N   L   P   L   W   K   Q   Q   N   L   K   K   E   K   G   L   F
```

FL (ferredoxin-like fold)

```
5'- ATG GGC GAG TTT GAC ATC CGG TTT CGG ACT GAT GAC GAC GAA CAG TTC GAG AAA
     M   G   E   F   D   I   R   F   R   T   D   D   D   E   Q   F   E   K
```

```
GTG CTG AAG GAG ATG AAT CGT CGA GCC AGA AAG GAT GCT GGA ACT GTG ACC TAC
 V   L   K   E   M   N   R   R   A   R   K   D   A   G   T   V   T   Y

ACA AGG GAT GGG AAT GAC TTC GAG ATT CGC ATT ACC GGC ATA AGC GAG CAA AAC
 T   R   D   G   N   D   F   E   I   R   I   T   G   I   S   E   Q   N

CGC AAA GAA CTG GCC AAA GAG GTT GAA AGG CTT GCA AAG GAA CAG AAC ATC ACA
 R   K   E   L   A   K   E   V   E   R   L   A   K   E   Q   N   I   T

GTC ACG TAT ACC GAG AGA GGT TCC CTC GAA -3'
 V   T   Y   T   E   R   G   S   L   E
```

EF(short) (EF hand motives 3 and 4 of human α-actinin)

```
5'- GCC GAA CAG GTG ATA GCC TCC TTT CGG ATC TTG GCA AGC GAC AAA CCC TAC ATT
     A   E   Q   V   I   A   S   F   R   I   L   A   S   D   K   P   Y   I

    CTG GCT GAA GAG CTG AGA AGG GAG CTT CCT CCC GAT CAA GCC CAG TAC AGC ATC
     L   A   E   E   L   R   R   E   L   P   P   D   Q   A   Q   Y   S   I

    AAG CGC ATG CCG GCT TAC TCT GGA CCA GGG TCA GTC CCT GGT GCT CTC GAC TAT
     K   R   M   P   A   Y   S   G   P   G   S   V   P   G   A   L   D   Y

    GCG GCA TTC TCC AGT GCC CTG TAT GGC -3'
     A   A   F   S   S   A   L   Y   G
```

Vectors for cloning and cDNA expression

The retroviral expression vectors pLPCX (puromycin and ampicillin resistance) and pLNCX (neomycine, ampicillin) were used for all constructs made for expression in mammalian cells. Constructs designated for DT40 cells were cloned into the high copy vector pcDNA3.1(+) (neomycin, ampicillin). pBluescript II SK(+) (ampicillin) was used as cloning vector for large constructs, which could not be assembled directly in the expression vector.

2.1.2.2 PCR

Recombinant plasmids were generated by restriction enzyme based cloning strategies. Restriction sites were added by polymerase chain reaction (PCR), using primers with appropriate overhangs. cDNA sequences with internal restriction sites for TSM integration were generated by overlap extention PCR as described in Austen et al. [2013].

PCR was performed with *PfuUltra*™ II Fusion HS DNA Polymerase (Agilent Technologies) according to the manufacturers protocol. Touch-down temperature gradients were used to increase specificity.

Table 2.8: PCR reaction mix

Component	Stock	Final conc./amount	Vol. used
Template (plasmid DNA)		5–30 ng	x µL
Forward primer	10 µM	0.2 µM	1 µL
Reverse primer	10 µM	0.2 µM	1 µL
dNTPs	10 mM each	200 µM each	1 µL
10× *PfuUltra* II reaction buffer	10×	1×	5 µL
ddH_2O			*ad* 100 µL

Table 2.9: Touchdown PCR program

Step	Temperature	Duration	Loops	ΔT/loop
1	95 °C	180 sec		
2	95 °C	20 sec		
3	68 °C [a]	20 sec	8×	-1 °C
4	72 °C	15 sec/1 kb		
5	95 °C	20 sec		
6	60 °C [a]	20 sec	30×	
7	72 °C	15 sec/1 kb		
8	4 °C	∞		

[a] Temperature was adapted according to the primer's T_M

2.1.2.3 DNA digest and vector dephosphorylation

Recombinant vectors were generated by classical cloning procedures and enzymes producing *sticky ends*. Restriction enzymes and reaction buffers were purchased from New England BioLabs, and digestions were typically incubated for 1 h at 37 °C (exceptions of specific enzymes apply). Double- and triple digests were performed in the buffers recommended by the manufacturer's Double digest finder (https://www.neb.com/tools-and-resources/interactive-tools/double-digest-finder).

To avoid religation of the vector during later steps of cloning, two non-compatible restiction enzymes were used for the 5'-prime and 3'-prime end whenever possible. Additionally, 5'-prime phosphates were removed from linearized vectors by CiP (alkaline phosphatase,

New England Biolabs). To this end, 1 µL CiP was added directly to the digestion mix after the digest was completed, and the mix was incubated for another 30 min at 37 °C. Then, another 1 µL was added and once more incubated for 30 min at 37 °C. After incubation with CiP, cut DNA was purified on agarose gels.

Table 2.10: Enzymatic DNA digest

Component	Stock	Final amount	Vol. used
DNA		1.5 µg	X µL
Buffer[a]	10×		3 µL
(BSA[b]	20×		1.5 µL)
Enzymes (each)			0.5 µL
ddH_2O			*ad* 30 µL

[a] According to the manufacturer's recommendation

[b] Not required with all buffers

2.1.2.4 Agarose gel electrophoresis and DNA purification

PCR amplificates and cut vectors were purified by default on 1 % agarose gels, following standard protocols. If several very large or small constructs were to be separated from each other, concentrations of 0.8–2 % were used accordingly. Gels ran with 80–130 V, depending on chamber size. To avoid overloading and obtain clear bands, max. 1.5 µg DNA were loaded per well. Recipes for buffers and DNA loading dye are listed in sec. 2.1.1.2.

DNA purification from agarose gels was done with the commercially available NucleoSpin® Gel and PCR Clean-up (Machinery-Nagel) kit and according to the manufacturer's protocol. DNA concentrations were determined using a NanoDrop 2000 UV-Vis (Thermo Fischer) and DNA was stored in the elution buffer provided with the kit at 4 °C (short term) or -20 °C.

2.1.2.5 DNA ligation

Linearized vectors and cDNA inserts were ligated using T4 ligase (New England BioLabs) and a vector:insert ratio of 1:3 (calculated with http://www.insilico.uni-duesseldorf.de/Lig_Input.html). The ligation mix was incubated by default for 1 h at room temperature (RT); if results were not satisfactory (e.g. because of a very long insert), ligations were incubated over night (o/n) at 16 °C. After ligation, DNA was either stored at -20 °C, or directly used for transformation.

Table 2.11: DNA ligation

Component	Final conc./amount	Vol. used
Vector	0.02 pmol	x µL
Insert	0.06 pmol	x µL
10× T4 ligase buffer		1.5 µL
T4 enzyme		1 µL
ddH_2O		*ad* 15 µL

2.1.3 Generation and transformation of competent bacteria

Generation of competent bacteria

The phage-resistant *E. coli* strain OmniMAX™ (Invitrogen) was used for the amplification of plasmid DNA. To generate competent bacteria, a single clone was picked form an LB (+Tet) plate to grow a 10 mL starter culture (+Tet) at 37 °C o/n (note: all liquid bacteria cultures were grown in orbital shakers; cultivation temperature for liquid cultures and plates was always 37 °C). In the morning, 100 mL warm LB (without antibiotics) were inoculated with 2 mL of the starter culture and grown until $OD_{550} \approx 0.5$. Next, the culture was incubated on ice for 10 min, transferred to pre-chilled autoclaving tubes, and spun for 15 min at 1100×g and 4 °C. Pellets were resuspended in a total of 10 mL ice cold TSS buffer (see sec. 2.1.1.1) and 2.5 mL glycerole (87 %) were added to the resuspension. Cells were then aliquoted (50–200 µL per tube), shock frozen in liquid nitrogen, and stored at -80 °C for no more than six months.

Transformation of competent bacteria

Competent bacteria were taken form -80 °C and directly placed on ice. 10 µL ligation mix was added to 100 µL of freshly thawed bacteria and, after gentle mixing, incubated on ice for 30 min. Plasmid uptake was facilitated by a 50–90 sec heat shock at 42 °C, directly followed by 3 min recovery on ice. Then, warm LB medium (10× the bacterial volume) without antibiotics was added and incubated for 45–60 min at 37 °C with gentle shaking. After recovery, bacteria were pelleted at 6 000×g for 3 min. The pellet was resuspended in 100 µL LB and plated on a prewarmed LB plate supplemented with antibiotics (see tbl. 2.2) and grown at 37 °C o/n.

For retransformation of plasmids, 0.5–1 µg plasmid DNA was added to 100 µL bacteria. After heatshock and recovery, 50 µL bacteria solution were plated without prior centrifugation.

2.1.4 Plasmid amplification, isolation, and verification

Analytical scale (Miniprep)

For analytical purpose, single colonies were picked form LB plates and grown in 3 mL cultures for at least 7 h or o/n. 2–3 mL of these cultures were pelleted (6 000×g, 3 min). Pellets were either frozen at -20 °C, or directly used for subsequent plasmid isolation with the NucleoSpin® Plasmid EasyPure kit (Machinery-Nagel). Concentration and purity of plasmid DNA was determined using a NanoDrop 2000 UV-Vis (Thermo Fischer), and samples were stored at 4 °C (short term) or -20 °C (long term).

Preparative scale (Maxiprep)

For preparation of larger amounts of plasmid, cultures of 100–150 mL (high copy plasmids) or 200–250 mL (low copy plasmids) were grown over night and pelleted at 5 000×g for 15 min at 4 °C. Pellets were either stored at -20 °C or used for plasmid isolation with NucleoBond® Xtra Midi Plus kit (Machinery-Nagel).

Verification and sequencing

Plasmids were checked by analytical digest (1.5 µg DNA, protocol as described in sec. 2.1.2.3) and agarose gelelectrophoresis (sec. 2.1.2.4), the obtained fragments were compared to size expected in accordance with the plasmid map. Clones selected for later use were further confirmed by DNA-sequencing, using Mix2Seq kits (Eurofins Genomics). DNA amount per sequencing tube was 0.75–1.5 µg plasmid and 20 pmol primer in a total volume of 17 µL.

Glycerole stocks

Glycerole stocks were made by adding 400 µL glycerole (≥ 99 %) to 600 µL dense bacterial culture and stored at -80 °C.

2.1.5 Identification of protein targeting sites

When designing a new biosensor, the site for integration the tension sensor module (TSM) into the protein of interest (POI) has to be carefully chosen to fulfill several criteria. First, the targeted protein domain must be in a region that can be expected to be under tension. This is easiest realized for proteins of elongated structure and distinct protein interaction domains at either terminus. Second, the local environment and quarternary protein structure must not prevent the POI (and with it, the TSM) from stretching when under force. Third, all proteins domains of the biosensor (including the TSM) must fold properly; and fourth, the protein must remain biologically functional despite TSM integration.

As no full-length structural information was available for any of the targeted proteins, promising domains were identified based on a number of indicators. Previously published results of crosslinking-mass spectrometry (MS) and *in vitro* pulldown assays were used to

locate interaction sites with other proteins or protein complexes. Regions of low conservation were identified by BLAST analysis of the protein sequences from very closely to more distantly related species. Additionally, the RaptorX structure prediction algorithm [Källberg et al., 2012] was used to obtain information about the secondary protein structure, and lastly, the local amino acid (aa) composition was taken into consideration. TSMs were then integrated at sites that showed low conservation, were likely to be disordered, and surrounded by glycine, alanine, valine, leucine, isoleucine, valine, serine, threonine, and proline.

2.2 Cell culture methods and protocols

2.2.1 General material for cell culture

Table 2.12: General material for cell culture

Product	Company	Cat.#
5 ml Pipette, Costar Stripette	Corning Inc.	4487
15 ml Pipette, Costar Stripette	Corning Inc.	4488
25 ml Pipette, Costar Stripette	Corning Inc.	4489
50 ml Pipette, Costar Stripette	Corning Inc.	4490
96 well plate, round bottom	Corning Inc.	35 3799
96 well plate, flat bottom	Corning Inc.	35 3596
24 well plate	Corning Inc.	35 3524
12 well plate	Corning Inc.	35 3043
6 well plate	Corning Inc.	35 3046
15 ml centrifuge tube	Corning Inc.	43 0791
50 ml centrifuge tube	Corning Inc.	43 0829
Cryogenic vials	Corning Inc.	43 0489
Petry dish 35 mm	Sarstedt	82.1135
100 mm cell culture dish	Corning Inc.	35 3003
Cell culture flask 25 cm^2	Corning Inc.	35 3108
Cell culture flask 75 cm^2	Corning Inc.	35 3136
Cell culture flask 175 cm^2	Corning Inc.	35 3118
Steriflip-GP 0.22 µm filter	Merck	SCGP00525
Syringes 20 mL	B. Braun	4606736V
Microscope slides	Gerhard Menzel GmbH	J1800AMNZ
Glass coverslips #1.5	Gerhard Menzel GmbH	0284

2.2.2 Media, additives and buffer for cell culture

Table 2.13: Commercial media and buffer for cell culture

Product	Company	Catalog#
Dulbecco's Balanced Salt Solution (DPBS)[a]	Gibco	14190-169
Phosphate Buffered Saline (tablets)[a]	Sigma	P4417
RPMI Medium 1640, GlutaMAX, Phenol Red	Gibco	61870-044
RPMI Medium 1640, ØGlutamine, ØPhenol Red	Gibco	32404-014
DMEM, 4.5 g/L D-Glucose, GlutaMAX, Pyruvate, Phenol Red	Gibco	31966-047
DMEM, 4.5 g/L D-Glucose, L-Glutamine, 25 mM HEPES	Gibco	21063-045
Opti-MEM, GlutaMAX, Phenol red	Gibco	51985-026
GlutaMAX	Gibco	35050-061
Fetal Bovine Serum (FBS)	Gibco	10270-106
FBS, Tet-approved Lot# 41F2646K	Gibco	10270-106
Tet System Approved FBS	Clontech	631106
Chicken Serum	Gibco	16110-082
Trypsin 0.5 % (10×)	Gibco	15400-054
Pyruvate 100 mM	Gibco	11360-088
HEPES 1 M (100×)	Gibco	15630-056
Pen Strep (10000 U/mL Penicillin, 10000 µg/mL Streptomycin	Gibco	15140-163
geneticin (G418)	Sigma	A1720
Trypan Blue Solution (0.4 %)	Sigma	T8154

[a] Ready-to-use PBS or PBS made from tablets was used for cell culture applications. For all other purposes, self-made PBS (tbl. 2.14) was used.

Table 2.14: PBS

Component	Weight used	Final conc.
NaCl	8.01 g	137 mM
KCl	0.20 g	2.68 mM
KH_2PO_4	0.24 g	1.73 mM
$Na_2HPO_4 \times 12H2O$	3.63 g	10 mM
ddH_2O (to pH 7.4)		*ad* 1 L

HeLa growth and freezing media

- Growth medium: 500 mL RPMI 1640, 50 mL FBS, 5 mL pyruvate.
- Freezing medium: 50 mL growth medium, 40 mL FBS, 10 mL DMSO
- Imaging medium: 500 mL RPMI 1640 (ØGlutamine, Øphenole red) + 5 mL GlutaMAX + 12.5 mL HEPES (1 M)

Talin$^{-/-}$ and Vinculin$^{fl/fl}$ growth and freezing media

- Growth medium: 500 mL DMEM high glucose, 50 mL FBS
- Freezing medium: 50 mL growth medium, 40 mL FBS, 10 mL DMSO
- Imaging medium: 500 mL DMEM high glucose + HEPES (Øphenole red), 50 mL FBS

DT40 growth and freezing media

- Growth medium: 500 mL DMEM high glucose, 50 mL FBS(ØTet), 7 mL chicken serum, 2 µL β-mercaptoethanol
- For stable cell lines: add 1 g G418 (in 20 mL 1 M HEPES, pH 7.4) per 500 mL medium
- For CENP-T knockdown: add 2 µg/mL docyxycline just before use
- Freezing medium: 90 mL FBS(ØTet), 10 mL DMSO
- Imaging medium: 500 mL DMEM high glucose + HEPES (Øphenole red), 50 mL FBS(ØTet), 7 mL chicken serum, 2 µg/mL doxycycline (added just before use)

Penicillin and Streptomycin

Antibiotics were used while new cell lines were established to minimize the risk of contamination. As soon as sufficient aliquots were cryo-conserved, cells were cultured without antibiotics.

2.2.3 HeLa cell culture and cell line generation

HeLa cells were obtained from CSL cell line service (passage 43, Lot# 300194-1212, 1.5 ml, 2×10^6 cells). Cells were grown at 37 °C and 5 % CO_2 in a humidified incubator.

2.2.3.1 Passaging, thawing, and freezing

Passaging

Cells were grown at 25–95 % confluency and passaged every 2–3 days. Before passaging, cells were washed twice with PBS, then 1 mL of 0.05 % trypsin was added per 75 cm^2 surface area. Cells were incubated at 37 °C until detached, and resuspended in growth medium. To sufficiently inactivate the trypsin, at least 4× more medium than trypsin was used. Resupended cells were split to fresh culture flasks or dishes at ration of 1:4–1:6.

After 6–8 weeks (20–25 passages), cells were discarded and a new vial was thawed.

Thawing and freezing

Frozen cells were thawed in a 37 °C water bath and diluted in 5 mL growth medium. DMSO was removed by centrifugation (300×g, 5 min). The pellet was resuspended in 10 mL growth medium and transferred in a 75 cm^2 culture flask.

For freezing, cells were trypsinated, pelleted, and resuspended in freezing medium to 1×10^6 cells/mL. Aliquots of 1–1,5 mL were transferred to cryotubes and placed at -80 °C. After 5–7 days, cells were transferred to liquid nitrogen.

2.2.3.2 Transient transfection

Lipofectamine LTX with Plus-Reagent (Thermo Fisher) was used for transient transfection of HeLa cells. In a 12-well format, 1.5×10^5 cells were seeded per well 0.5 days prior to transfection. For one well, 5 µL Lipofectamine LTX and 2.5 µL Plus-Reagent as well as 2.5 µg pasmid DNA were diluted in Opti-MEM and mixed according to the manufacturer's instructions. After 6 h, the transfection mix was removed, cells were washed once with PBS and normal growth medium was added. Cells were analyzed 24–72 h after transfection.

2.2.3.3 Generation of stable cell lines

Stable cell lines were generated using the Gryphon helper-free retrovirus producer cell system (Nolan Lab, Stanford) and a biological safety level 2 laboratory and according to the following protocol.

• Day 0 (evening): Gryphon cells are seeded on 10 cm dishes at 60 % confluency.

• Day 1 (morning): Just before transfection, replace medium of Gryphon cells by 7 mL fresh growth medium supplemented with 4 µL of 50 mM chloroquine (Sigma, Cat. # C6628). Per dish, dilute 40 µg plasmide DNA with ddH_2O to a total volume of 439 µL and mix with 61 µL of 2 M $CaCl_2$ solution. Add this solution dropwise while vortexing to 500 µL 2× HBS buffer (tbl. 2.15). Add the resulting volume of 1 mL to the Gryphon cells and mix by gentle shaking. After 8 h of incubation, replace by fresh growth medium.

• Day 2 (morning): Replace medium of Gryphon cells with 8 mL fresh growth medium. Recipient HeLa cells are seeded at 20 % confluency into 10 cm dishes.

• Day 2 (evening): Remove medium of recipient HeLa cells. Collect virus-containing medium from Gryphon cells, add 8 µL polybrene, and sterile filtrate onto HeLa cells. Add 8 mL fresh growth medium to Gryphon cells.

• Day 3 and day 4 (morning and evening): Repeat virus infections as done in the evening of day 2, until a total of 4–5 rounds of infection have been completed.

After the last infection, cells recovered for 24 h. Positive cells were then selected with either 0.5 µg/mL puromycin for 3 days, or 500 µg/mL neomycin/G418 for at least 10 days, depending on the vector.

Table 2.15: 2×HBS buffer

Component	Weight used	final conc.
NaCl	1.64 g	280 mM
HEPES	1.19 g	50 mM
Na_2HPO_4	21.29 mg	1.5 mM
ddH_2O (to pH 7.0)		*ad* 100 mL

2.2.3.4 Cell cycle synchronization of HeLa cells

To increase the number of mitotic cells during imaging experiments, the transient transfection protocol was combined with a single round of thymidine block. To this end, cells were treated for 18–24 h with 2 mM thymidine, starting one day after Lipofectamine transfection. Cells were released from the S-phase block by thymidine washout and imaged 8.5 h later.

2.2.4 DT40 cell culture and cell line generation

Chicken DT40 cells with tetracycline-inducible knockdown of CENP-T were a gift from the lab of Tatsuo Fukagawa (Graduate School of Frontier Biosciences, Osaka University, Japan) and have been described in Hori et al. [2008]. As derived from a B-cell lymphoma, DT40 cells grew in suspension at 37 °C and 5 % CO_2 in a humidified incubator.

2.2.4.1 Passaging, freezing, and thawing

Passaging

Cells were grown at densities between 0.5–5×10^6 cells/mL in upright standing cell culture flasks. To allow sufficient oxygen transport, medium levels in the flasks did not exceed 1 cm. Cells were split every 2–3 days by 4–8 times dilution. For complete replacement of the growth medium, cells were pelleted at 200×g for 5 min and resuspended into fresh medium.

CENP-$T^{Tet\text{-}off}$ cells not stably expressing biosensors were cultured in medium containing neither tetracycline or doxycycline, nor G418. Stable cell lines were grown under constant addition of doxycycline (2 µg/mL, always added freshly to the medium) and G418 (2 mg/mL).

Thawing and freezing

Frozen vials were thawed at 37 °C and resuspended in 5 mL fresh growth medium. DMSO from the freezing medium was removed by pelleting cells for 5 min at 200×g, afterwards, cells were resuspended to 1×10^6 cells/mL.

For cryoconservation, cells were pelleted and resuspended in freezing medium to a density of 1×10^7 cells/mL. 1 mL was aliquoted per vial and frozen at -80 °C. After 5 days, cells were transferred to liquid nitrogen.

2.2.4.2 Generation of stable cell lines

Stable cell lines were generated by electroporation with the Amaxa Nucleofector Kit T (Lonza) and subsequent selection with antibiotics.

30 µg plasmid DNA were linearized for 6 h with PvuI (New England BioLabs) in a total volume of 100 µL, containing 2 µL enzyme. PvuI cuts within the ampicillin resistence gene of the pcDNA vector, thus not destroying any sequence relevant for cDNA expression in eukaryotic cells. Linearized DNA was directly purified using the NucleoSpin® Gel and PCR Clean-up (Machinery-Nagel) kit. To not exceed the column binding capacity, each sample was distributed onto two columns, both columns were then eluted into a total volume of 25 µL elution buffer. To facilitate higher yields, the elution buffer was prewarmed to 60 °C, resulting in concentrations ∼1 µg/µL.

Starting a few days before electroporation, DT40 cells were split daily to be kept at logarithmic growth. Prior to electroporation, 3×10^6 cells were collected by centrifugation and resuspended in 100 µL transfection reagent T and mixed with 12 µL linearized DNA (∼12 µg). The suspension was transferred to an Amaxa electroporation cuvette and electroporated using the program B-23. Directly after, cells were resuspended in 4 mL fresh medium without antibiotics or doxycycline.

3 days after electroporation, cells that stably integrated the biosensor were selected by addition of 2 mg/mL G418. After ≥ 1 week of selection, cryostocks were made and the cells were cultured in the presence of doxycycline to deplete endogenous wtCENP-T.

2.2.4.3 Growth analysis of stable DT40 cell lines

The potential of chicken CENP-T biosensors to rescue the lethal phenotype of CENP-T knockout was assessed by comparing growth rates of rescued cells with those of CENP-$T^{Tet\text{-}off}$ cells growing in the presence or absence of doxycycline. To avoid growth inhibition due to dense cell numbers and nutrient shortage, cells were cultivated in medium with only 1 % FBS but normal levels of chicken serum.

Prior to the experiment, cells were grown for 1 week at low densities ($\leq 2\times10^6$ cells/mL) without doxycycline and G418. At day 0, cells were diluted to 1×10^5 cells/mL and doxycycline was added to all flasks but the control. For initial analysis, cells were counted 24, 48, 72, an 96 h after starting the treatment; cell lines that differed only by the linker peptide from previously established cell lines were counted after 48 and 96 h only. Counting was performed using the Scepter™ cell counter (EMD Millipore) with 60 µm sensors tips and a particle gating of 7.6–18 µm. To maintain constant growth conditions, cells were split daily (after counting) at a 1:2 ratio. Non-rescued CENP-T$^{\text{Tet-off}}$ cells treated with doxycycline were not diluted during the course of the experiment, as they stopped proliferation within the first 24 h after addition of doxycycline.

2.2.4.4 Nocodazole treatment

To generate a situation in which kinetochores (KTs) do not experience force, cells were treated with 5 µM nocodazole for 1.5–2 h. Nocodazole was dissolved as a 25 mM stock solution in DMSO and stored in aliquots at -20 °C. Control cells were treated for the same period with equivalent amounts of DMSO alone, namely 1:5 000.

2.2.5 Talin$^{-/-}$ and Vinculin$^{fl/fl}$ cell culture and cell line generation

Talin-1 and Talin-2 deficient mouse fibroblasts (named Talin$^{-/-}$ in this thesis) were generated by Roy Zent and Moritz Widmaier [Theodosiou et al., 2015]. Mouse embryonic fibroblasts with floxed vinculin (Vinculin$^{fl/fl}$) were provided by Ingo Thievessen and Clare Waterman (NIH) and subsequently immortalized and cloned by Carleen Kluger (MPI of Biochemistry). Both cell lines were grown at 37 °C and 5 % CO_2 in a humidified incubator.

2.2.5.1 Passaging, freezing, and thawing

Passaging

Talin$^{-/-}$ and Vinculin$^{fl/fl}$ cells were cultured similar to HeLa cells; however, using a different growth medium (see sec. 2.2.2). As both cell lines grew significantly faster, cells were typically split every 2–3 days by 1:8–1:16.

Thawing and freezing

Thawing and freezing was done as described for HeLa cells; however, with a different growth medium (sec.2.2.2).

2.2.5.2 Transient transfection of Vinculin$^{fl/fl}$ cells

Candidates for new TSMs were first tested by transient cytosolic expression in Vinculin$^{fl/fl}$ cells. Cells were seeded on 6-well plates and transfected at ∼80 % confluency. Per well, 5 µL

Lipofectamine 2000 and 2 µg plasmid DNA were diluted in 150 µL Opti-MEM each. Both components were then mixed and incubated according to the manufacturer's protocol. The transfection mix was removed from the cells after 8 h and cells were analyzed 24–72 h post transfection.

2.2.5.3 Generation of stable cell lines from Talin$^{-/-}$ cells

Talin$^{-/-}$ cells were rescued by stable expression of talin-biosensors. Biosensor cDNA was integrated into the genome using the Phoenix helper-free retrovirus producer cell system (Nolan Lab, Stanford). The Phoenix system is analogous to the Gryphon system described in sec. 2.2.3.3, with the difference that Phoenix cells produce ecotropic viruses that cannot infect human cells and are therefore classified as S1.

Cell lines were generated using the same transfection and infection protocol as described in 2.2.3.3. Rescued cells were isolated from non-rescued cells by taking advantage of their increased ability to adhere to cell culture dishes. To this end, cells were washed and a treated with trypsin that was diluted 10× higher than for normal passaging. As talin deficient cells are unable to spread and adhere only very weakly, non-rescued cells could be washed off after a few minutes of trypsin treatment, while rescued cells still stably adhered.

2.3 Immunocytochemistry and general microscopy

2.3.1 Antibodies

Table 2.16: Antibodies for immunofluorescence

Target	Label	Origin	Company	Catalog#	Conc.
Tubulin (DM1α)	–	mouse	Sigma-Aldrich	T6199	1:500
Mad1	–	rabbit	GeneTex	GTX105079	1:500
Mouse IgG (H+L)	Alexa-647	donkey	Invitrogen	A31571	1:500
Rabbit IgG (H+L)	Alexa-405	goat	Invitrogen	A31556	1:500

2.3.2 HeLa fluorescence microscopy

Coverlips and life cell imaging dishes were coated for ≥ 2 h with fibronectin (0.5 µg/mL PBS; Merck, Cat.# 341631) and placed under an UV lamp for ≥ 30 min for sterilization. Directly before seeding, fibronectin was removed and dishes were once rinsed with PBS. Cells were allowed to adhere for at least 2 h, but usually o/n.

For life cell imaging, growth medium was removed and, after washing 2× with PBS, replaced by imaging medium (with HEPES, without phenole red).

For immunostainings, cells were washed 1× with PBS and 1× with PHEM buffer (tbl. 2.17). Next, cells were fixed and permeabilized for 20 min at RT with 2 % PFA + 0.5 % Triton X-100 in PHEM. After fixation, cells were washed 3× with PHEM and blocked with 2 % BSA + 0.1 % Triton X-100 in PHEM for 1 h at RT. Primary and secondary antibodies were diluted in blocking buffer and incubated each for 1 h at RT, separated by 3× washing with PHEM in between. After incubation of the secondary antibody, cells were washed once, followed by incubation with DAPI (1:10 000 in PHEM) for 5 min at RT, and washed 3× with PHEM. Coverslips were then mounted with ProLong Gold (Life technologies, Cat.# P36934) mounting medium and stored at 4 °C until imaging.

Table 2.17: PHEM buffer

Component	Weight used	final conc.
PIPES	30.24 g	100 mM
HEPES	2.38 g	10 mM
EGTA	3.80 g	10 mM
$MgCl_2$	0.324 g	2 mM
ddH_2O (to pH 7.4)		*ad* 1 L

2.3.3 DT40 fluorescence microscopy

Life cell microscopy and immunocytochemistry of DT40 cells was performed on life cell imaging dishes, coated with Concanavalin A (ConA) (Sigma, Cat.# L7647), dissolved at 1 mg/mL in ddH_2O. 2 µL per 1 cm^2 surface area were spread and allowed to dry. Directly prior to seeding, dishes were once washed with PBS. 0.5–0.75 mL cells were seeded per 1 cm^2 and allowed to adhere to the coated glass for 10 min at RT. Remaining medium was then removed and cells were covered either with medium (containing inhibitors, if applicable), or washed with PBS for further treatment.

For immunocytochemistry, seeded cells were washed 3× with PBS and fixed in 3 % PFA for 15 min (RT). After washing, cells were permeabilized with 0.5 % NP40 (Tergitol) for 10 min (RT) and blocked with 1 % BSA in PBS for either 1 h at RT or o/n at 4 °C. Primary antibodies were diluted in blocking buffer and incubated for 2 h at RT. After 3× washing with PBS, secondary antibodies (also diluted in blocking buffer) were incubated for 1 h at RT. After washing once, cells were stained with DAPI (1:10 000 in PBS) for 10 min at RT and washed 3× with PBS. Cells were imaged directly after staining and inside the life cell imaging dish, filled with PBS.

Immunostainings were imaged at a Leica SP5 confocal microscope, using HyD detectors and an HCX PL APO lambda blue 63.0×1.20 WATER UV objective. To represent the full 3D structure of the mitotic spindle, immunostainings were imaged as Z-stacks (pinhole 100 µm) in steps of 450-500 µm. To avoid photobleaching of the tension sensor, Alexa-647 labeled tubulin was used for focusing. The actual stack were recorded sequentially by color in the order YPet (tension sensor), Alexa-647 (tubulin) and DAPI (DNA). Images shown in the thesis are Z-projections (generated with Fiji, projection mode: standard deviation).

2.4 Ratiometric FRET analysis of CENP-T biosensors

2.4.1 Image acquisition and microscope settings

For life cell ratiometric FRET analysis, biosensor expressing DT40 cells were seeded on ConA coated glass-bottom #1.5 life cell imaging dishes as described in sec. 2.3.3. After cells adhered to the imaging dish, the medium was replaced with imaging medium (HEPES buffered, without phenole red), supplemented either with 5 µM nocodazole dissolved in DMSO and administered in a 1:5 000 dilution, or with DMSO alone. Cells were imaged 1.5–2 h after starting the treatment.

Leica TCS SP5 X and Leica TCS SP8 confocal microscopes, equipped with highly sensitive HyD detectors, were used for ratiometric FRET analysis. Specific settings for both systems are listed in tbl. 2.18.

To avoid photobleaching and -damage, the laser power during focusing was 10× lower than for actual image acquisition. Furthermore, screening for mitotic cells was done at lower magnification to reduce the energy density. Once a cell was focused onto a plane with a high number of kinetochores, laser power and magnification were increased and the donor and acceptor/FRET emission signal was recorded simultaneously upon excitation.

Table 2.18: Microscope settings for ratiometric FRET measurements

Parameter	Leica TCS SP5 X	Leica TCS SP8
Excitation wavelength	514 nm	514 nm
Objective	63×, water [a]	63×, water [b]
Pinhole	100 µm	100 µm
Zoom	6.5×	6×
Image dimensions	37.9 µm	30.75 µm
Pixel resolution	512×512	512×512
Scanning speed	400 Hz	400 Hz
Voxel width	74.1 nm	60 nm
Line average	2×	2×
Donor gating	525–550 nm	525–550 nm
Acceptor gating	600–700 nm	580–700 nm
Donor gain	100 %	100 %
Acceptor gain	100 %	100 %
Temperature	RT	37 °C

[a] HCX PL APO lambda blue 63.0×1.20 Water UV, refractive index 1.33

[b] HC PL APO CS 63×/1.20 Water, refractive index 1.33

2.4.2 Thresholding and data evaluation

Isolation of KTs and subsequent image analysis was performed with custom written Matlab software (developed by Christoph Klingner, MPI of Biochemistry). The workflow for KT thresholding is shown in fig. 2.1. For automated KT thresholding, a region of interest (ROI) was first drawn around the cell. Next, the donor image was blurred with a Gaussian lowpass filter (size 20, 1 sigma). Extended maxima of the blurred images were identified and dilated to generate kinetochore masks. As this thresholding procedure occasionally picked up regions with heterogeneous but weak background signal, a quality check was performed to ensure that the average acceptor intensity of each identified KT mask was at least 3 times brighter than the average background intensity. In addition, masks containing saturated pixels were excluded. KT masks were then superimposed on the original (not blurred) donor and acceptor images and the FRET ratio was calculated for each KT as mean acceptor intensity divided by mean donor intensity. For further analysis, the FRET ratio of an entire cell (shown as one "dot" in boxplots) was defined as the median KT FRET ratio of all individual KTs per cell. Boxes in boxplots indicate 25 and 75 % percentiles, the

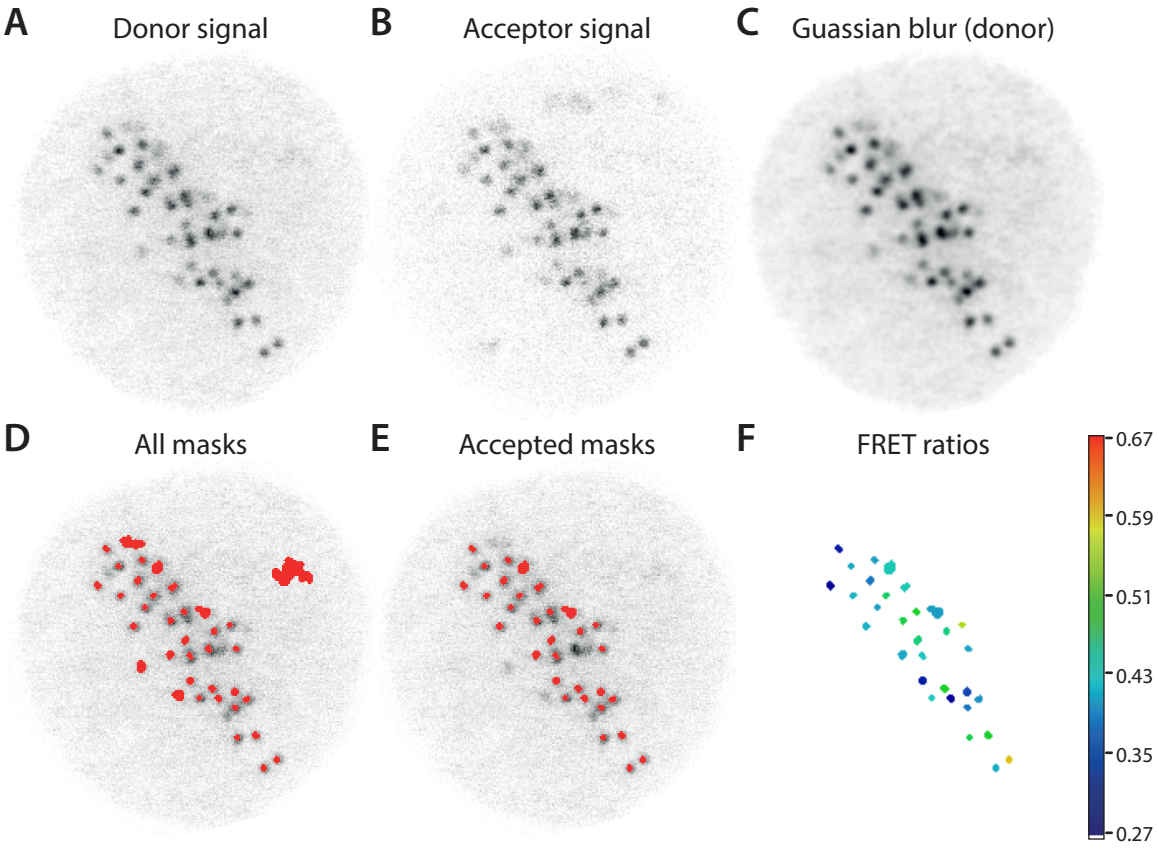

Figure 2.1: Kinetochore thresholding. **A**) Original donor image. **B**) Original acceptor image. **C**) Donor image filtered with a Gaussian lowpass filter. **D**) Initial masks were generated by identification of extended maxima and subsequent dilation of the blurred donor image. **E**) Masks with saturated pixels or a mean acceptor intensity $<3\times$ higher than the acceptor background were excluded. **F**) FRET ratios were calculated for each mask as mean acceptor intensity divided by mean donor intensity.

median is shown as line, the mean is indicated by a small square, and the maximum length of the whiskers is set to $1.5\times$ the width of the box.

2.5 TCSPC-FLIM

2.5.1 Image acquisition and microscope settings

Cytosolically expressed TSM candidates as well as talin biosensors were analyzed by live cell time-correlated single photon counting fluorescence lifetime imaging microscopy (TCSPC-FLIM). Experiments were performed on a Leica TCS SP5 X confocal laser scanning microscope, equipped with a pulsed white light laser (WLL, 80 MHz repetition rate; NKT Photonics), a FLIM X16 TCSPC detector (LaVision Biotech) and a $63\times$ water objective (HCX PL APO CS, NA=1.2). As only the donor lifetime is measured for FLIM-FRET applications, a bandpass filter 545/30 (Chroma) was used to block photons emitted by the

acceptor fluorophore. Images were acquired with a scanning velocity of 400 Hz, a spatial resolution of 512×512 pixels, and an image field coverage of 123.02×123.02 µm^2. To collect sufficient photons for lifetime fitting, a series of 20 images was recorded per cell and superimposed for lifetime analysis.

2.5.2 Thresholding and data evaluation

Data were analyzed with custom-written MATLAB software (developed by Anna-Lena Cost and Carleen Kluger, MPI of Biochemistry) as published in Austen et al. [2015] and Ringer et al. [2017a]. In brief, a ROI was manually drawn around each cell and subsequent thresholding was restricted to the area within the ROI. Signal of cytosolically expressed TSMs was isolated by a multi-Otsu thresholding with 2 intensity classes; the brighter class was used as cytosolic signal. For isolation of focal adhesions (FAs), the original image was blurred with a Gaussian lowpass filter (size 3, 2 sigma) and subjected to a 3-class multi-Otsu thresholding. To exclude areas of bright cytosolic background as occasionally found in the vicinity of the nucleus, only object sized between 0.5 and 150 µm^2 were accepted as FA masks.

Next, a histogram of the arrival times of all photons within the identified masks was generated and photon arrival times were fitted by a mono-exponential decay function. Fits with an $R^2 < 0.98$ were excluded from further analysis. For obtaining the donor only lifetimes, cells either expressing cytosolic YPet or talin-YPet(int) were measured. FRET efficiencies were then calculated as

$$E = 1 - \frac{\tau_{DA}}{\tau_D} \tag{2.1}$$

with τ_D being the median donor lifetime of all YPet control cells measured at the particular experimental day, and τ_{DA} the lifetime of a tension sensors expressing cell. Thus, the described procedure provides the average lifetime of all FAs (or from the complete cytosol) of one individual cell, and the FRET efficiencies of each individual tension sensor expressing cells are then calculated using the median donor only lifetime of the respective experimental day. Boxplots depict the FRET efficiency of each individual cell as blue dot, the median (red line) and the interquartile range (blue box). The maximum length of the whiskers is 1.5× the interquartile range.

2.6 Statistical analysis

2.6.1 Statistical tests on pooled data

CENP-T ratiometric FRET data

Caused by the systematic day-to-day shifts of absolute FRET ratios, pooled data containing all individual cells of one cell line and condition across several experimental days were not

in all cases normally distributed. Consequently, the non-parametric Mann-Whitney U test was used for statistical analysis of pooled ratiometric FRET data. Because its test statistics is determined solely by the ranks of the individual data points and not by their absolute values, this test is particularly robust for non-uniform data distributions.

FLIM data

FLIM data were analyzed using the non-parametric Kolmogorov-Smirnov test, so that normal distribution of the data was not required. Unlike the Mann-Whitney U test, however, this test still takes the distribution (which can be of any shape) into account, and therefore has a higher power to detect differences if the distributions of the two samples are similar in shape, but differ with respect to their mean or variance.

2.6.2 Bootstrap analysis

Bootstrapping is a statistical resampling method that was used for a more detailed analysis of ratiometric FRET data. Bootstrap analysis tests if an effect seen within an empirical data set is a generic property of the entire distribution, or rather dependent on a small subset of extreme values. To this end, random samples are drawn from the original distribution. In cases with moderate sample sizes of the original data, or if bootstrapping is performed to estimate standard errors and construct confidence intervals, random samples should have the same number of data points as the original sample. Consequently, the samples are drawn "with replacement", meaning that individual values can (and usually will) be represented more than once within the bootstrap sample.

After one random sample has been drawn from each of the two original data sets (here: metaphase cells and nocodazole treated cells), the two bootstrap samples are analyzed using the same statistical test as for the original data (in this study the Mann-Whitney U test). The whole process is then repeated multiples times (in this study 20 000 times) to obtain a distribution of test results for each pair of the original data set.

In biology, the result of a statistical analysis is typically reported by the p-value. The p-value itself, however, lacks information about which of the samples had the higher mean. However, if the difference between both sample means is rather small, this relation could be reversed in a subset of bootstrap samples. For this reason, Z-scores are reported in the context of bootstrap analysis as an alternative to p-values. Z-scores can be unambiguously translated to p-values, but have not yet lost the information about the directionality of the detected difference. A Z-score of -1.96 or 1.96 is equivalent to a p-value of 0.05.

The 20 000 Z-scores obtained from each pair of original data are shown as histograms. In cases where differences between original data sets are caused by a small number of extreme

values, histograms of bootstrap samples lack normal distribution. This is due to the fact that only a subset of bootstrap samples will contain these extreme values. Additionally, the Z-scores of the original data will not map onto the peaks of the Z-score histograms from the bootstrap samples.

2.6.3 Confidence intervals

In most biological experiments, only a small subset of the entire population is sampled. Thus, the arithmetic mean of the empirical data is only a point estimate for the real population mean. To indicate the level of uncertainty about the true mean, confidence intervals (CIs) are computed on the basis of the empirical data mean and standard deviation (SD). CIs indicate the range, in which the true population mean resided with a predefined and indicated certainty (typically 95 % for biological applications). The width of a CI critically depends on the population's SD, but similarly to the estimate for the population mean, the experimentally obtained SD σ is also just an estimation of the true SD of the entire population σ^*.

If a sampling population is large enough, it can be assumed that σ sufficiently approximates σ^*. In accordance with the central limit theorem, a 95 % CI is then defined by the boundary values, between which the area under the standard normal distribution covers 95 % of the total area under the curve. The lower and upper boundaries of a CI are thus defined as

$$\mathrm{CI}_{lower} = \overline{X} - Z_{\alpha/2} \times \frac{\sigma}{\sqrt{n}} \quad \text{and} \quad \mathrm{CI}_{upper} = \overline{X} + Z_{\alpha/2} \times \frac{\sigma}{\sqrt{n}} \tag{2.2}$$

where $\overline{X}$ is the point estimate of the sample mean, α the predefined level of confidence (e.g. 0.95 for a 95 % CI), and Z refers to the standard normal Z-table for the area under the curve. As $Z_{0.95/2} = 1.96$ and $\frac{\sigma}{\sqrt{n}}$ is the standard error of the mean (SEM), the 95 % confidence interval is given by $\overline{X} \pm 1.96 \times \mathrm{SEM}$.

If the sample size is not sufficiently large, however, it cannot be assumed that σ sufficiently approximates σ^*. This adds an additional level of uncertainty, and applying the Z-table and the SEM would result in CIs that are too narrow. To compensate for this additional uncertainty, CIs for smaller samples are calculated based on the Student's t distribution instead of using the standard normal distribution.

Rather than being a single distribution, the t distribution is a family of curves, whose exact shape depends on the respective degrees of freedom *df* (see fig. 2.2). Like the Z-table for the normal distribution, T-scores for different degrees of freedom and confidence levels have been tabulated. Upper and lower boundaries of CIs for small to medium sample sizes

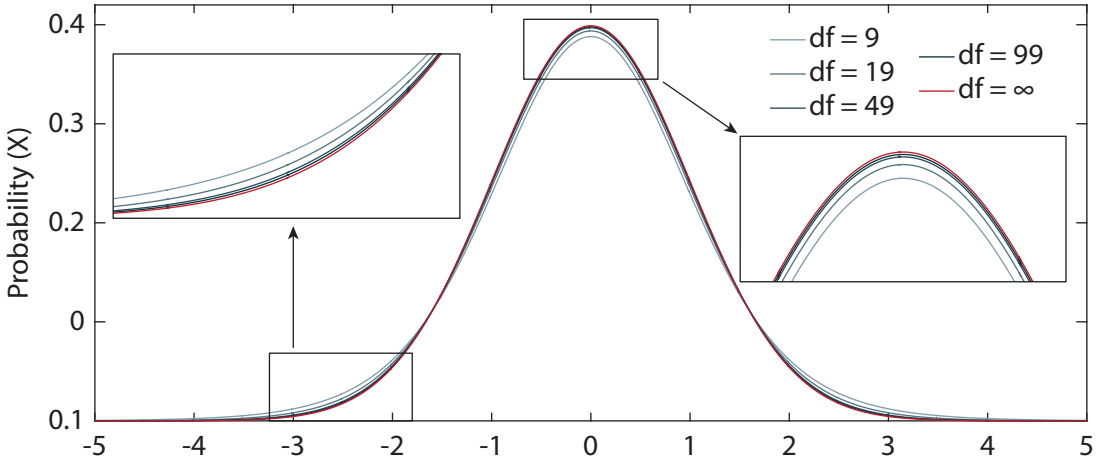

Figure 2.2: *T*-distribution. The T-distribution is a family of curves that is determined by the degrees of freedom df. The lower df, the flatter the curve; for increasing df, the T distribution approaches the standard normal curve (shown in red).

are are defined by

$$\mathrm{CI}_{lower} = \overline{X} - T^{df}_{\alpha/2} \times \frac{\sigma}{\sqrt{n}} \quad \text{and} \quad \mathrm{CI}_{upper} = \overline{X} + T^{df}_{\alpha/2} \times \frac{\sigma}{\sqrt{n}} \tag{2.3}$$

where df are the degrees of freedom (calculated as n − 1; n = number of measurements) and T the function value of the T-distribution corresponding to the respective degrees of freedom df and the predefined confidence level.

Table 2.19 exemplarily shows 95 % CIs for data sets that vary in size, but share the same point estimate $\overline{X}$ and experimentally defined σ; the confidence level is set to 0.95 % in all cases.

Table 2.19: Confidence intervals in relation to sample size

n	df	$\overline{X}$	σ	α	$T^{df}_{\alpha/2}$	$\frac{\sigma}{\sqrt{n}}$	95 % CI
10	9	10	2	0.95	2.262	0.632	[8.569; 11.431]
20	19	10	2	0.95	2.093	0.447	[9.064; 10.936]
50	49	10	2	0.95	2.010	0.283	[9.431; 10.569]
100	99	10	2	0.95	1.984	0.200	[9.603; 10.397]

2.6.4 Effect size calculation

For better comparison between different experiments and compensation of systematic shifts, raw FRET ratios (reported in arbitrary units) were transformed into effect sizes. The effect size is a standardized mean difference, also referred to as Cohen's d or Hedges' g. Similar to

a correlation coefficient, Cohen's d and Hedges' g are dimensionless numbers that quantify the effect of a certain treatment in comparison to a control group; in this thesis, the effect of nocodazole treatment in comparison to untreated metaphase cells. Thus, transforming raw data to effect sizes reduces the number of "data sets" shown in the graphs by the factor of two (if assumed that on the level of the original data, treatment group and control were shown as two individual data sets). Cohen's d and Hedges' g were calculated as

$$d = \frac{\overline{X}_{noco} - \overline{X}_{meta}}{S_{within}} \tag{2.4}$$

where $\overline{X}$ is the sample mean of the respective group. S_{within} is the within standard deviation pooled across groups and it is defined as

$$S_{within} = \sqrt{\frac{(n_{noco}-1)S^2_{noco} + (n_{meta}-1)S^2_{meta}}{n_{noco}+n_{meta}-2}} \tag{2.5}$$

with S being the individual standard deviation of each group. As the presented formula has a slight bias towards overestimating d in small samples, an additional correction factor J was introduced. J is commonly approximated by

$$J = 1 - \frac{3}{4 \times (n_{noco}+n_{meta}-2) - 1} \tag{2.6}$$

and the unbiased effect called Hedges' g is calculated as

$$g = d \times J. \tag{2.7}$$

Finally, the variance of Cohen's d is given by

$$V_d = \frac{n_{noco}+n_{meta}}{n_{noco} \times n_{meta}} + \frac{d^2}{2(n_{noco}+n_{meta})} \tag{2.8}$$

and the variance of Hedges' g by

$$V_g = V_d \times J^2 \tag{2.9}$$

[Borenstein et al., 2009].

2.6.5 Meta analysis

Once all data have been transformed to the effect scale, the common effect across all studies can be determined by meta analysis [Borenstein et al., 2010, 2009, 2007]. The weight of an individual study within the complete analysis depends on the quality of the original study.

Studies with large sample sizes and a narrow data distribution will have higher weight on the combined result than studies with small sample sizes and large standard errors.

Generally, two different models for the conduction of a meta-analysis can be distinguished, namely a fixed- and a random-effects model [Borenstein et al., 2007]. As the concept of meta analysis is rarely known in the field of experimental biology, a more detailed description of both models and why I decided to apply the random-effects model in the course of this study can be found directly within the results section (3.10.3.2). This should help the reader to more easily follow the line of thoughts while reading the results part, without the need to jump back and forth between different chapters.

Within the random-effects model, the total weight of a particular study is determined by the sum of the within-study variance v_i and the between-study variance T^2.

After the individual effect sizes g and variances v of each study i were calculated according to equations (2.7) and (2.9), the total variance Q is calculated as

$$Q = \sum_{i=1}^{k} w_i (g_i - \overline{g})^2 \tag{2.10}$$

with k being the total number of studies i and w being the weight of an individual study calculated as

$$w = \frac{1}{v}. \tag{2.11}$$

This allows to compute the between-study variance T^2 as

$$T^2 = \begin{cases} \frac{Q-df}{C} & \text{if} \quad Q > df \\ 0 & \text{if} \quad Q \leq df \end{cases} \tag{2.12}$$

with C defined as

$$C = \sum_{i=1}^{k} w_i - \frac{\sum_{i=1}^{k} w_i^2}{\sum_{i=1}^{k} w_i} \tag{2.13}$$

and df referring to the degrees of freedom given by

$$df = k - 1. \tag{2.14}$$

Now, the combined variance v^* of each study can be calculated as

$$v^* = v + T^2 \tag{2.15}$$

and the final wight w^* is given by

$$w^* = \frac{1}{v^*}. \tag{2.16}$$

The combined effect (or weighted mean) $\overline{g^*}$ is then computed as

$$\overline{g^*} = \frac{\sum_{i=1}^{k} w_i^* g_i}{\sum_{i=1}^{k} w_i^*}. \tag{2.17}$$

The variance of the combined effect is defined as

$$v^* = \frac{1}{\sum_{i=1}^{k} w_i^*} \tag{2.18}$$

and the Z^*-score of the combined effect can be computed as

$$Z^* = \frac{\overline{g^*}}{\sqrt{v^*}} \tag{2.19}$$

(all computations referenced in Borenstein et al. [2007]).

2.7 Calibration of new tension sensor modules

Single-molecule force spectroscopy calibration of the new FL TSM was performed in collaboration with the lab of Matthias Rief (Technical University Munich). A detailed description of the experimental procedure and data evaluation is published in Ringer et al. [2017b] and Austen et al. [2015].

In brief, the TSM flanked by N- and C-terminal cysteine residues was transiently transfected into HEK293 cells by $CaPO_4$-precipitation and purified with a His-tag. Cysteine residues of the purified TSM were then used to attach functionalized DNA handles to either side. Via the DNA handles, individual molecules could be coupled to glass beads that were trapped in dual-trap optical tweezers, and force—extension curves were recorded for repeated stretch/relax cycles. As the DNA handles themselves show an elongation that can be fitted with a worm-like chain (WLC) model; elongation traces for completely closed or completely open TSMs can be fitted separately. While forces are low, experimental data initially follow the WLC fit for the folded module. When the applied force increases above the threshold of the TSM, the recorded trace will transit to the WLC fit of the open module. The force upon which this transition is observed indicates the force required for linker unfolding.

3 Results

3.1 Rational design of tension sensor experiments

Before setting up a tension sensor (TS) study, a number of pre-experimental evaluations are required. Besides identification of a suitable target protein, the two most important questions relate to the expected force regime and the technical setup that will be used for quantitative FRET measurements.

3.1.1 Expected force range

By the time this project was initiated, no *in vivo* measurements of molecular forces at kinetochore (KT) proteins had been published. However, two *in vitro* studies had given indicators for the expected force range: Powers et al. [2009] had shown that the Ndc80 complex forms attachments to dynamic microtubule (MT) tips that can bear loads of at least 2.5 pico Newton (pN), and Akiyoshi et al. [2010] demonstrated that the interaction between isolated budding yeast KT complexes and MTs is stabilized by mechanical forces; furthermore, a catch-bond behavior between 1 and 5 pN was observed. Based on these *in vitro* data, a KT–TS was based upon the 1–6 pN F40 module (see also sec. 1.3.4 and fig. 1.11).

3.1.2 Fluorophore optimization

The F40 sensor module was originally developed with an mTFP1–Venus FRET pair and predominantly analyzed by intensity-based methods [Grashoff et al., 2010]. Meanwhile, fluorescence-lifetime imaging microscopy (FLIM) was established in the lab as method of choice for quantitative FRET measurements and the fluorophores were changed to YPet and mCherry, which make a good FRET pair for FLIM applications due to the long YPet lifetime. Unfortunately, initial tests clearly demonstrated that our FLIM setup is not applicable for KT imaging, since KTs were too motile and bleached too fast to acquire the series of 20 images (taking 50 sec in total) necessary for our FLIM-FRET setup (data not shown). As faster alternative, protocols for ratiometric FRET of mitotic cells were established (see sec. 3.4). mCherry, however, shows (like other red fluorescent proteins) from comparatively

fast bleaching and low quantum yield. With the aim to improve signal intensities of ratiometric FRET images, tension sensor modules (TSMs) with alternative fluorophore pairs were tested.

The popular FRET pair mCerulean3–YPet yielded comparably bright KT signal in both channels, but vesicles showing equally bright autofluorescence in the donor channel impeded automatic KT thresholding (see sec. 3.4.2) during image analysis.

As second alternative, the newly developed red fluorescent protein mRuby2 [Lam et al., 2012] was tested in combination with YPet. While mRuby2 was reported to be superior to mCherry in terms of improved quantum yield (∼1.7× higher), elevated brightness (∼2.7×), faster maturation (∼3.8×), less bleaching (∼1.3× slower) and increased spectral overlap with YPet fluorescence, YPet–mRuby2 sensor modules showed reduced FRET as compared to the established YPet–mCherry pair – an effect that was also observed by other labs (personal communication) and is presumably caused by inefficient folding of mRuby2 when incorporated into a protein.

Together, these observations supported the decision to retain the established combination of YPet and mCherry also for ratiometric FRET.

3.2 Development of putative Ndc80 complex tension sensors

3.2.1 Generation of three putative Ndc80 biosensor constructs

A range of criteria have to be fulfilled in order to generate a functional TS (see sec. 1.4 for details). First, the target protein needs do be involved in force transduction, and second, the TSM has to be inserted into a region that experiences stretching force as consequence of two interaction partners that bind N- and C-terminally of the insertion site. Third, the targeted protein must remain functional after integration of the sensor module, and fourth, the quarternary protein structure must not impede elongation of the TSM when forces are applied.

The Ndc80 complex is the major MT interaction site (see sec. 1.2.3) and almost certainly fulfills the first requirement of being involved in force transduction; furthermore, it can be expected that forces are transduced along the rod in a linear fashion. Finally, it is – based on the current knowledge about the quarternary protein structure of the KT – rather unlikely that other KT components bind to the Ndc80 complex such that elongation is restrained. However, the stiff structure of the compact rod domain, which is predominantly made of coiled-coils, requires careful selection of potential insertion sites, as integration of the TSM within one of the protein tails is likely to either prevent correct formation of the tetramer, or forces the sensor module into folded conformation, looping out of the rod.

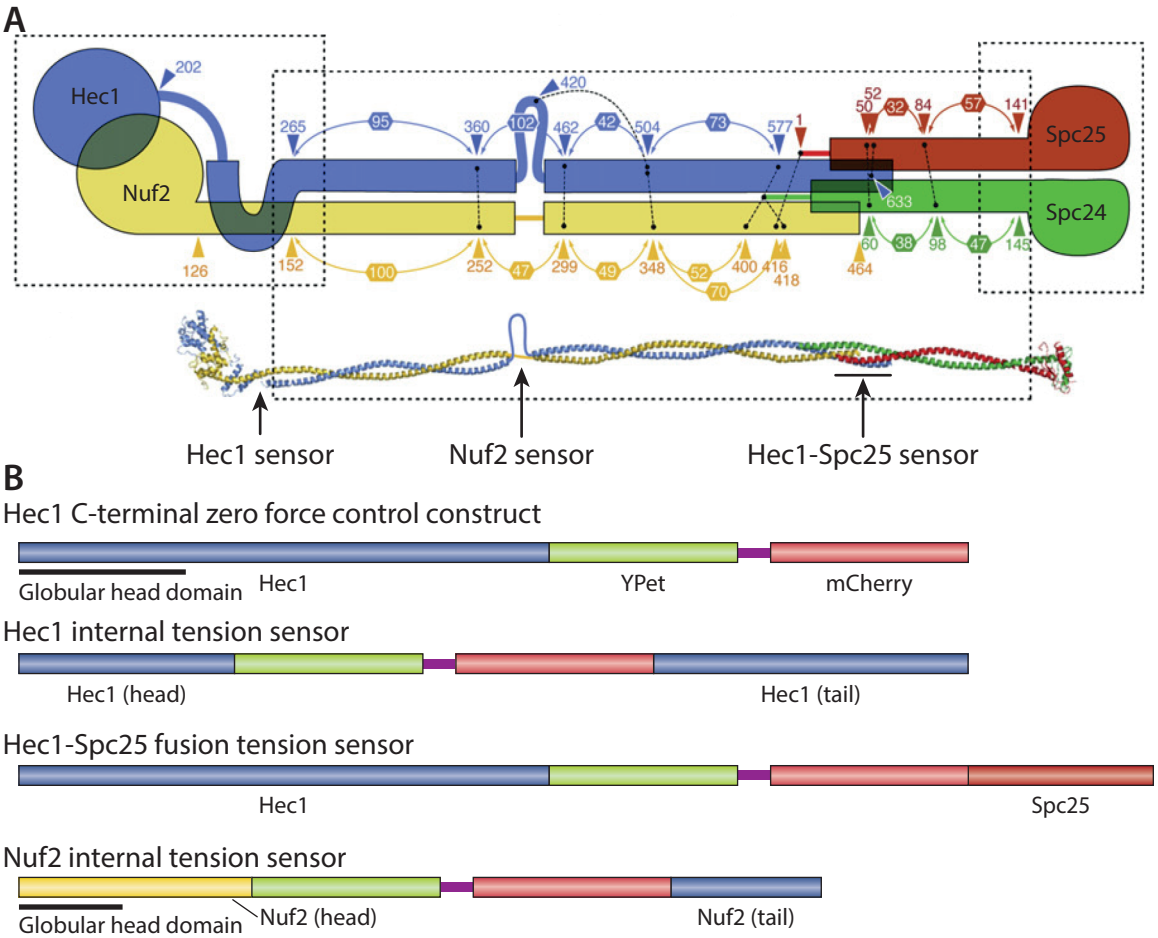

Figure 3.1: Ndc80 complex tension sensors. A) Predicted structure of the Ndc80 complex. Numbers with arrows are counters for amino acids. Black arrows mark TSM insertion sites. **B)** Hec1 C-terminal zero-force control and the three putative Ndc80 biosensors, drawn to scale on DNA level. The tetrameric coiled-coil is most likely disrupted in the Hec1-Spc25 fusion sensor. Panel A) is reproduced with permission from Ciferri et al. [2008].

Since it is impossible to predict whether a given integration site will make a functional biosensor, three putative Ndc80 biosensors have been generated by integrating the TSM at distinct positions within the Ndc80 complex (fig. 3.1).

The Hec1–TS was made by inserting the TSM between the MT binding calponin homology (CH)-domain and the beginning of the tail domain after aa 261 [Ciferri et al., 2008]. Such an integration is likely to still allow normal dimer formation with Nuf2 via coiled-coil interactions, but due to the increased length of Hec1 after TSM insertion, the Nuf2 head might be significantly separated from the MT surface. Structural studies, however, suggest that also in the native protein complex, only the head of Hec1 but not that of Nuf2 directly interacts with MTs [Alushin et al., 2010, Wilson-Kubalek et al., 2008]. Furthermore,

extinguishing the MT-binding capability of Nuf2 by introduction of a charge reversal point mutation had only relatively mild effects on KT–MT attachment [Sundin et al., 2011]. It can therefore be speculated that separating the head domains of Hec1 and Nuf2 does not interfere with MT-binding of the complex at whole.

The Nuf2 sensor takes advantage of the kink-region of Hec1 by positioning the sensor module opposite to the Hec1 loop into the Nuf2 tail after aa 282. As no structural information was available for this region of the protein complex, the appropriate location was deduced on the base of protein crosslinking-mass spectrometry (MS) [Ciferri et al., 2008] and structural prediction [Källberg et al., 2012].

The third construct is a Hec1–TS–Spc25 chimera. The direct fusion of both proteins by the TS was possible because the N-termini of both proteins point towards the inner KT, so that under normal conditions, the Hec1 C-terminus interacts with Spc25's N-terminus. Such a chimeric protein most certainly prevents formation of the tetrameric coiled-coil in the middle of the Ndc80 complex, but interactions between the tails of Hec1 and Nuf2 on the one hand and those of the two Spc proteins on the other hand might still be able to form, while the covalent fusion of Ndc80 and Spc25 by the TSM holds the entire complex together.

As zero-force control that is applicable for all three internal biosensors was generated by C-terminal tagging of Hec1.

3.2.2 Ndc80 tension sensor localization and functionality

To test if Ndc80 TSs localize to KTs (an obvious prerequisite for biological functionality), all three biosensors and the zero-force construct were transiently expressed in HeLa cells. The decision for HeLa as model organism was based on the wide use of this cell line in cell cycle research and the good availability of antibodies and published siRNA sequences. Fluorescence imaging of the TS in combination with tubulin immunostaining demonstrated that all constructs efficiently localize to KTs and that formation of the mitotic spindle is apparently undisturbed (fig. 3.2). Additionally, immunostainings against the spindle assembly checkpoint activator Mad1 showed that protein localization to KTs could be seen in prometaphase but gets lost during metaphase, indicating that the spindle assembly checkpoint is satisfied (fig. 3.3).

While correct localization of the biosensor and the loss of Mad1 signal from KTs during metaphase were promising indicators for functionality, only very few cells expressing internal TSs completed mitosis during time-lapse microscopy. Instead, a number of cells was observed that had presumably inconspicuous metaphase plates at the beginning, but failed to proceed to anaphase and finally lost chromosome bi-orientation (fig. 3.4).

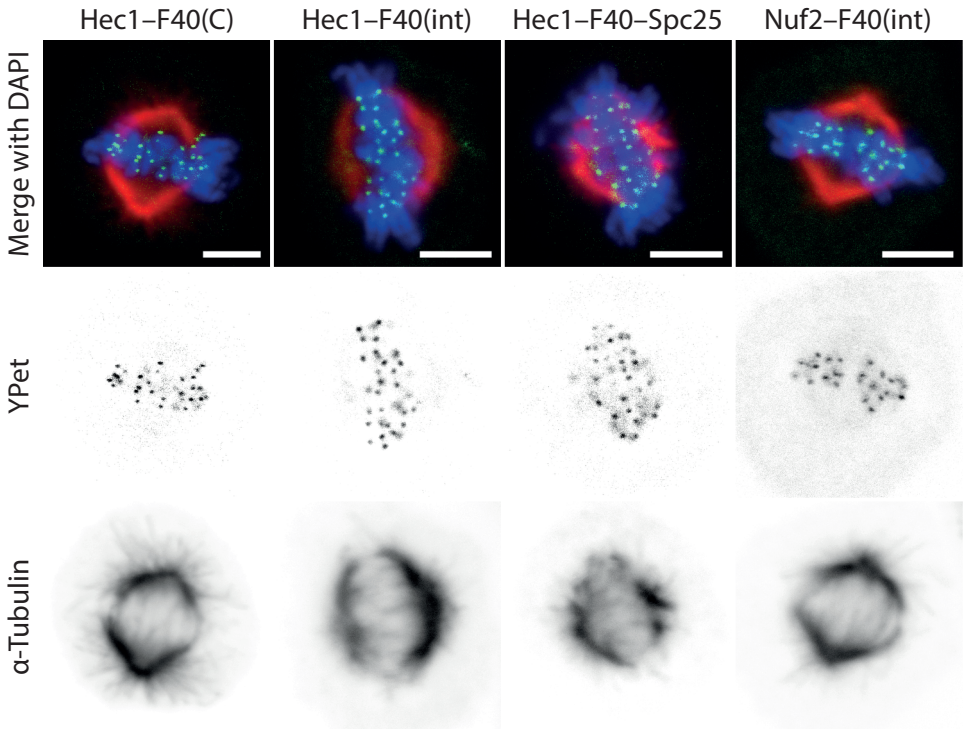

Figure 3.2: Normal spindle formation in Ndc80 biosensor expressing cells. HeLa cells transiently expressed the indicated biosensors. Fixed cells were stained for α-tubulin (red) and DAPI (blue); YPet was imaged to visualize KTs (green). Scalebar 5 µm.

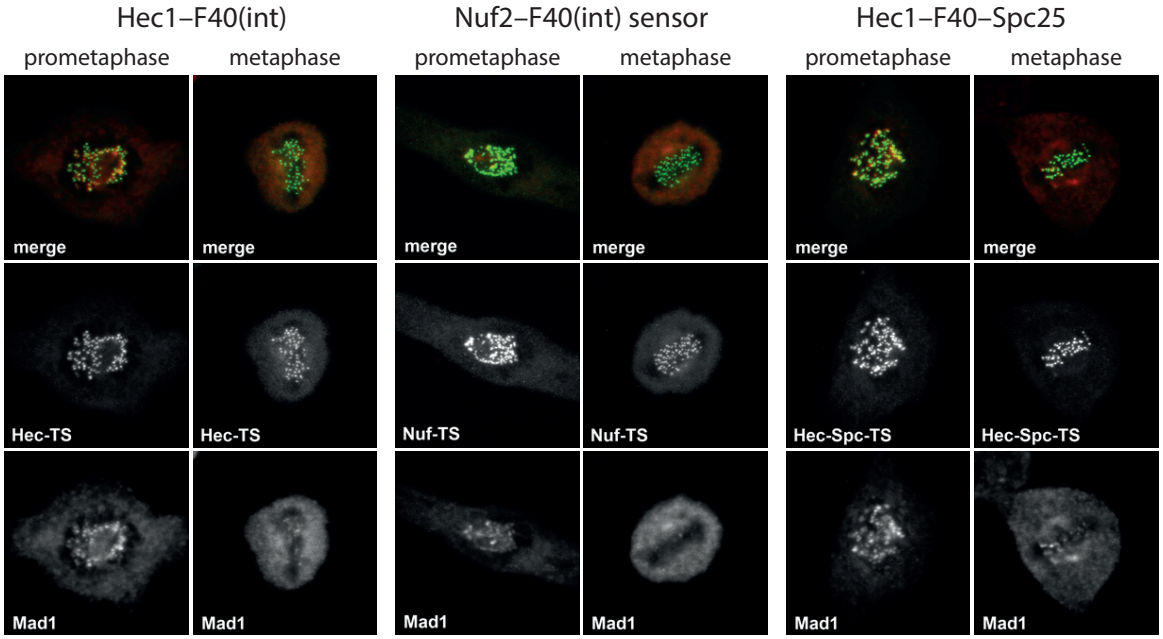

Figure 3.3: Ndc80 biosensor cells loose Mad1 localization during metaphase. Transiently transfected HeLa cells were fixed and stained for the spindle assembly checkpoint marker Mad1 (red); YPet (green) was imaged to visualize KTs. While Mad1 is localized to KTs during prometaphase, the localization gets lost as cells proceed through metaphase. (Images taken by Carsten Grashoff.)

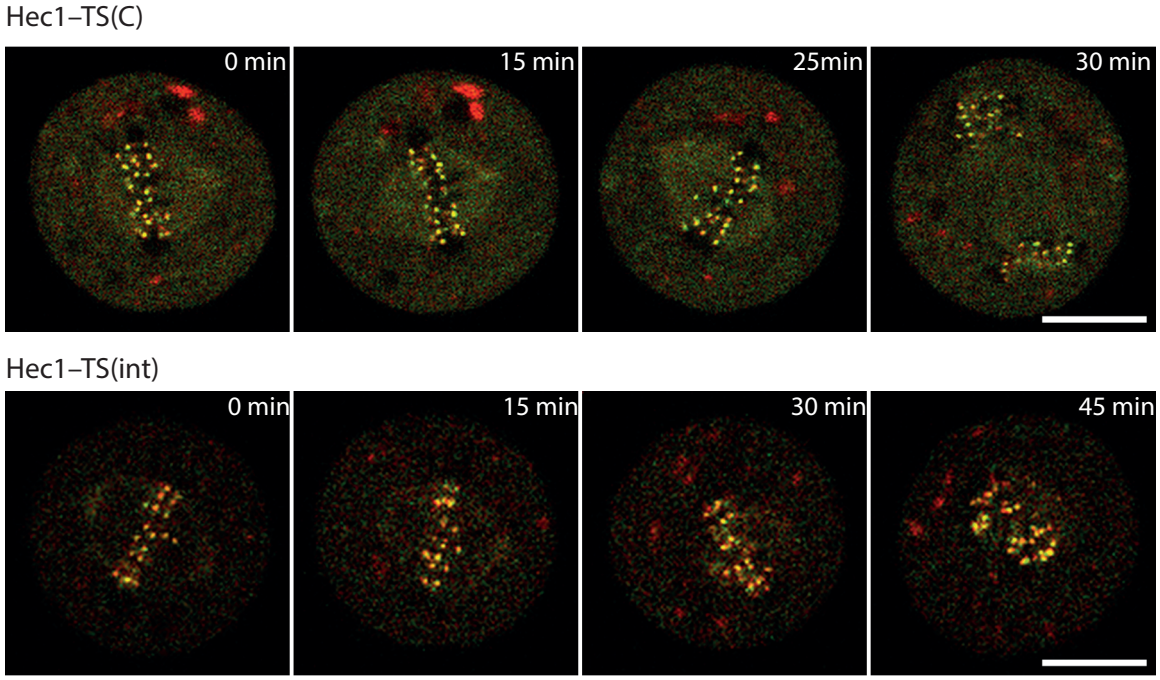

Figure 3.4: Time-lapse microscopy of mitotic Hec1 biosensor cells. While most Hec1 control construct expressing cells reliably completed mitosis during time-laps microscopy, a number of cells expressing the internal tension sensor failed to proceed to anaphase and eventually lost proper organization of the spindle (not quantified). Scalebars 10 µm.

In order to test whether expression of Ndc80 biosensors indeed interfered with progression through mitosis, a retroviral transfection system was used to generate stable cell lines with the aim to more closely study cell cycle progression in these cells. While it was no problem to establish a cell line that expresses fluorescently tagged histone H2B with the same system, several attempts to generate cell lines that express one of the biosensors or control constructs failed; either because no cells survived subsequent selection with antibiotics, or because surviving cells showed no fluorescence. In combination with the observations made during time-lapse microscopy, this indicates that integration of the TSM into the Ndc80 complex disturbed normal function of the protein complex. I therefore assessed alternative target proteins for KT-TS generation.

3.3 Development of putative CENP-T tension sensors

The MT binding Ndc80 complex it anchored to centromeric chromatin via two proteins, namely centromere protein C (CENP-C) and centromere protein T (CENP-T) (sec. 1.2.4.2, fig. 1.7) [Nishino et al., 2013]. Both proteins are essential, but while the CENP-C linkage essentially requires the complete KMN-network (comprised of the Ndc80 complex together with the Knl1 and Mis12 complexes), CENP-T can also bind directly to the Ndc80 complex

and, therefore, is thought to form a more direct linkage. In addition, it was shown in HeLa cells that each CENP-T recruits a total of ∼2 Ndc80 complexes (one directly and one via Mis12), whereas only about 40 % of all CENP-C molecules recruit a KMN network [Suzuki et al., 2015a]. Consequently, at least 60 % of all CENP-C are not connected to the outer KT and therefore not under force, making CENP-T the more promising candidate for the generation of a valuable KT-TS.

3.3.1 Conditional CENP-T knockout cell line

The example of the three Ndc80 sensors demonstrated that correct localization of the biosensor does not necessarily correlate with protein functionality. Furthermore, expression of the biosensor on top of endogenous protein might lead to an underestimation of forces if both variants are incorporated into the same structure, as the endogenous protein without the TSM might be shorter than the biosensor with the potential consequence that endogenous proteins carry the major load. For these reasons as well as for the purpose of better interpretable data, tension sensor experiments should be best performed in the absence of wt protein.

CENP-T is (as many kinetochore components) an essential protein, making a classical knockout approach impossible. The lab of Tatsuo Fugakawa has overcome this difficulty by using a tetracycline (tet)-off system to establish a range of conditional knock out cell lines on the background of DT40 chicken lymphoma cells. If grown in the absence of tetracycline, the tet-off promoter is active, but expression is suppressed soon after addition of tetracycline or the closely related doxycycline (see figure 3.5 and Hori et al. [2008] for a detailed description).

3.3.2 KMN recruitment to the chicken CENP-T tail

The choice of the TSM insertion site is a crucial step for the development of a new biosensor and critically depends on interacting proteins and – if known – their exact binding sites. I was therefore interested whether the recently discovered recruitment of the KMN network to human CENP-T [Huis in 't Veld et al., 2016, Rago et al., 2015] is conserved in chicken DT40 cells. In HeLa, KMN recruitment was highly dependent on a serine residue at amino acid (aa) 201, and further supported by phosphorylation of a threonine at aa 195 [Huis in 't Veld et al., 2016, Rago et al., 2015]. BLAST analysis of human CENP-T against mouse and rat (chosen for their common role as mammalian model organisms) as well as three avian species (including chicken) revealed a high level of conservation, but also categorical differences between mammals and birds (fig. 3.6). Interestingly, however, human threonine-195 is replaced by a serine in the three avian species, and human serine-201 was replaced by a threonine in all other tested species. It has to be noted that

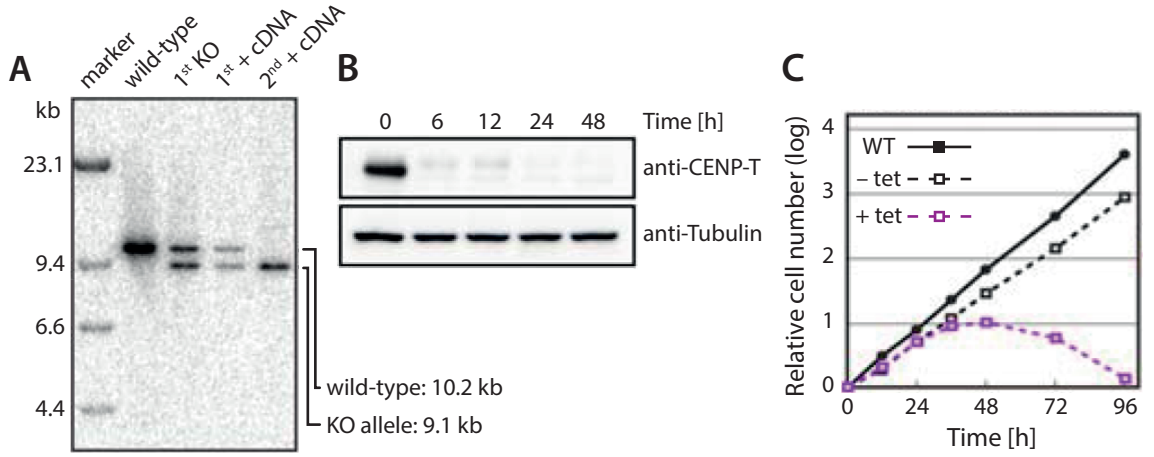

Figure 3.5: Characterization of the conditional DT40 CENP-T$^{\text{tet-off}}$ knockout cell line. **(A)** Southern blot showing a restriction analysis at different stages of CENP-T$^{\text{tet-off}}$ cell line generation. Lanes show, from left to right, a size standard, wt cells, heterozygous knockout, heterozygous knockout with CENP-T$^{\text{tet-off}}$ cDNA, and homozygous knockout with CENP-T$^{\text{tet-off}}$ cDNA. **(B)** Western blot analysis of CENP-T protein content in cell extracts treated with tetracycline for indicated time periods. **(C)** Growth curves of wt and CENP-T$^{\text{tet-off}}$ cells after addition of tetracycline. Images are reproduced with permission and modified from Hori et al. [2008].

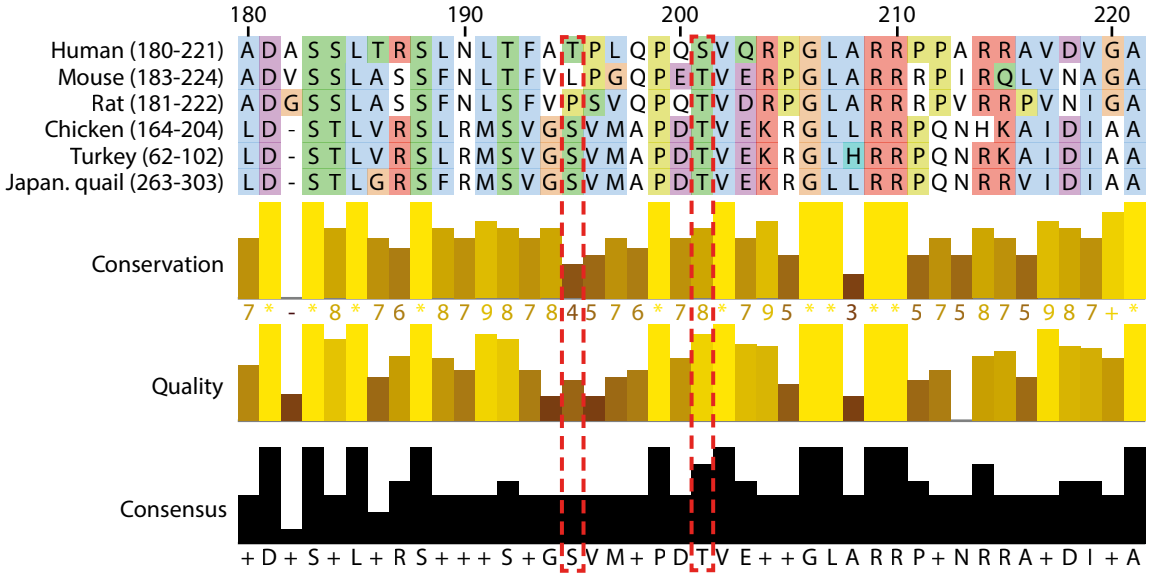

Figure 3.6: Evolutionary conservation of CENP-T CDK1 phosphorylation sites. In human CENP-T, serine-201 is flanked by a minimal CDK1 consensus motive S/T–X–X–R/K; phosphorylation of serine-201 facilitates KMN binding and is presumably enhanced by phosphorylation of threonine-195 [Huis in 't Veld et al., 2016, Rago et al., 2015]. BLAST analysis of three mammalian and three avian isoforms shows that despite the overall high level of conservation, serine is replaced by threonine and vice versa in the consensus sequence.

CDK1 is a serine/threonine kinase, rendering phosphorylation of the respective residues possible besides the Ser–Thr replacements. Considering, however, that phosphorylation at the S/T–X–X–R/K motive downstream of human serine-201 is rather weak [Suzuki et al., 2015b], it is questionable if also the corresponding threonine is phosphorylated in other species. These doubts are further underlined by a whole-proteome MS analysis of dependencies in DT40 KT assembly after depletion of defined components [Samejima et al., 2015]. In this study, the CENP-T cohort did not correlate with the Mis12 complex, and the authors propose competitive binding of CENP-T and the Mis12 complex to the Spc24/Spc25 binding site.

3.3.3 Generation of two CENP-T tension sensor constructs

CENP-T is functionally conserved between eukaryotes; however, the length and sequence of the unstructured tail varies between species. For identification of suitable insertion sites, a BLAST analysis between CENP-T protein sequences of various species was performed. Two particularly low conserved regions between the histone fold and the Spc24/Spc25 binding domain were identified as promising positions for TSM insertion, one located after amino acid 282, the other after amino acid 364. The zero-force control was generated by attaching the TSM to the N-terminus of the protein, since the C-terminus comprises the histone fold domain and is tightly incorporated into centromeric DNA (see figure 3.7).

3.3.4 CENP-T tension sensor constructs rescue knockout phenotype

Establishing KT tension sensors on the basis of an inducible knockout cell line brought the advantage that biological functionality of the biosensors could be tested in the absence of interfering wt protein. DT40 CENP-T$^{\text{tet-off}}$ cells were grown in the absence of doxycycline and electroporated with linearized CENP-T–TS DNA. Thereafter, cells that had the TS plasmid stably incorporated into their genome were enriched by selection with Geneticin (G418). After selection, the cell lines could be challenged by treatment with doxycycline, causing a depletion of wtCENP-T, while CENP-T–TS was still expressed. As CENP-T depletion is lethal, cells will die within a few days unless rescued by the expression of a functional CENP-T–TS construct (fig. 3.8 A).

Cells expressing either of the internal tension sensors or the N-terminal control construct survived knockdown of wtCENP-T and grew at rates comparable to CENP-T$^{\text{tet-off}}$ cells that were not treated with doxycycline, which is a direct evidence for biological functionality of the CENP-T biosensors (fig. 3.8 B). Furthermore, immunostainings of rescued cells showed morphologically normal spindles and sensor expressing cells at late anaphase indicate normal progression through mitosis (fig. 3.9).

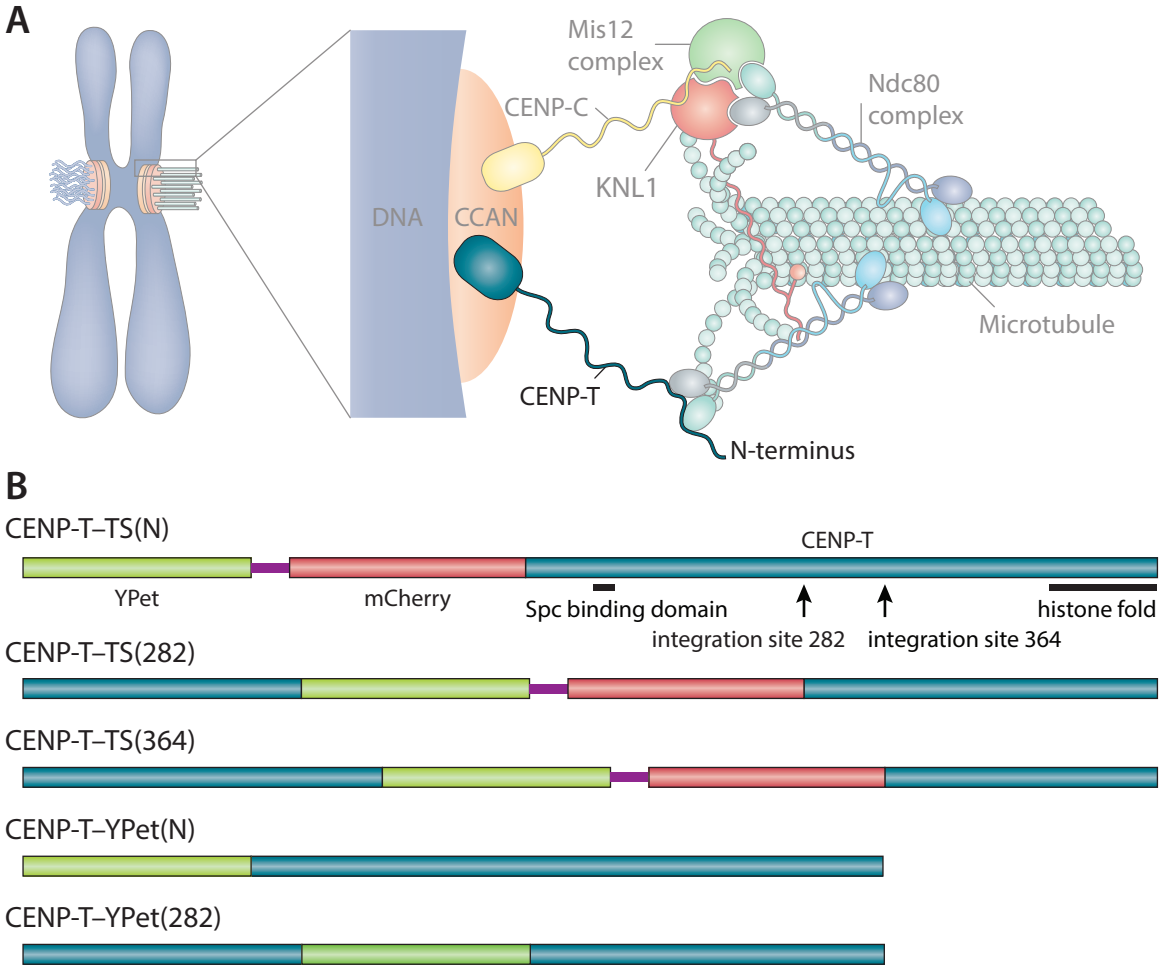

Figure 3.7: Construct design for CENP-T tension sensors. **(A)** The Ndc80 complex is connected to centromeric chromatin via CENP-T, but also via the Mis12 complex and CENP-C. **(B)** The C-terminus of CENP-T comprises a histone fold domain, which directly binds centromeric DNA. To avoid steric hindrance, the zero-force control construct was generated by N-terminal fusion of the TSM and CENP-T. For obtaining internal tension sensors, the module was inserted into the tail of CENP-T after amino acid 282 and 364, respectively. N-terminal and internal YPet-only constructs were generated as additional controls. All constructs are drawn to scale according to the number of amino acids.

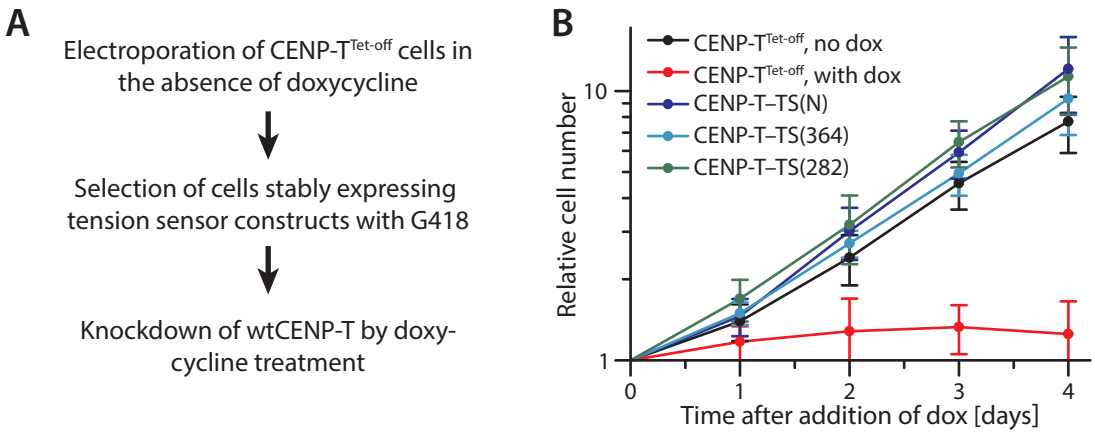

Figure 3.8: CENP-T tension sensor constructs rescue knockdown phenotype. A) CENP-$T^{tet\text{-}off}$ cells were grown in the absence of doxycycline and electroporated with CENP-T tension sensor constructs. After antibiotic selection for cells with the tension sensor DNA stably integrated into the genome, all cell lines were treated with doxycycline to asses functionality of the biosensors. **B)** Growth curves of wt and rescued cells; doxycycline was added at day 0. Both internal biosensors as well as the N-terminal construct rescue lethality of wtCENP-T depletion and restore normal growth rates. Plot depicts mean cell counts and standard deviation of three independent experiments.

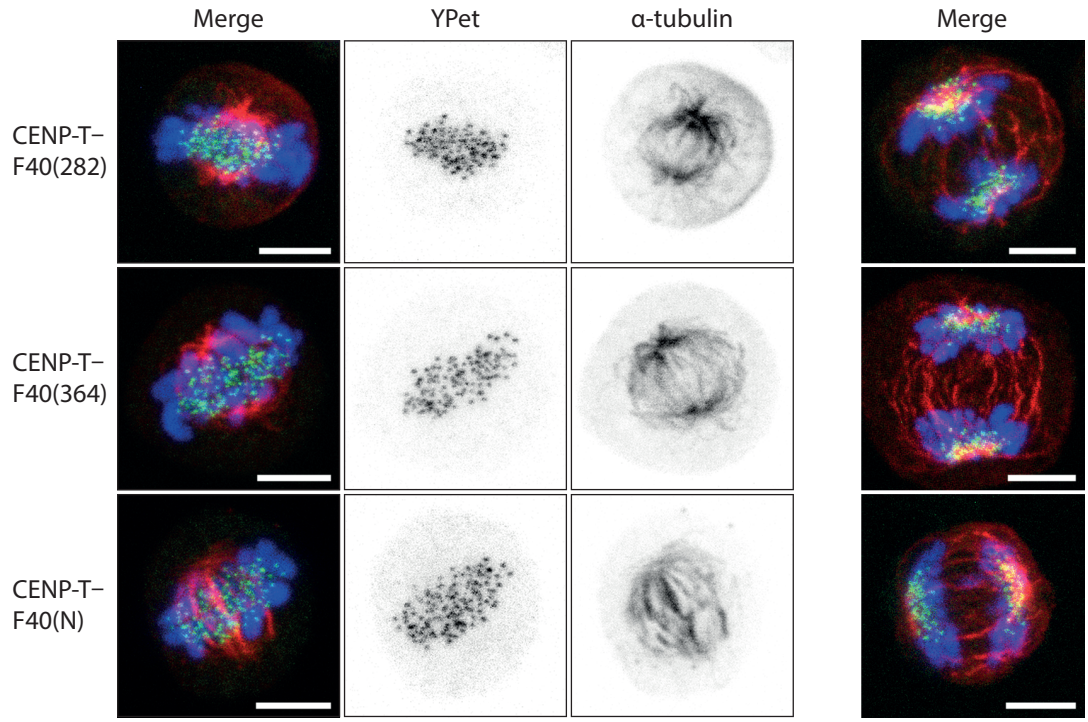

Figure 3.9: Cells expressing CENP-T biosensors form morphologically normal spindles. Immunostainings of metaphase and anaphase cells expressing the indicated constructs and depleted of wtCENP-T. Merged images show YPet fluorescence in green, α-tubulin immunostaining in red, and DAPI staining in blue. Scalebars 5 µm.

3.4 Image analysis with ratiometric FRET

Two characteristics of KTs have to be considered when designing a quantitative FRET experiment: First, they are very small and therefore projected as diffraction limited spots by a fluorescent microscope. In addition, they are rather dim and therefore prone to fast bleaching. Based on the fluorescent intensities of GFP-tagged KT components in DT40 cells, Johnston et al. [2010] estimated a number of 28 ± 4 CENP-T molecules per KT. Second, KTs oscillate during metaphase with velocities of (depending on the cell line and study) 25 to 50 µm/s [Amaro et al., 2010, Skibbens et al., 1993, Sutradhar and Paul, 2014]. Consequently, methods applicable for FRET measurements at KTs should neither require the acquisition and superimposition of non-simultaneously taken images (e.g. due to changing filters between imaging the donor and acceptor channel), nor depend on multiple rounds of excitation (which would cause bleaching after a few frames and thereby falsify FRET quantification).

A workflow that fulfills all afore mentioned requirements is ratiometric FRET analysis performed on a confocal laser scanning microscope (CLSM). Instead of utilizing filters (which absorb all light but certain wavelengths) to record only the specific emission wavelength of one fluorophore, CLSM systems utilize beamsplitters to split up the emitted light. Thereby, two or more emission channels (in this case from the donor and acceptor fluorophore) can be recorded simultaneously on two distinct detectors. Regarding sensitivity, recently developed hybrid detectors have a greatly increased performance and lower background noise as compared to conventionally applied photo multiplier tubes (PMTs), allowing precise detection even of low fluorescence.

In its pure form, ratiometric FRET analysis requires only a single round of donor excitation with simultaneous recording of the donor and acceptor fluorescence. While the signal in the donor channel comes from fluorophores that undergo no or only inefficient energy transfer to an acceptor molecule, the signal detected in the acceptor channel will be composed of light emitted by the acceptor plus bleedthrough of the donor. In addition, the acceptor fluorophore itself will be excited by energy transfer from the donor and, to a small extend, also through direct excitation by the donor excitation laser line, a phenomenon called crosstalk (also see sec. 1.4.2 for further details). In the case of unknown and varying fluorophore concentrations, this is problematic as it is not possible to distinguish between acceptor signal, donor bleedthrough, and crosstalk without the acquisition of additional reference images. However, for physically coupled FRET pairs like our biosensors, the ratio between the number of donor and acceptor fluorophores can be assumed constant and close to (but due to inefficient fluorophore maturation and beaching not exactly) 1:1. Therefore, bleedthrough

and crosstalk for a certain pair of fluorophores can be treated as a constant, which depends only on the chosen fluorophores as well as on the specific settings of the microscope.

3.4.1 Experimental design of live cell ratiometric FRET measurements

Ideally, FRET should only occur between the donor and acceptor fluorophore of the same molecule (known as *intra*molecular FRET) and be solely dependent on the length of the linker peptide. However, depending on the local density of CENP-T molecules, FRET might also occur between fluorophores of adjacent CENP-T biosensors (called *inter*molecular FRET). Without prior quantification of the levels of intermolecular FRET at the respective insertion sites, a direct comparison of FRET ratios between different CENP-T constructs is challenging and error-prone, as the FRET ratio is not exclusively determined by the length of the linker peptide.

Intermolecular FRET could be quantified by co-transfection of DNA constructs containing only the donor or acceptor fluorophore, respectively. However, due to the low number of CENP-T molecules incorporated into a single KT (see section 3.4 and 1.2.4.3), a high degree of stochastic variation between the number of incorporated donor-only and acceptor-only constructs is to be expected. Furthermore, transfection efficiencies of donor-only and acceptor-only constructs cannot be assumed to be exactly identical in every cell and a strong signal in the FRET channel could be either due to high intermolecular FRET, or caused by a higher transfection rates for the donor-only constructs in relation to the acceptor-only construct, accompanied by a correspondingly high level of bleedthrough. Both sources of signal in the FRET channel cannot be separated without the calculation of actual FRET efficiencies, which again would require the acquisition of a separate image with direct acceptor excitation, again causing the adverse effects discussed in section 3.4.

For these reasons, an alternative approach to quantify kinetochore forces which does not require direct comparison between different insertion sites was taken. In this approach, an additional zero-force condition was generated for each cell line by treating cells for approximately 1.5 h with 5 µM nocodazole. At this concentration, nocodazole completely disrupts the polymerization of MTs and thereby prevents the formation of a mitotic spindle (see figure 3.10). Due to its direct association with centromeric DNA, CENP-T remains located at KTs even in this situation, allowing the comparison of nocodazole treated cells with metaphase-cells of the same cell line. Assuming that force is transduced across CENP-T in metaphase, nocodazole treatment should result in an increased FRET ratio due to relaxation of the linker in internal CENP-T biosensors, but not in N-terminal controls.

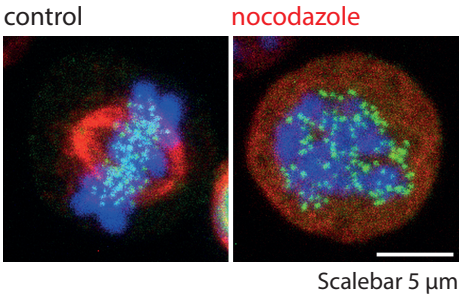

Figure 3.10: Nocodazole treatment disrupts spindle formation. Treatment of cells with 5 µM nocodazole for approximately 1.5 h disrupts the mitotic spindle while KTs are maintained as punctuate structure. Images show overlays of YPet signal from the CENP-T tension sensor (green), immunostaining of α-tubulin (red) and DNA staining with DAPI. Nocodazole was applied in a 5 000x concentrated stock solution dissolved in DMSO, control cells were treated with DMSO only.

As FRET measurements were performed on life cells, identification of mitotic cells on the basis of DNA or tubulin stainings was not possible. However, the setup of a CLSM allows the acquisition of a brightfield image simultaneously to fluorescence imaging by recording non-absorbed excitation light that passed through the sample with an additional detector. The nucleus of interphase cells (or its absence during mitosis) is well visible in these brightfield images and metaphase cells were classified by a combination of the absence of a nucleus and the pattern of the fluorescent signal emerging from KTs.

3.4.2 Kinetochore thresholding and FRET quantification

Ratiometric FRET images were evaluated using custom written Matlab software (developed by Dr. Christoph Klingner) and a workflow that is detailed in section 2.4. In brief, a region of interest (ROI) was manually drawn around each cell and within this ROI, individual KTs were identified by a multi-otsu thresholding. The FRET ratio per KT was then calculated as the quotient of the average acceptor and donor intensity per mask (see fig. 3.11).

As each individual KT mask contains only few pixels, the FRET ratio of an individual KT mask contains a high level of noise. Therefore, further analysis was performed on the median FRET ratio of all KTs within a cell.

The absolute values of donor and acceptor intensity (and therefore also the FRET ratio) directly depends on the microscope settings (excitation power, detector gain and settings for wavelength gating onto the respective detectors). Therefore, microscope settings were kept constant throughout an entire experiment.

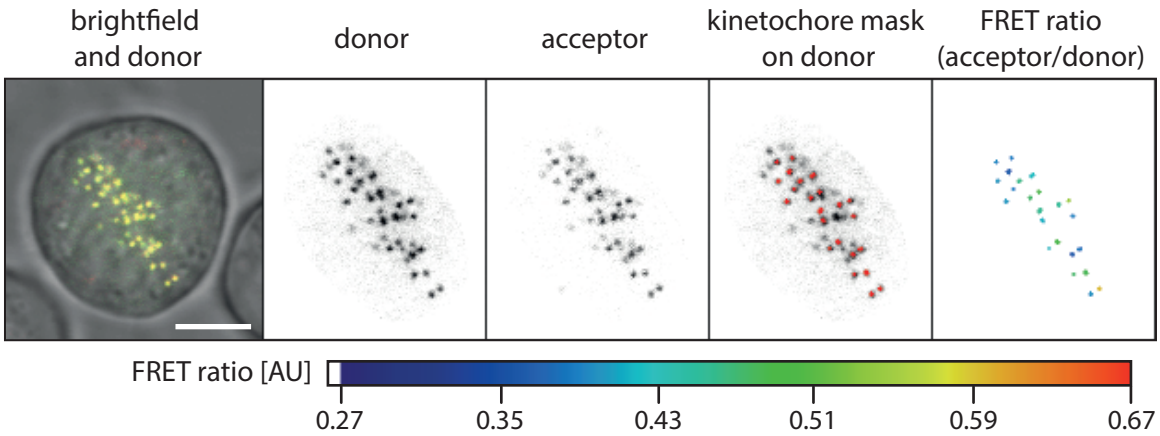

Figure 3.11: Ratiometic FRET image analysis. A region of interest was manually drawn around each cell and a mask for each KT was generated by multi-otsu thresholding. Masks that contained either saturated pixels or had an average intensity that was less than 3 times the average background intensity were excluded from further analysis. FRET ratios were calculated per mask by dividing the mean acceptor intensity by the mean donor intensity. (For better visualization in print, fluorescence signal in this figures was amplified. Image analysis was performed on the original images.) Scalebar 5 µm.

3.4.3 Donor bleedthrough is unaffected by total intensity and small chemical compounds

In order to compare FRET ratios of different constructs and treatments, microscope settings have to be chosen such that detectors operate within their linear range. When these requirements are met, the proportion of donor bleedthrough should be independent of the total donor intensity. To confirm that the settings were chosen appropriately, cell lines expressing either CENP-T–YPet(N) or CENP-T–YPet(282) were imaged and YPet bleedthrough into the mCherry detection channel was quantified. As shown in fig. 3.12 A, donor bleedthrough is independent of the fluorophore insertion site. Furthermore, no systematic correlation between YPet intensity and bleedthrough could be detected (fig. 3.12 B).

As described in section 3.4.1, KT forces will be measured by comparing metaphase cells with cells after nocodazole treatment. It is therefore crucial that neither nocodazole, nor the solvent DMSO affects fluorescence, which was exemplarily tested for the CENP-T–YPet(282) cell line. Exposure to 5 µM nocodazole (dissolved in DMSO and administered in a 1:5 000 dilution) or DMSO alone (also 1:5 000) neither affected average YPet intensity, nor the quantity of donor bleedthrough (fig. 3.13).

The effect of both chemicals on the acceptor fluorophore mCherry was indirectly evaluated by treating cells expressing the N-terminal control construct with nocodazole, which had no influence on FRET (see later chapters).

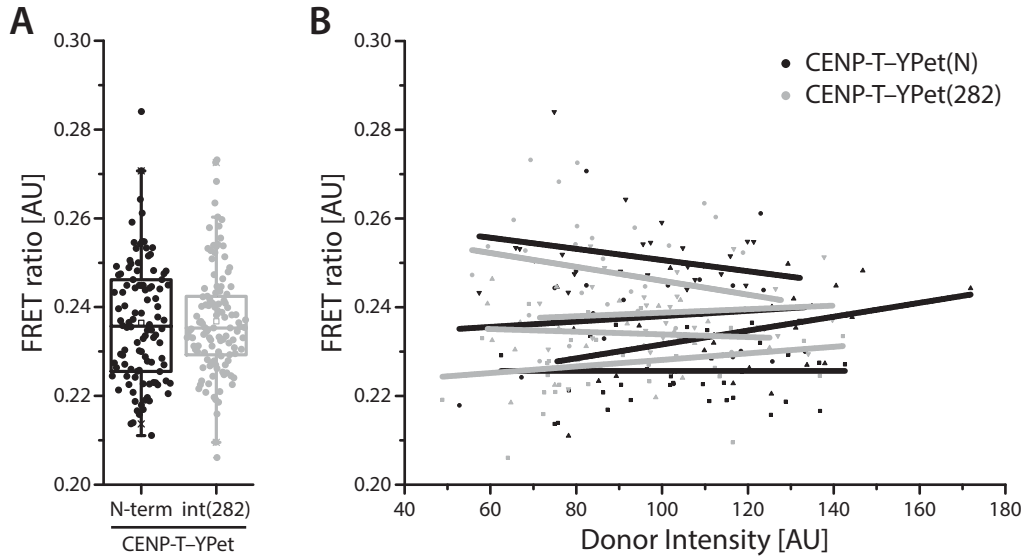

Figure 3.12: Donor bleedthrough is independent of fluorophore position and intensity. **A)** In cells that express only the donor but no acceptor fluorophore, the FRET ratio is a measure for the bleedthrough of donor fluorescence into the acceptor channel. YPet was attached to CENP-T either N-terminally, or inserted after aa 282. n = 106 and 117 cells for CENP-T–YPet(N) and CENP-T–YPet(282), respectively, from four independent experiments. **B)** No correlation between bleedthrough and YPet intensity could be detected. Data were individually fitted for each experimental day. Correlation coefficients (Pearson's r) are 0.100, -0.001, 0.385, and -0.286 for CENP-T–YPet(N) and -0.214, 0.227, -0.078, and 0.099 for CENP-T–YPet(282).

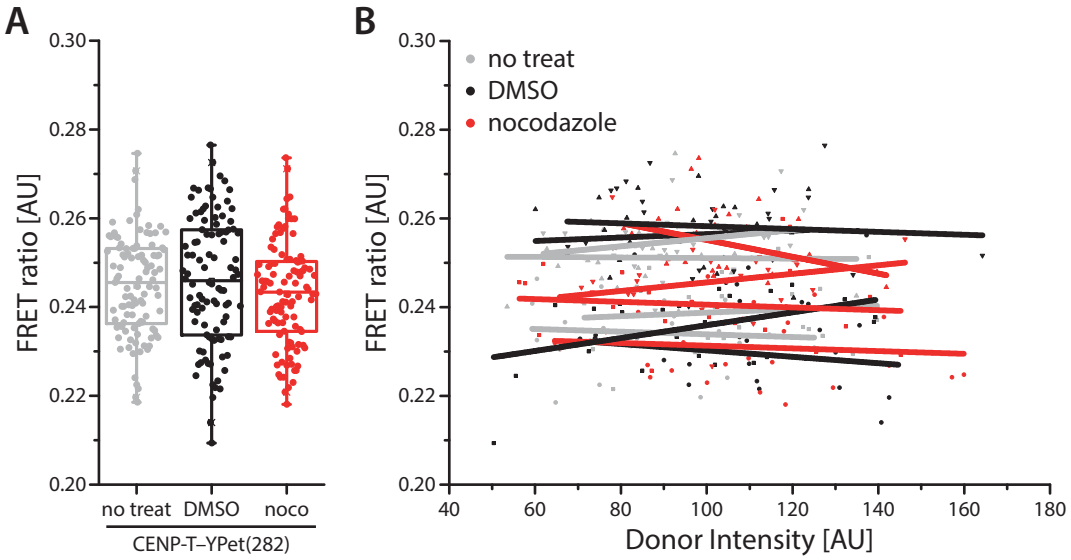

Figure 3.13: DMSO and nocodazole do not affect donor bleedthrough. **A)** Neither treatment with DMSO alone (1:5 000) or nocodazole dissolved in DMSO had an effect on donor bleedthrough. Data are from four independent experiments, n = 103, 102 and 106 cells for no treat, DMSO, and nocodazole, respectively. **B)** No correlation between bleedthrough and YPet intensity could be detected. Data were individually fitted for each experimental day. Correlation coefficients (Pearson's r) are -0.078, 0.099, -0.015, and 0.236 for no treat; -0.139, 0.431, 0.0772, and -0.083 for DMSO; and -0.083, -0.101, -0.353, and 0.214 for nocodazole.

3.5 Initial evaluation of potential CENP-T tension sensors

After proving that all CENP-T biosensors are biologically functional (rescued growth after knockdown of wtCENP-T and morphologically normal mitotic spindles, fig. 3.8 and 3.9, sec. 3.3.4), FRET measurements were performed to evaluate if the sensors are able to detect forces by elongation of the tension sensitive peptide and corresponding reduction in FRET. Cell lines expressing either one of the internally integrated F40 tension sensors or the N-terminally fused zero-force control were treated with DMSO (mock treatment, also referred to as "untreated" hereafter) or nocodazole. Live cell FRET measurements of untreated cells during metaphase and nocodazole treated cells were performed on a Leica SP5 confocal system. After acquisition, images were subsequently thresholded and quantified as described in sections 3.4.2 and 2.4.

Image quantification revealed that all cell lines express fluorescently marked CENP-T to similar levels as demonstrated by comparable donor intensities (shown in fig. 3.14 A). Treatment with nocodazole slightly reduced the average donor intensity in all cell lines; however, due to the large spread within each cell line and condition, this effect is only of weak (N-terminal and internal-282) or no (internal-364) significance.

With respect to FRET ratios (fig. 3.14 B), the N-terminal control and the internal sensor at position 282 showed a slight but non-significant increase upon nocodazole treatment (p-values 0.076 for N-terminal control and 0.165 for position 282, Mann-Whitney U Test).

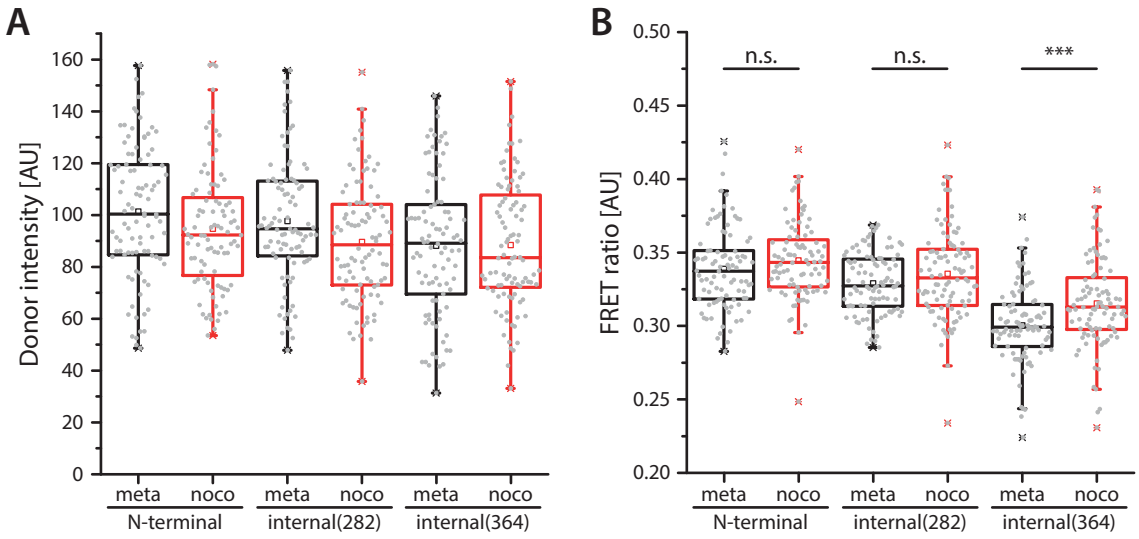

Figure 3.14: Analysis of different CENP-T integration sites. A) Median donor intensities of cells expressing either the F40 N-terminal control construct or one of the internal tension sensor constructs. **B)** FRET ratios of the same cells as shown in A). Median FRET ratios (in the same order as shown in the graph) are 0.337, 0.343, 0.327, 0.333, 0.299, and 0.313. Number of cells n = 94, 92, 96, 98, 94, and 96 cells from 5 independent experiments, Mann-Whitney U Test, ***: p-value < 0.001.

For the internal sensor at position 364, the relative FRET increase between metaphase and nocodazole was more pronounced (p-value 2.90×10^{-4}). It has to be noted, however, that despite the relative increase, FRET ratios of this construct were generally reduced as compared to the internal 282 insertion site and the N-terminal control. At this point, it can only be speculated about the origin of this decrease; site specific fluorophore folding/maturation efficiencies and different levels of intermolecular FRET are likely causes.

3.6 CENP-T forces are detected by the 1–6 pN F40 sensor module

The initial CENP-T–F40 tension measurements shown in figure 3.14 were performed at room temperature and it cannot be excluded that this shift in temperature had an effect on the process of cell division and its mechanics. This initial experiment was therefore repeated at a comparable confocal system, but this time with an integrated heating chamber, so that cells could be kept at 37 °C throughout the entire experiment.

Due to the almost identical technical setup of the previously used Leica SP5 and the henceforth used Leica SP8 system, most of the settings could be directly reapplied. Adjustments had to be made only with regard to the laser power and, since the SP8 was built with redesigned internal optics, the magnification (see sec. 2.4.1. Additionally, the gating for the acceptor channel was adjusted from 600–700 nm (SP5) to 580–700 nm (SP8). This adaptation allowed better coverage of the donor emission spectrum, however, on the cost of slightly elevated donor bleedthrough. While increased bleedthrough may be seen disadvantageous at first intuition, it proved valuable during the process of image analysis as it made the detection of KTs in the acceptor image more reliable.

The data collected on the new system showed a decreased average donor intensity (which can be easily explained by a slightly reduced output laser power, fig. 3.15 A) and a slight elevation of total FRET ratios as a consequence of the changed acceptor gating. Despite these differences, the first three replications of the experiment reliably reproduced the data collected at room temperature, namely a significantly increased FRET ratio following nocodazole treatment in CENP-T–F40(364) cells, but no change in the N-terminal control and at integration site 282. I therefore stopped the analysis of insertion site 282 at this point and explored only the CENP-T–F40(364) in more detail (fig. 3.15 B).

The fact that only one of the two internal constructs is sensitive to forces exerted by the mitotic spindle seems to be inconsistent at first glance. However, such a discrepancy is not surprising, considering the key requirements that have to be fulfilled to build a functional

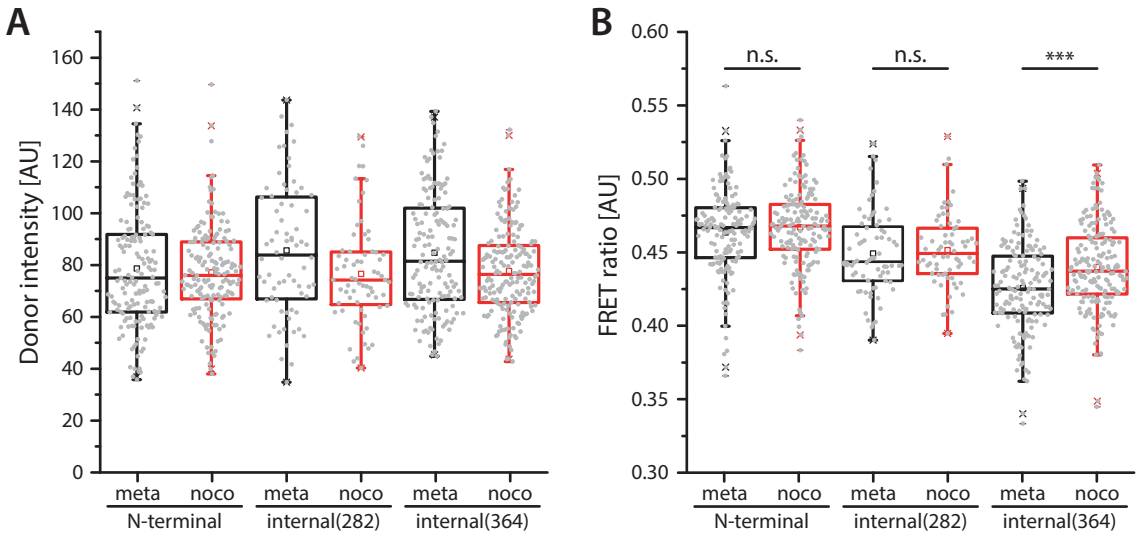

Figure 3.15: CENP-T force analysis with the 1–6 pN F40 sensor. A) Median donor intensities of cells expressing either the F40 N-terminal control construct or one of the internal tension sensor constructs. **B)** Median FRET ratios of the same cells as shown in A), in numbers: 0.467, 0.468, 0.444, 0.449, 0.425, and 0.437. n = 157, 167, 72, 68, 156, and 182 cells; number of independent experiments N = 8, 8, 3, 3, 8, and 8 independent experiments. Mann-Whitney *U* Test, ***: p-value < 0.001.

tension sensor. Despite the obvious premise that the protein has to remain functional after tension sensor integration (which could be confirmed for all three CENP-T sensors by rescue of the lethality of wtCENP-T knockout (see section 3.3.4), the sensor must be integrated at a position that experiences linear tension in the direction of the linker peptide. Furthermore, the quaternary protein structure must be such that the TSM forms the weakest link at its respective position and both fluorophores must have enough space to freely rotate. It is therefore possible, that additional KT proteins prevent sensor elongation or fluorophore rotation only at one, but not at the other internal integration site or that the direction of forces acting at integration site 282 is not parallel to the linker. For these reasons, only integration site 364 was considered for further analysis.

3.6.1 Advantages and limitations of the F40 tension sensor

As shown in fig. 1.11 E, the F40 linker peptide is characterized by an almost linear relationship between FRET efficiency and applied force in the range of 1–6 pN. While this sensitivity profile is highly advantageous for initial and qualitative force measurements (i.e. is the targeted protein under force at all?), it is sub-optimal for a more detailed quantification of forces for two reasons:

First, the mean FRET ratio obtained by averaging the signal from hundreds of CENP-T molecules per cell does not allow drawing any conclusion about the actual status of an

individual molecule. In particular, it is unknown if many molecules are under a similar level of tension, or if only very few molecules experience high tension (resulting in very low to no FRET), whereas the majority of molecules is not under force at all [Freikamp et al., 2016]. Calculation of FRET ratios not for a whole cell but on the level of individual KTs would partially improve the resolution by reducing the number of averaged molecules to a few tens, but on the cost of a significantly worsened signal-to-noise ratio due to the small area of an individual KT that covers only a few pixels.

The second reason why the F40 TSM alone is not sufficient for detailed force quantification is the dynamic range of the linker peptide, which is limited to 6 pN. Forces higher than this threshold can still be detected, but not resolved by the F40 sensor. In addition, it has been proposed (but not yet proven) that the F40 peptide is sensitive to compression, resulting in increased levels of FRET as compared to its resting state [Rothenberg et al., 2015]. Consequently, it is possible that the measured average is underestimating the real average force per molecule.

As both of the above described phenomena occur simultaneously, the parallel application of several TSMs covering distinct force ranges is a prerequisite if forces should be not only qualitatively analyzed but also quantified. I therefore decided to next analyze CENP-T forces with a stiffer sensor module which is sensitive to forces above 6 pN.

3.7 CENP-T forces are lower than 6 pN

The HP35 peptide is an ultra-fast folding domain of the actin-binding protein villin and has been thoroughly characterized by single-molecule force spectroscopy [Žoldák et al., 2013]. Despite originating from an actin-binding protein, the 35 amino acid long headpiece does not interact with actin, thus allowing the use of HP35 as linker peptide in TSMs [Austen et al., 2015]. As shown in fig. 1.11 D and E, the HP35 sensor shows highest sensitivity between 6 and 8 pN.

To test whether CENP-T is exposed to forces higher than 6 pN, the HP35 sensor module was integrated into CENP-T at position 364; additionally, an N-terminal zero-force construct was made.

Stable cell lines were generated using the same protocol as for the F40 sensors, followed by subsequent depletion of wtCENP-T. Immunostainings of metaphase and anaphase cells demonstrated that CENP-T–HP35 sensors localize to KTs and formation of the mitotic spindle is undisturbed (fig. 3.16 A). Furthermore, growth rates of CENP-T–HP35 cells under the administration of doxycycline recovered to the rate of CENP-T$^{\text{tet-off}}$ cells that were cultured in the absence of doxycycline (fig. 3.16 B).

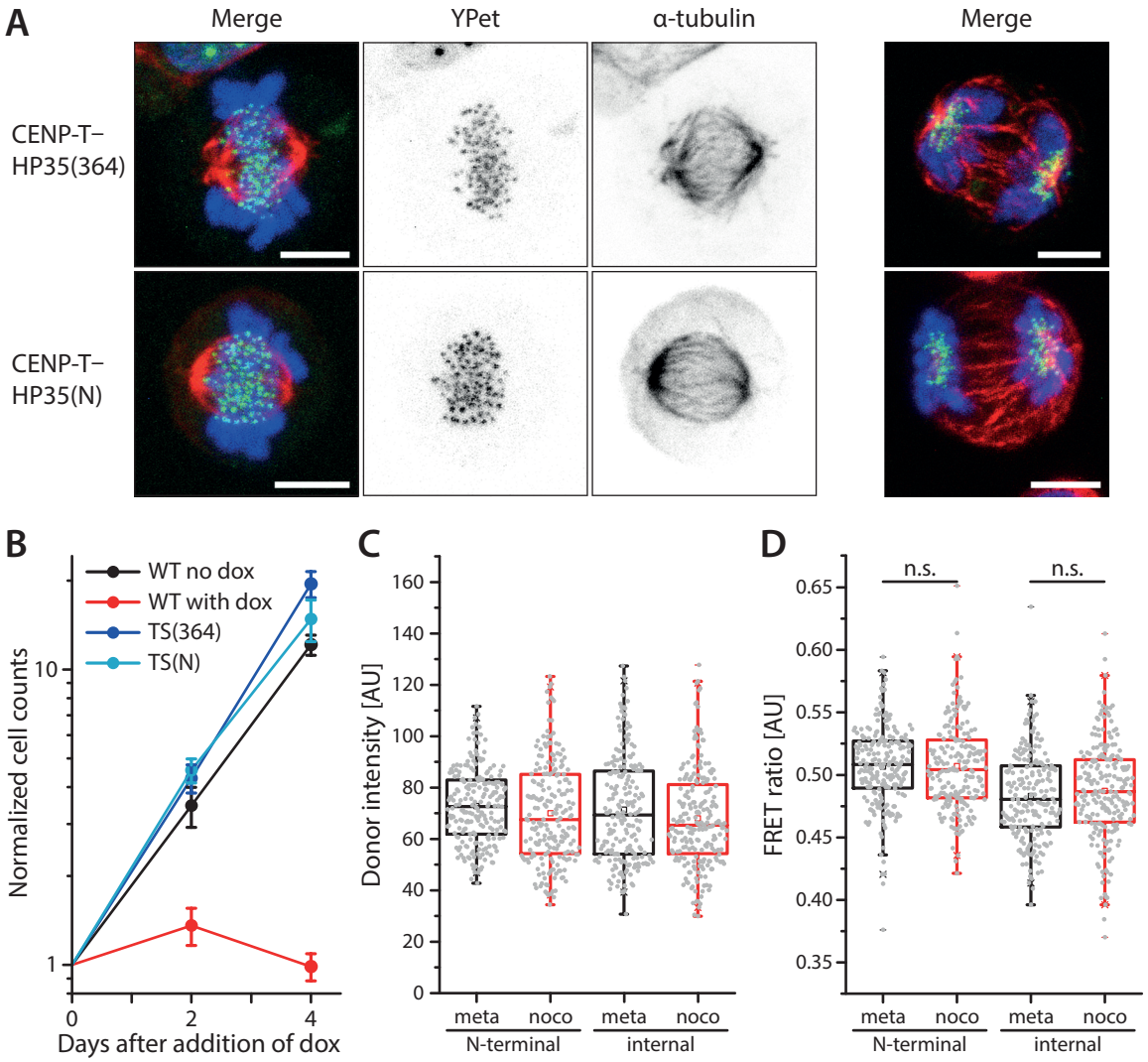

Figure 3.16: CENP-T force analysis with the 6–8 pN HP35 sensor. A) Immunostainings of metaphase and anaphase cells expressing the indicated constructs and depleted of wtCENP-T. Merged images show YPet fluorescence in green, α-tubulin immunostaining in red and DAPI staining in blue. Scalebars 5 µm. **B)** Cell growth after addition of doxycycline at day 0. The internal biosensor as well as the control rescues lethality of wtCENP-T depletion and restores normal growth rates. Plot depicts mean cell counts and standard deviation of three independent experiments. **C)** Median donor intensities of cells expressing either the HP35 N-terminal control construct or the internal tension sensor construct. **D)** Median FRET ratios of the same cells as shown in C). FRET ratios in numbers: 0.508, 0.504, 0.480, and 0.487. n = 216, 203, 209 and 224 cells from 8 independent experiments, Mann-Whitney *U* Test, ***: p-value < 0.001.

As already seen for the F40 sensors, treatment with nocodazole neither changed the total donor intensity, nor FRET ratios of the N-terminal control (p-value 0.510, Mann-Whitney *U* Test); the internal CENP-T–HP35(364) did not show the force dependent decrease in FRET that was observed with the F40 module at the same position (p-value 0.145). It has to be noted, however, that FRET ratios for the internal construct at position 364 are generally reduced as compared to the N-terminal control (fig. 3.16 C and D) – an effect that could be seen already for the respective F40 sensors.

3.7.1 Combined results of F40 and HP35 biosensors

Analysis of the F40 biosensors raised the hypothesis that the decreased FRET ratio of CENP-T–F40(364) is the consequence of linker elongation due to force, while the sensor module at position 282 is unable to report forces. However, with data of only a single sensor module, it could not be ruled out that the increased FRET ratio at position 364 is caused by an artifact instead of force. As the F40 and HP35 sensor modules differ only in the very short linker region (40 amino acids for the F40 module and 35 amino acids for the HP35 module, respectively), such artifacts are likely to be determined by the integration site rather than being dependent on the exact linker sequence. Combination of the data obtained for CENP-T–F40(364) and CENP-T–HP35(364) sensors supports the hypothesis that CENP-T is indeed subjected to forces, which are, however, within the lower single pN range and therefore high enough to evoke a response of the F40 sensor, but not sufficient to cause a significant reduction of FRET if the HP35 sensor is applied. Nevertheless, a more detailed force analysis with sensors showing increased sensitivity and discrimination power within the low pN range would be necessary to further test this hypothesis.

3.8 Development of new low-force sensors with increased sensitivity

The F40 sensor with its rather broad and almost linear sensitivity profile is an ideal module for initial force analyses of rather qualitative nature. For conducting more detailed analyses, however, it has three shortcomings: First, despite the almost linear behavior, mean forces per molecule cannot be reliably calculated because its resolution is limited to forces lower than 6 pN. Second, the broad sensitivity spectrum from 1 to 6 pN in combination with the rather low starting FRET of no more than 25 % comes at the cost of a rather weak resolution power for small differences. And third, the F40 sensor has been reported to be sensitive to compression [Rothenberg et al., 2015]. If this experimentally not yet verified assumption holds true, tension in oscillating systems like the mitotic spindle may be masked, as some KTs show decreased FRET due to tension while others show increased FRET caused by compression.

Together, these three reasons constitute the need for the development of additional TSMs with sensitivities below 6 pN and, ideally, a narrow transition range from fully closed to fully opened.

3.8.1 Destabilized mutants of HP35

The HP35 peptide is widely used as a model of protein folding and various mutations have been introduced into the peptide in order to change folding behavior and stability. Through replacing the wild type HP35 by a stabilized mutant HP35st (fig. 3.17 A) [Žoldák et al., 2013], a third TSM that is sensitive for 9 – 11 pN could be successfully generated (see fig. 1.11) [Austen et al., 2015].

For best comparison of the results obtained with different TSMs, the linkers should be structurally as similar as possible. We therefore thought to expand our set of TSMs with additional variants of the villin headpiece peptide, carrying destabilizing mutations.

A cluster of three conserved phenylalanine residues that forms most of HP35's hydrophobic core (fig. 3.17 B) has been the focus of two studies by Frank et al. [2002] and Xiao et al. [2009]. Substitution of phenylalanines (F) by leucines (L) and subsequent analysis with circular dichroism (CD) and 1D-nuclear magnetic resonance (NMR) spectroscopy revealed that all three single mutants as well as the F5L/F10L double mutant are destabilized, but still properly folding. Double mutants that involved F17A, on the contrary, failed to adopt the native structure of the villin headpiece [Frank et al., 2002]. When the same F→L substitutions were combined with the two stabilizing mutations of the HP35st peptide, a complete set comprising three single, three double and the triple F→L mutant could be generated and all constructs were well-folded [Xiao et al., 2009].

Based on these biophysical characterizations, five different destabilized HP35 mutants (fig. 3.17 C) were inserted between the YPet–mCherry FRET pair and expressed cytosolically in mouse embryonic fibroblasts. FLIM analysis of these TSM candidates revealed that, in comparison to the cytosolically expressed HP35st module, only those with a single destabilizing mutation (HP35st +/– and HP35st –/+) showed normal FRET efficiencies, while all other mutants had reduced energy transfer rates (fig. 3.17 D). The most probable explanation for this reduced energy transfer is that the peptide still adopts the native conformation *when* folded. However, the folding energy of these mutants is reduced so much, that the peptide occasionally transits to an unfolded state even if no external force is applied, making them unsuited as TSM linkers. The two constructs that had FRET efficiencies comparable to those of HP35st had folding energies (ΔG^0) close to wt HP35 (fig. 3.17 C). It can therefore be expected that the sensitivity spectrum of these linkers would greatly overlap with that of the already established HP35 TSM.

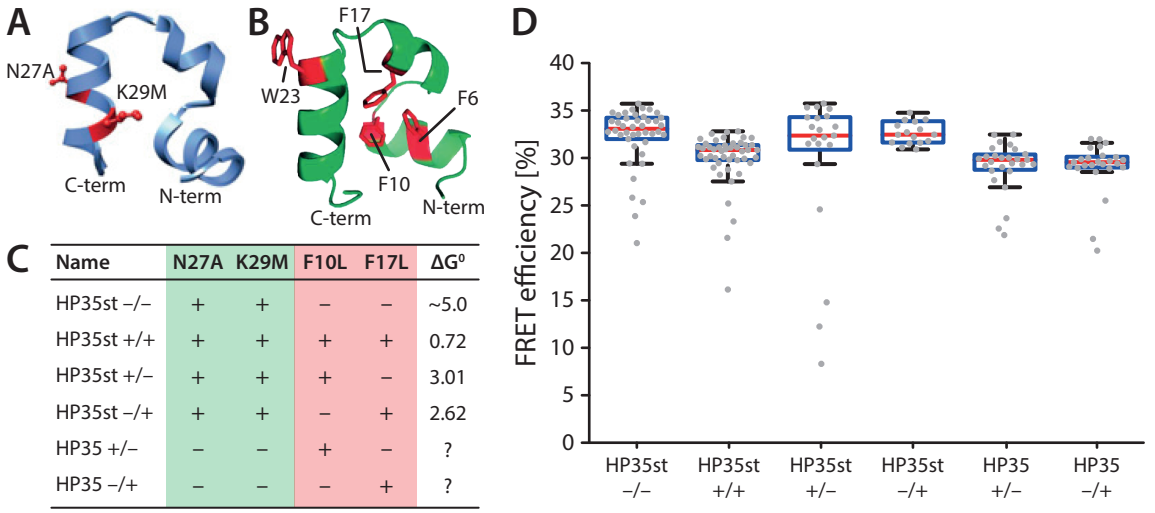

C

Name	N27A	K29M	F10L	F17L	ΔG⁰
HP35st −/−	+	+	−	−	~5.0
HP35st +/+	+	+	+	+	0.72
HP35st +/−	+	+	+	−	3.01
HP35st −/+	+	+	−	+	2.62
HP35 +/−	−	−	+	−	?
HP35 −/+	−	−	−	+	?

Figure 3.17: Cytosolic FRET measurements of destabilized HP35 sensor modules. A) The stabilized HP35st peptide was generated by introduction of two point mutations N27A and K29M [Žoldák et al., 2013]. **B)** Three phenylalanine residues F6, F10, and F17 stabilize HP35 by the formation of hydrophobic interaction withing the HP35 core. Mutating these residues to leucine significantly destabilizes HP35 [Frank et al., 2002]. **C)** Five destabilized mutants of the HP35 peptide were chosen as new linker candidates. Values for ΔG^0 [kcal/mol] from Xiao et al. [2009]. As comparison: ΔG^0 of HP35 $\approx$ 2.5 kcal/mol (calculated from Žoldák et al. [2013]). **D)** FRET efficiencies of cytosolically expressed TSMs with the indicated linker peptide. HP35st −/− serves as reference. n = 42, 47, 21, 17, 27, and 25 cells from N = 4, 4, 2, 2, 1, and 1 experimental days.

3.8.2 Ferredoxin-like fold and EF-hand motives as new sensor candidates

Besides destabilized HP35 mutants, two additional domains were tested for their suitability as linker peptides: a *de novo*-designed domain resembling a ferredoxin-like fold structure (FL) and a calcium-independent EF-hand motive, comprising the EF-hands 3 and 4 of human actinin alpha 2 (fig. 3.18 A and B). When forming a protein-based hydrogel, the FL domain unfolds at ~5 pN [Fang et al., 2013], while the EF-hand was estimated to unfold in the range of 2 – 3.5 pN (personal communication with Marco Grison from the lab of Matthias Rief).

The N- and C-termini of a folded linker peptide should be as close as possible to obtain high FRET in the resting state. At the same time, however, the construct must be flexible enough to ensure proper folding of the individual domains and allow free rotation of the fluorophores. For this reason, two versions of each putative module were generated. Three glycine residues were added to each side of the naturally very compact FL domain to obtain a version with increased flexibility [FL(li)]. The EF-hand, on the other hand, already contains flexible domains at the N- and C-termini and a shortened variant lacking the first five N-terminal and the last four C-terminal amino acids was generated [EF(s)].

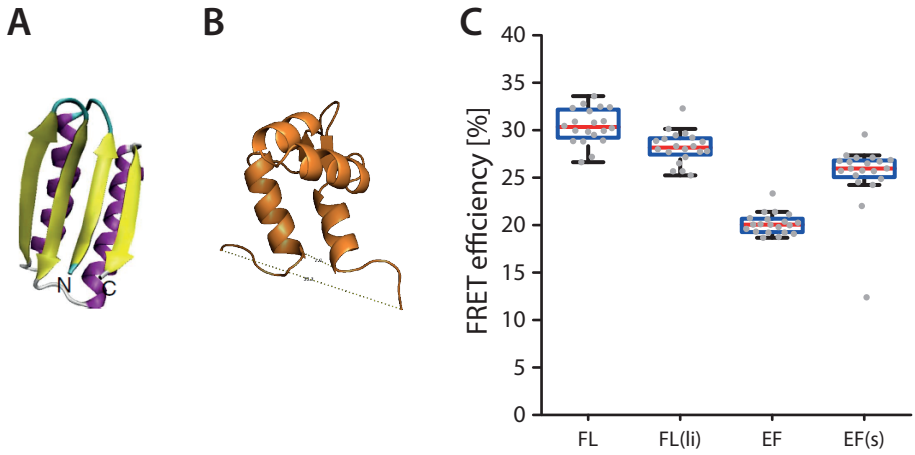

Figure 3.18: Cytosolic FRET measurements of FL and EF sensor modules. A) Structure of the *de novo*-designed ferredoxin-like fold domain (FL) (modified from Fang et al. [2013]). **B)** Structure of the EF-hands 3 and 4 of human actinin alpha 2. **C)** FRET efficiencies of TSMs cytosolically expressed in mouse embryonic fibroblasts and analyzed by FLIM. FL: ferredoxin-like fold domain, FL(li): FL domain flanked by three glycine residues to increase flexibility, EF: full-length EF-hand motive, EF(s): EF-hand motive shortened by five N- and four C-terminal amino acids. For all constructs: n = 20 cells from two experimental days.

All four putative TSMs were expressed cytosolically in mouse embryonic fibroblasts and analyzed by FLIM (fig. 3.18 C). As expected, observed FRET efficiencies were between 20 and 30 % and the shorter variants had increased energy transfer as compared to the longer analogs, indicating that all four constructs folded properly. It was therefore decided to continue with the shorter version of each construct to maximize starting FRET efficiency and thereby increase the dynamic range.

3.8.3 FL- and EF-based tension sensors are functional in the focal adhesion protein talin

After it was shown that both new modules adopt a folded conformation and show sufficient energy transfer when expressed cytosolically, they were introduced into the focal adhesion protein talin for additional testing. Talin's head domain binds to membrane-spanning integrins, while the talin tail interacts with the actin cytoskeleton. Talin force transduction has been well studied in our lab; it was shown by application of the previously calibrated F40, HP35 and HP35st modules that talin is under forces > 7 pN [Austen et al., 2015] and thus a suitable model for testing functionality of the new sensor modules.

Talin tension sensor generation, live cell imaging, and data evaluation were performed as described in Austen et al. [2013]. In brief, the TSM was either inserted between talin's head and tail domain, or attached C-terminally as zero-force control. Live cells were imaged by FLIM and focal adhesion signal was extracted by multi-otsu thresholding (fig. 3.19 A).

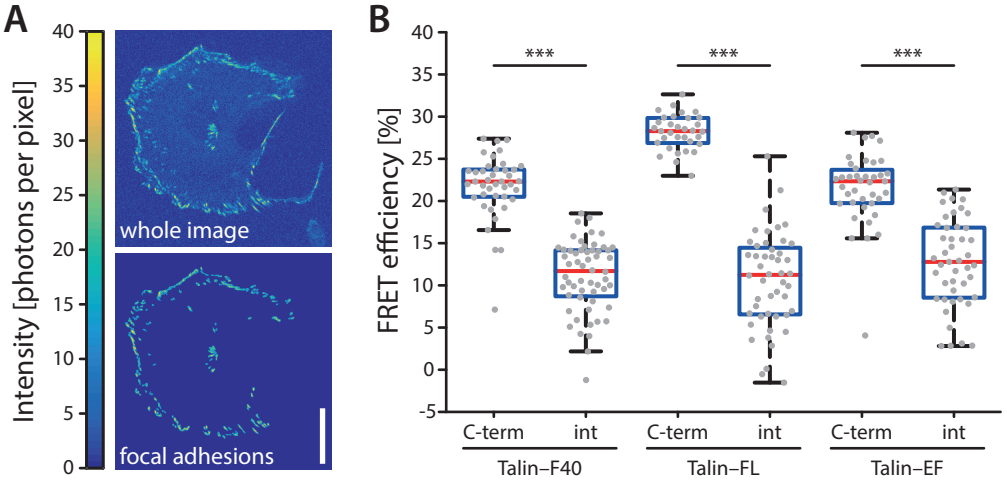

Figure 3.19: FL and EF tension sensor modules are functional in talin. A) Intensity images generated from FLIM data showing a talin–FL(int) cell before (upper) and after (lower) focal adhesion isolation. Scalebar 20 µm. **B)** FRET efficiencies obtained by FLIM microscopy for three TSMs. n = 41, 56, 33, 48, 39, and 45 cells from 4 independent experiments. Kolmogorov-Smirnov-Test, ***: p-value < 0.001.

Afterwards, the mean FRET efficiency across all focal adhesions of one cell was determined. The new talin–FL and talin–EF sensors were compared with the previously established talin–F40 sensor (fig. 3.19 B).

Both new TSMs report force along talin by a significantly reduced FRET. While starting FRET and dynamic range of the EF sensor are comparable to the F40 sensor, FL shows a greatly increased starting FRET but the same residual FRET when under force. This increased dynamic range is particularly advantageous for ratiometric FRET experiments, where the maximal difference between high an low FRET is partially masked by donor bleedthrough and acceptor crosstalk, which is both added as a constant to the FRET efficiency. Based on these data, I decided to proceed with the FL sensor module for single molecule calibration.

3.8.4 Single molecule calibration of the FL tension sensor module

The full length TSM, comprising the donor fluorophore YPet, the short version of the FL linker, and the acceptor fluorophore mCherry was calibrated by single–molecule force spectroscopy, using the same dual optical trap setup as for calibration of the HP35 and HP35st modules (see fig. 1.11 B and Austen et al. [2015]). Calibration was performed in collaboration with the Lab of Matthias Rief (Technical University Munich) and carried out by Andreas Weißl and Alexander Mehlich. When kept at a constant force of no more than 3.1 pN, the module predominantly adopted the folded state, but switched to mostly unfolded when hold at 5.1 pN. When constantly hold at 4.2 pN, both unfolded and folded states

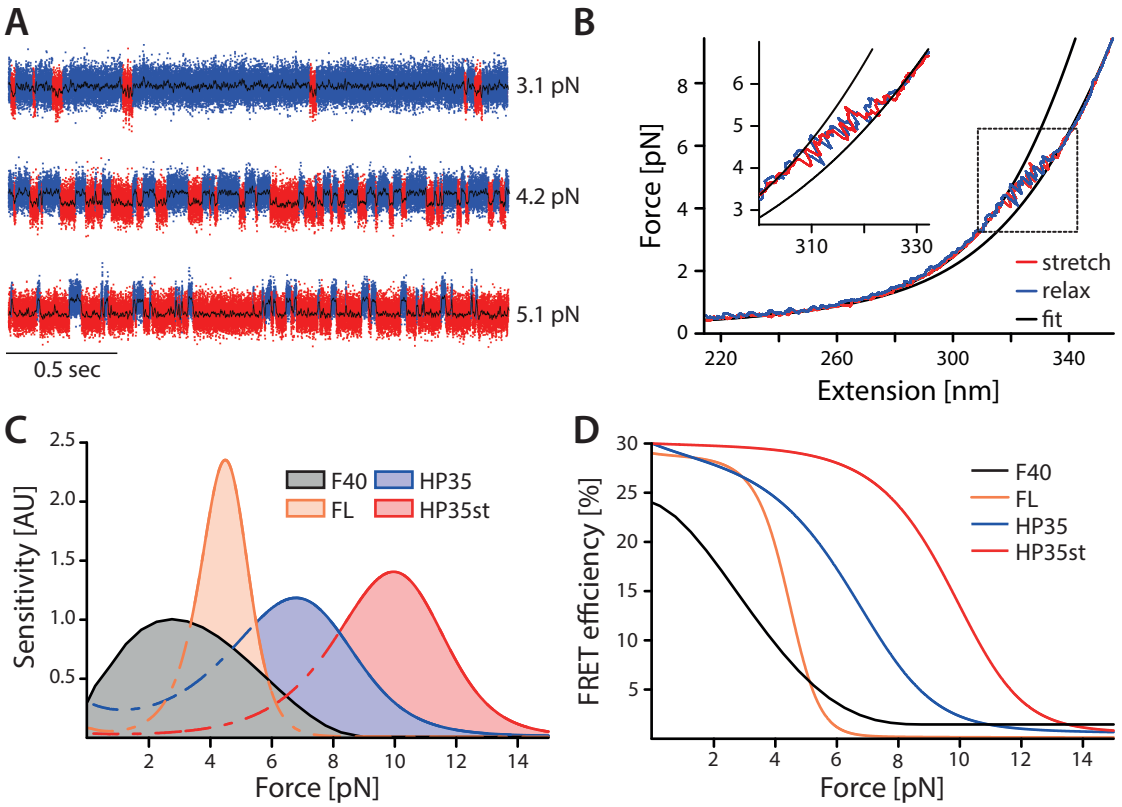

Figure 3.20: Single molecule calibration of the FL tension sensor module. Calibration of the module was performed with a dual optical trap as shown in fig. 1.11 B. **A)** The optical trap was set to a constant force and elongation of the sensor module was recorded. At 3.1 pN, the module was predominantly in the closed (blue track) and at 5.1 pN in the unfolded (red track) state. An equilibrium of 50 % open and closed states was observed when the module was hold at 4.2 pN. **B)** Force–extension plot showing unfolding (red) and refolding (blue) traces of the FL sensor module. Black lines show worm-like chain model fits. **C)** and **D)** Sensitivity vs. force and FRET efficiency vs. force plots comparing the four calibrated TSMs.

were about equally populated (fig. 3.20 A). Long-lived conformations with partially unfolded linker could not be observed, indicating that the domain undergoes a defined conformational change from folded to unfolded rather than gradual unzipping of the individual subdomains.

When the bead distance was continuously increased and decreased while measuring the applied force, no hysteresis between unfolding and refolding could be detected as long as no unphysiologically high pulling velocities were applied (fig. 3.20 B).

In accordance with these force-extension curves, the new FL modules shows a much more pronounced sensitivity–force correlation as compared to the three previously calibrated TSMs and the F40 module in particular (fig. 3.20 C), which is also reflected in the FRET–to–force plot (fig. 3.20 D). The complete insensitivity of the FL sensor to forces below 2 pN is of particular importance as this eliminates mechanical noise. In addition, the length

increase of the FL sensor is much larger than for previously developed sensors, resulting in the total absence of FRET in the open state.

In summary, the FL peptide makes an excellent new tension sensor molecule to report forces that are ≥ 3 pN.

3.9 CENP-T forces exceed 3 pN

Application of the F40 and HP35 sensors suggested that CENP-T is under force during metaphase, and that these forces are lower than 6 pN. Additionally, Ye et al. [2016] meanwhile report that metaphase forces across CENP-C are, on average, ∼1–2 pN in *D. melanogaster* S2 cells. If this average force represents indeed what the majority of molecules experiences, the force along an individual KT connector would be very close to the mechanical noise. It is therefore likely that at any time, only a subpopulation of molecules is actively involved in mechanotransduction and that these molecules experience forces higher than 2 pN, while other molecules are not under force in that given moment and thus lower the total average. To test whether CENP-T is exposed to higher forces, I generated CENP-T–FL biosensors by inserting the module either after amino acid 364 or attaching it N-terminally as zero force control. Stable cell lines on a conditional CENP-T knockout background were generated as described previously.

As expected, CENP-T–FL cell lines form morphologically normal spindles and CENP-T–FL constructs rescue the lethal effects of CENP-T knockout (fig. 3.21 A and B). Treatment of CENP-T–FL cell with nocodazole neither affected donor intensities (fig. 3.21 C), nor the FRET ratio of mitotic CENP-T–FL(N) cells (p-value 0.281, Mann-Whitney *U* Test); however, nocodazole treated CENP-T–FL(int) cells showed significantly increased FRET as compared to cells imaged in metaphase (p-value 1.34×10^{-7}). As the new FL sensor is insensitive to forces below 3 pN, these data demonstrate that a population of CENP-T experiences forces exceeding this threshold.

In combination with the results obtained from the F40 and HP35 sensors, I concluded that CENP-T experiences mechanical forces during mitosis, which exceed 3 pN and are therefore clearly above mechanical noise, but are not increased above 6 pN.

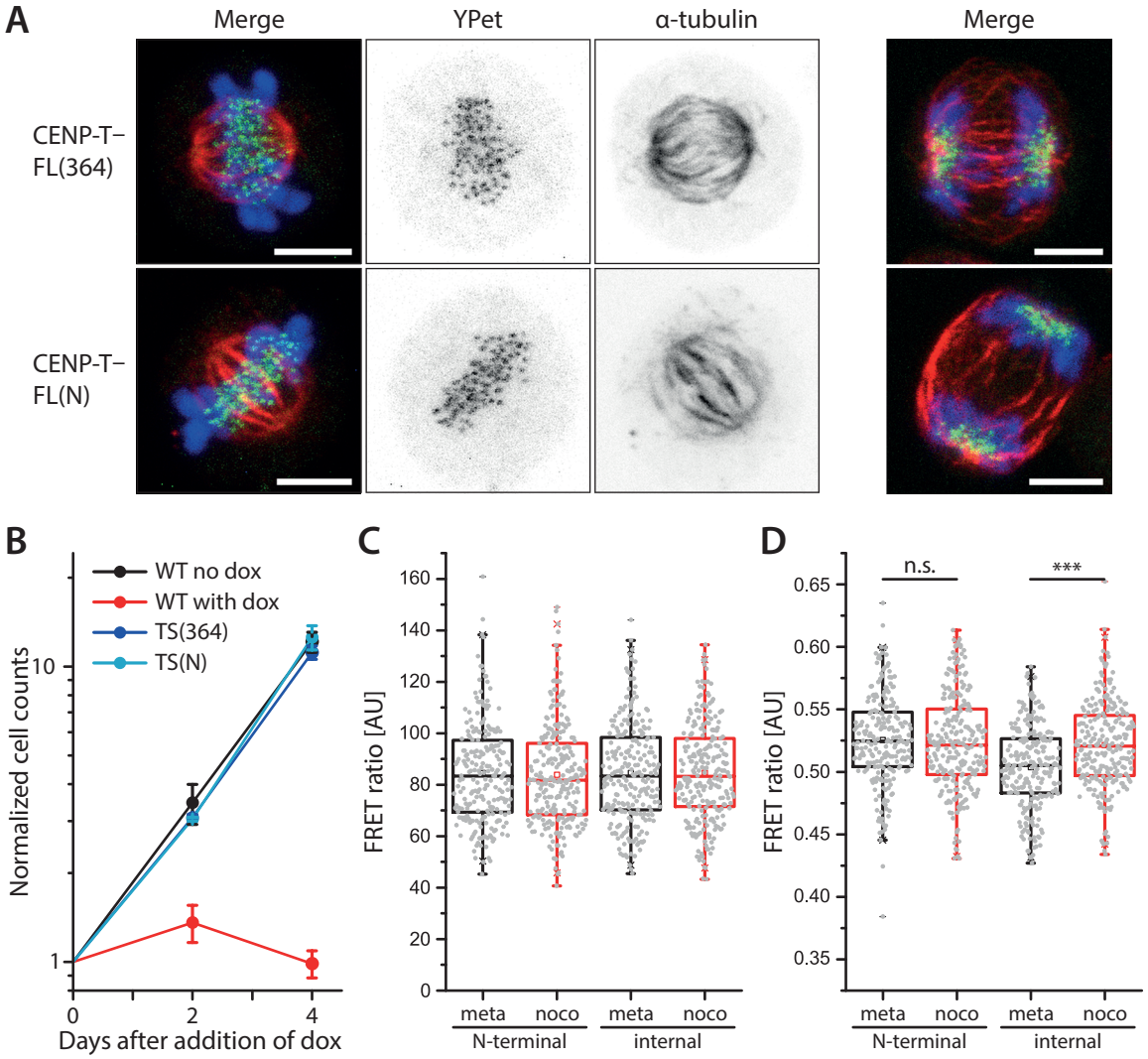

Figure 3.21: CENP-T force analysis with the 3–5 pN FL sensor. **A)** Immunostainings of metaphase and anaphase cells expressing the indicated CENP-T–FL constructs and depleted of wtCENP-T. Merged images show YPet fluorescence in green, α-tubulin immunostaining in red and DAPI staining in blue. Scalebars 5 µm. **B)** Cell growth after addition of doxycycline at day 0. The internal biosensor as well as the N-terminal construct rescue lethality of wtCENP-T depletion and restore normal growth rates. Plot depicts mean cell counts and standard deviation of three independent experiments. **C)** Median donor intensities of cells expressing either the FL N-terminal control construct or the internal tension sensor construct. **D)** Median FRET ratios of the same cells as shown in C). FRET ratios in numbers: 0.525, 0.521, 0.505, and 0.521. n = 259, 278, 268, and 276 cells from 9 independent experiments, Mann-Whitney *U* Test, ***: p-value < 0.001.

3.10 Advanced statistical analysis of the three CENP-T tension sensors

Due to the low signal intensity and the small KT area, quantitative KT imaging challenges light microscopy at its technical limits. Consequently, the absolute differences in FRET ratios between different constructs and conditions were rather small compared to the overall data spread within each construct and condition. In addition, YPet bleedthrough might partially mask small differences in FRET by contributing ∼25 AU to the FRET ratio (fig. 3.12 and 3.13), which accounts for ∼50 % of the total value.

For the thus far presented statistical analysis of tension measurements, data from multiple experimental days were pooled and analyzed as a single cohort. Though being simple and straight forward, this procedure raises two questions: First, are the total differences observed after data pooling indeed general effects or rather caused by individual days showing extreme values; and second, are the presented effects relevant, considering the small differences between cell lines and conditions and the much larger spread within each cell line and condition.

To answer these questions, I explored additional data analysis approaches. First, bootstrapping was performed to analyze whether the observed differences are a general property of the entire data set or caused by only a few but extreme values. Second, the calculation of confidence intervals (CIs) for each individual replication of the experiment allowed the analysis of day-to-day variability and identification of confounding factors. Third, the transformation of raw differences in FRET ratios to a normalized effect allowed an objective and dimensionless classification of the effect. And finally, the determination of the effect of nocodazole during each individual repetition of the experiment allowed the conduction of meta-analysis as an alternative method to combine data across experimental days.

3.10.1 Bootstrap analysis

Bootstrap analysis is a resampling method that can be used to analyze if an observed effect is a coherent property of the complete data set, or if only few individual but extreme observations are responsible for the overall effect. To this end, bootstrap samples were generated from the original data by random sampling with replacement and the size of the bootstrap sample was defined by the size of the original data set. Samples pairs were drawn for metaphase and nocodazole treated cells and compared using the Mann-Whitney U test, as already done previously for analysis of the original data. A schematic example of the complete process is shown in fig. 3.22.

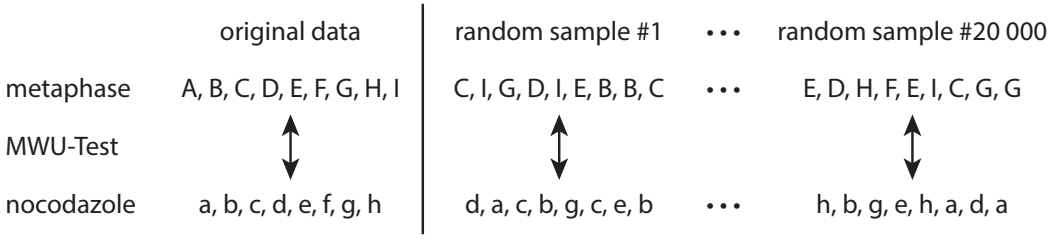

Figure 3.22: Schematic illustration of bootstrap analysis. The original data set in this schematic example contains 9 metaphase cells and 8 nocodazole treated cells; FRET ratios of individual cells are symbolized by letters. The Mann-Whitney *U* (MWU) test was used to analyze differences between these data sets. For bootstrap analysis, random samples with replacement (i.e. one value from the original data can be represented multiple times in the bootstrap sample) of the same size as the original data set were generated. These samples were then analyzed with the same test as used for the original data. The whole process was repeated 20 000 times to obtain a representative distribution of Z-scores for further analysis.

As p-values lack information about the direction of an effect, histograms of Z-scores from a bootstrap analysis with 20 000 cycles per cell line and condition are shown in figure 3.23. Negative Z-scores indicate that metaphase cells had lower FRET ratios than nocodazole treated cells and vice versa; a score of $|Z| \geq 1.96$ is equivalent to a p-value ≤ 0.05 and indicates statistical significance. If an effect seen in the original data was caused by only a few but extreme values, histograms of Z-values would be skewed, since only a subset of bootstrap samples contains these extreme values; furthermore, the Z-value from the original data maps to the shoulder region instead of overlapping with the histogram peak.

Z-score histograms for all cell lines and conditions are normally distributed (Lilliefors test) and of comparable width and standard deviation (fig. 3.23). Furthermore, Z-values from the original data map onto the peak of the respective histogram. Table 3.1 summarizes the results of the bootstrap analysis and provides information on the percentage of bootstrap samples that fall into the the respective p-value strata.

Together, the results of the bootstrap analysis indicate that the effects described in the previous sections are supported by the mass of each data set and not caused by few but extreme outliers.

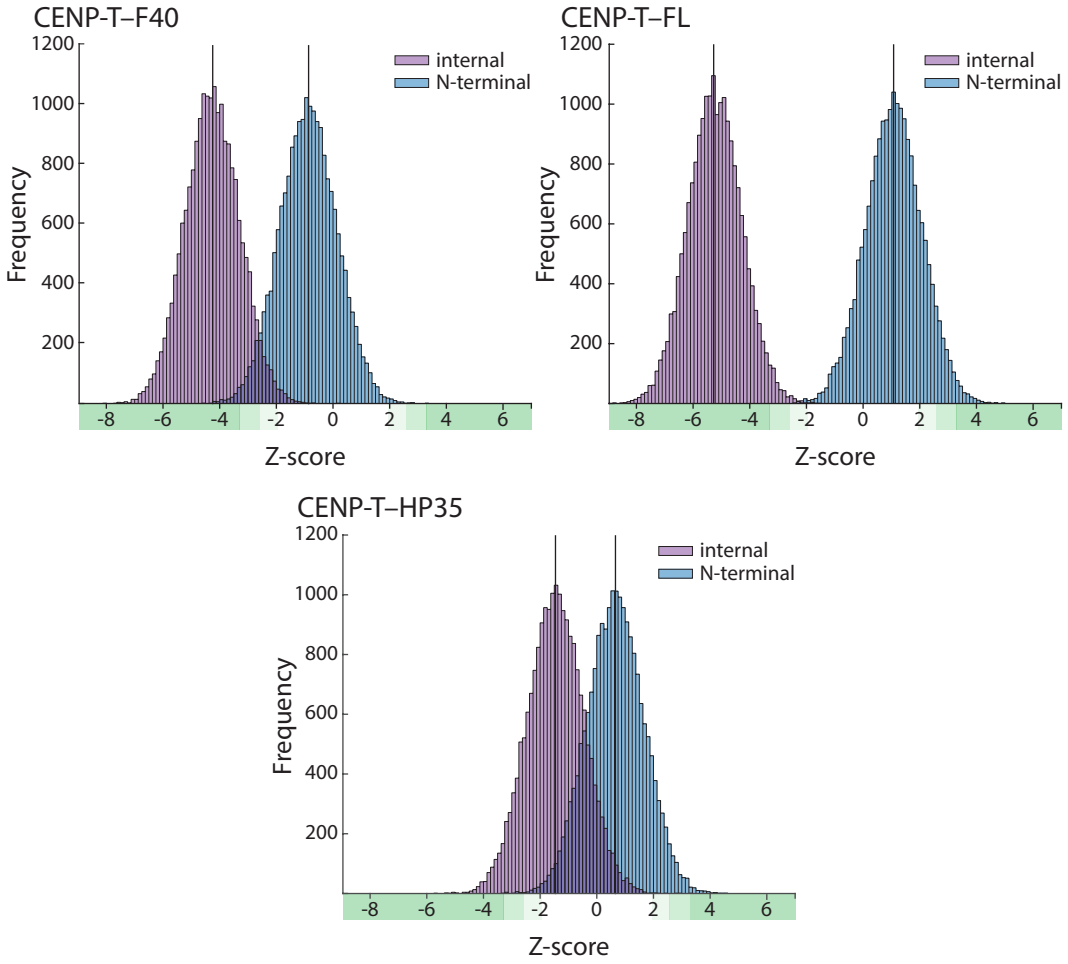

Figure 3.23: Bootstrap analysis of CENP-T biosensors. Bootstrap analysis was performed with 20 000 samples that were generated from the original data by random sampling with replacement (also see fig. 3.22). Results are shown as Z-scores, since p-values lack information about the direction of the effect. $|Z| \geq 1.960$ corresponds to $p \leq 0.05$, $|Z| \leq 2.576$ to $p \leq 0.01$, and $|Z| \leq 3.291$ to $p \leq 0.001$. Negative Z-score indicate that metaphase cells had lower FRET ratios than nocodazole treated cells. Vertical lines indicate experimentally obtained Z-scores.

Table 3.1: Results summary of bootstrap analysis

	neg. Z-values in %[a]				pos. Z-values in %[a]			bootstrap		exp. data
	***	**	*	n.s.	*	**	***	mean Z	SD	actual Z
F40(int)	84.4	11.6	3.1	0.8	–	–	–	-4.259	0.956	-4.246
F40(N)	0.7	3.6	9.4	86.0	0.2	–	–	-0.867	1.000	-0.862
FL(int)	98.0	1.8	0.2	–	–	–	–	-5.263	0.951	-5.274
FL(N)	–	–	0.2	81.2	12.0	5.4	1.2	1.069	0.997	1.077
HP35(int)	3.3	9.9	17.5	69.3	–	–	–	-1.459	0.995	-1.456
HP35(N)	–	0.1	0.3	89.8	7.1	2.4	0.4	0.659	1.000	0.659

[a] Numbers shown are percentage of Z-scores/p-values obtained by bootstrap analysis that fall into the indicated category. Stratification of Z-scores/p-values according to * = $p \leq 0.05$ or $Z \geq |1.960|$, ** = $p \leq 0.01$ or $Z \geq |2.576|$ and *** $p \leq 0.001$ or $Z \geq |3.291|$.

3.10.2 Confidence Intervals

To compare how uniform measurements were between individual experimental days, 95 % CIs for the mean FRET ratio per cell line, day and condition were calculated based on the T-distribution (see section 2.6.3 for details). In brief, the 95 % CI defines the interval that covers the true mean (which could be determined only with a certain error due to within-sample variations and measurement errors) with a certainty of 95 %.

Assuming that FRET ratios were only determined by the respective cell line and treatment, each repetition of the experiment should be measuring the same true mean; however, with an individual sampling error. As CIs already account for these sampling errors by their width, 95 out of 100 CIs that have been calculated to the 95 % level should cover a common value, which marks the true mean.

The data presented in figure 3.24 show that the variance between individual days is much larger than expected, if FRET ratios were only determined by cell line and treatment. This indicates that the total FRET ratio of an individual experiment is determined by additional confounding factors that varied between individual repetitions.

3.10.3 Effect size calculation and meta-analysis

3.10.3.1 Effect size

Calculation of 95 % CIs revealed that additional factors besides cell line and treatment had an impact on FRET ratios. One of these so called confounding factors is clearly connected to the experimental day, as some days showed generally elevated or reduced absolute FRET ratios across all constructs. As the magnitude of these day-to-day variation sometimes exceeded the relative within-day differences between cell lines and treatments,

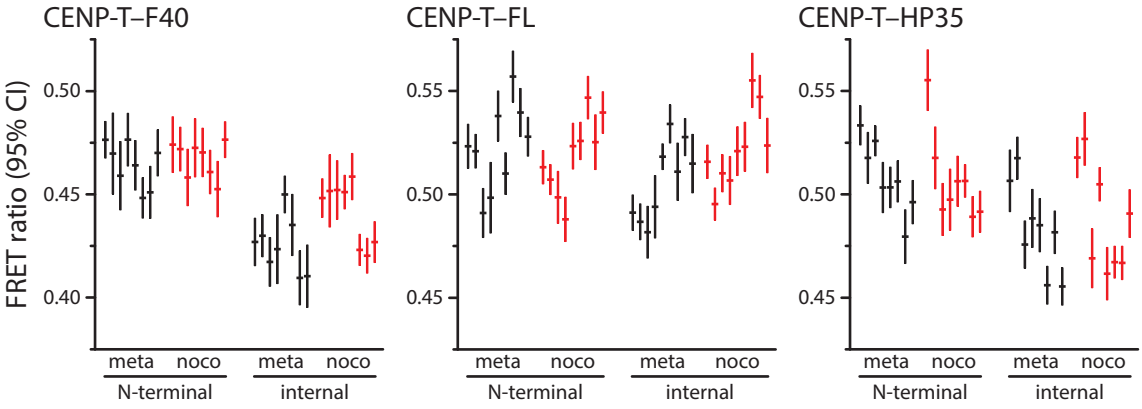

Figure 3.24: 95 % confidence intervals of individual experimental days. Each vertical line represents the 95 % CI for the mean FRET ratio of an individual experiment, horizontal lines mark the point estimate. CIs were calculated based on the T-distribution as described in section 2.6.3.

simple pooling of all cells irrespectively of the experimental day introduces a high variance within the pooled data set and thereby hampers statistical analysis.

These total FRET shifts likely depend on the state of the microscope; however, as this study is not interested in absolute FRET efficiencies but in FRET-shift upon nocodazole treatment, the observed offset can be treated as systematic error, which is constant within one day but varies between days. One way to exclude such systematic errors from data analysis is to determine the standardized mean difference or effect size, called Hedges' g (equations are provided in sec. 2.6.4). Similar to a correlation coefficient, Hedges' g is a dimensionless number quantifying the effect of a certain treatment in comparison to a control group; in this case, the effect of nocodazole treatment in comparison to untreated metaphase cells. It has to be noted that the effect size itself already refers to the difference between treatment group and control, thus reducing the number of "data sets" that is shown when reporting the data by the factor of two (as compared to previous graphs, in which treatment group and control group were shown as two separate data sets next to each other). Effect sizes together with 95 % CIs for each individual experimental day and biosensor and shown in tables 3.2, 3.3, and 3.4.
Despite compensating for systematic errors that depend on the experimental day, transforming raw data to the dimension free effect size g has the additional advantage of yielding information about the effect strength, which is commonly categorized as small ($0 < |g| \leq 0.2$), medium ($0.2 < |g| \leq 0.5$), and large ($|g| > 0.5$).

3.10.3.2 Meta analysis

After transforming the data from all individual experiments to a common, dimensionless scale, meta analysis was performed to determine the common effect across all experimental days. The general concept of meta analysis is the calculation of a mean effect size, which is not simply the arithmetic but a weighted mean of all individual effect sizes. Depending on the experimental setup and the underlying theoretical model, either a fixed effects, or a random effects model can be chosen [Borenstein et al., 2010].

The fixed effects model is based on the assumption that the true effect was the same in all studies and variations between the outcome of individual studies were solely caused by a random measuring error (called within-study variance). This is usually the case if all experiments have been performed under exactly identical conditions from the technical side and no biological variation between individual days has to be expected. In this case, the weight of an individual study is determined by the inverse within-study variance of that same study. Consequently, studies with low variance (and high accuracy) contribute stronger towards the final mean effect than those with a high variance (and low accuracy).

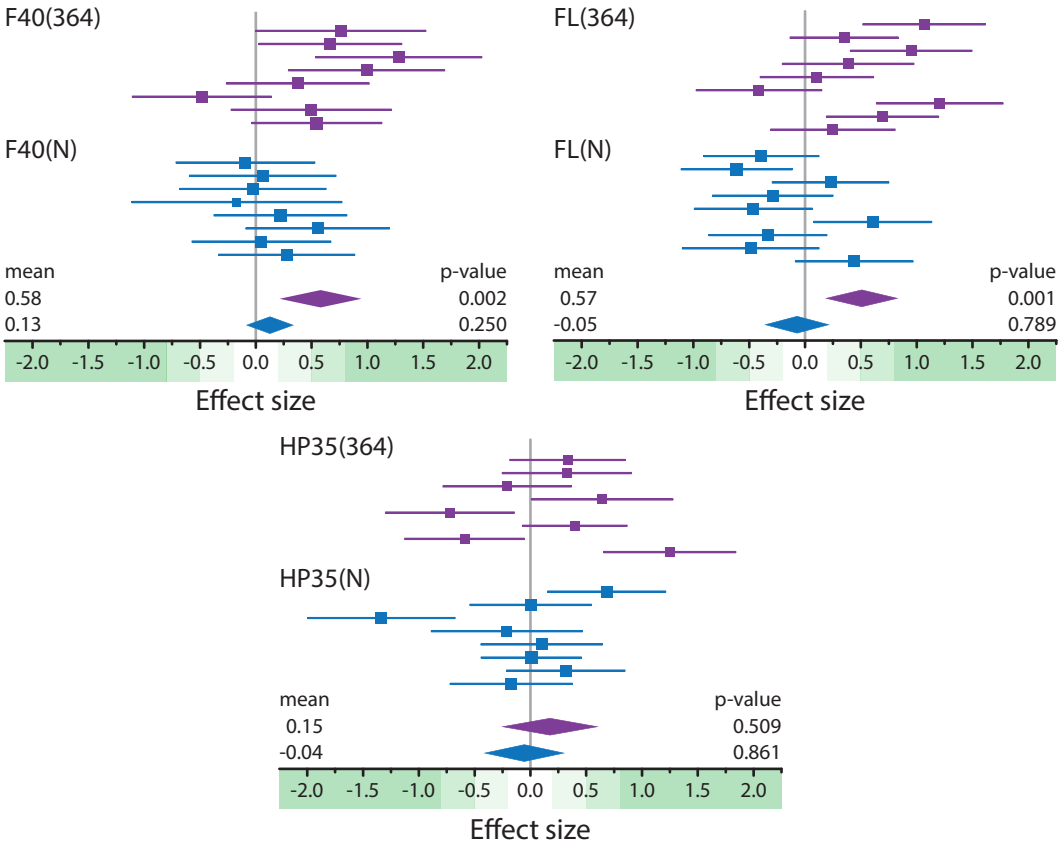

Figure 3.25: Random-effects model meta analysis. Forest plots showing the results of a meta-analysis calculated with the random effects model. Lines represent 95 % CIs for the effect that nocodazole treatment had on a particular experimental day and cell line. Point estimates for individual days are marked by squares, the area of each square is proportional to the weight that was assigned to the respective experiment during meta-analysis. Diamonds represent combined 95 % CIs. Effect sizes E are categorized as small ($0 < |E| \leq 0.2$), medium ($0.2 < |E| \leq 0.5$), large ($0.5 < |E| \leq 0.8$), very large ($0.8 < |E| \leq 1.2$), and huge ($|E| > 1.2$).

The random effects model, on the contrary, assumes that the true effect (that was measured with a certain error) was always similar, but not identical across studies or experimental days. This is, for example, the case if different batches of a chemical cannot be assumed to have exactly the same efficacy or if the performance of a measuring device slightly varies over time. To account for this additional source of variation, a between-study variance is calculated and the total variance of an individual study is defined as the sum of within- and between-study variance; studies are then weighted according to the inverse total variance. As consequence, individual weights get more balanced on the cost of an increased total variance (and therefore wider CI) of the combined effect.

Notably, if the between-study variance within a random-effects analysis is very low, results closely approximate those of the fixed-effects model as the total variance is mainly determined by the within-study variance. Additionally, in cases where the between-study

variance turns out to be trivial (i.e. less than expected under the hypothesis of only random variations between studies), the random effects model will reduce to the fixed effects model.

Even though the experimental protocol for tension sensor experiments was identical between individual days (thus meeting the key criterion for choosing the fixed-effects model), small variations in inhibitor concentration due to pipetting errors or partial degradation caused during storage and repeated freeze-thaw-cycles and variations in the microscope performance could not be excluded. Since both models will provide identical results if the between-study variance should indeed be negligible, I decided to apply the random-effects model on the cost of wider CIs of the combined effect. Computational details are provided in sec. 2.6.5 and were performed according to Borenstein et al. [2007].

Figure 3.25 shows 95 % CIs of effect sizes for each individual biosensor and experiment as well as overall effects obtained by random effects meta-analysis; tables 3.2, 3.3 and 3.4 provide additional information about sample sizes, individual variances and total weights within meta-analysis.

Together, the results obtained from the meta-analysis match with those seen after simple pooling by revealing that the two sensors for the low force regime, F40 and FL, report CENP-T forces during metaphase, while these forces are not sufficient to unfold the HP35 peptide. Furthermore, despite the small differences in absolute FRET ratios, effect size calculation proved that the observed effects are considered as "large", demonstrating their relevance.

Table 3.2: Meta-analysis of CENP-T–F40 sensors

Experiment	n[a]	Variance	Weight [%]	Effect	95 % CI
F40(int)–1	21/23	0.097	12.65	0.883	[0.243; 1.524]
F40(int)–2	21/21	0.097	12.64	0.667	[0.026; 1.309]
F40(int)–3	19/18	0.126	11.45	1.280	[0.535; 2.025]
F40(int)–4	19/20	0.111	12.03	0.992	[0.292; 1.693]
F40(int)–5	20/22	0.094	12.79	0.376	[-0.264; 1.017]
F40(int)–6	19/28	0.088	13.06	-0.483	[-1.106; 0.139]
F40(int)–7	16/19	0.113	11.93	0.494	[-0.224; 1.212]
F40(int)–8	21/31	0.080	13.44	0.546	[-0.038; 1.130]
F40(int)–overall	*156/182*	*0.035*	*100*	*0.579*	[*0.212; 0.947*][b]
F40(N)–1	23/20	0.090	13.39	-0.093	[-0.716; 0.530]
F40(N)–2	20/19	0.099	12.26	0.062	[-0.595; 0.719]
F40(N)–3	20/19	0.098	12.26	-0.026	[-0.683; 0.630]
F40(N)–4	9/15	0.166	7.26	-0.169	[-1.110; 0.771]
F40(N)–5	24/23	0.083	14.58	0.220	[-0.375; 0.816]
F40(N)–6	21/20	0.098	12.37	0.554	[-0.090; 1.197]
F40(N)–7	20/24	0.088	13.66	0.050	[-0.572; 0.673]
F40(N)–8	20/27	0.085	14.22	0.276	[-0.334; 0.887]
F40(N)–overall	*157/167*	*0.012*	*100*	*0.126*	[*-0.089; 0.342*][b]

[a] Numbers given in the order metaphase/nocodazole
[b] p-values: F40(int) = 0.002 (**), F40(N) = 0.250 (n.s.)

Table 3.3: Meta-analysis of CENP-T–FL sensors

Experiment	n[a]	Variance	Weight [%]	Effect	95 % CI
FL(int)–1	31/31	0.072	11.06	1.066	[0.517; 1.614]
FL(int)–2	35/35	0.057	11.77	0.378	[-0.106; 0.863]
FL(int)–3	31/30	0.071	11.09	0.960	[0.414; 1.505]
FL(int)–4	20/33	0.088	10.42	0.835	[0.215; 1.455]
FL(int)–5	33/30	0.067	11.27	0.219	[-0.310; 0.748]
FL(int)–6	27/26	0.075	10.94	-0.412	[-0.975; 0.151]
FL(int)–7	30/30	0.077	10.86	1.196	[0.629; 1.763]
FL(int)–8	36/32	0.061	11.56	0.694	[0.192; 1.196]
FL(int)–9	25/29	0.073	11.03	0.249	[-0.308; 0.807]
FL(int)–overall	*268/276*	*0.0279*	*100*	*0.573*	[*0.246; 0.900*][b]
FL(N)–1	29/34	0.064	11.30	-0.410	[-0.926; 0.107]
FL(N)–2	31/39	0.060	11.46	-0.681	[-1.181;-0.181]
FL(N)–3	31/29	0.065	11.22	0.229	[-0.293; 0.752]
FL(N)–4	26/32	0.074	10.88	0.679	[0.119; 1.239]
FL(N)–5	30/30	0.065	11.23	-0.413	[-0.935; 0.110]
FL(N)–6	30/31	0.067	11.16	0.605	[0.076; 1.134]
FL(N)–7	30/29	0.067	11.16	-0.335	[-0.865; 0.194]
FL(N)–8	22/24	0.087	10.40	-0.488	[-1.100; 0.125]
FL(N)–9	30/30	0.066	11.19	0.404	[-0.123; 0.931]
FL(N)–overall	*259/278*	*0.030*	*100*	*-0.046*	[*-0.387; 0.294*][b]

[a] Numbers given in the order metaphase/nocodazole
[b] p-values: FL(int) , 0.001 (***), FL(N) = 0.789 (n.s.)

Table 3.4: Meta-analysis of CENP-T–HP35 sensors

Experiment	**n**[a]	**Variance**	**Weight** [%]	**Effect**	**95 % CI**
HP35(int)–1	29/33	0.064	12.88	0.333	[-0.186; 0.851]
HP35(int)–2	25/25	0.079	12.43	0.325	[-0.253; 0.904]
HP35(int)–3	25/25	0.078	12.44	-0.209	[-0.785; 0.368]
HP35(int)–4	21/23	0.093	12.01	0.644	[0.009; 1.278]
HP35(int)–5	25/28	0.078	12.43	-0.721	[-1.299;-0.143]
HP35(int)–6	28/30	0.068	12.77	0.193	[-0.340; 0.727]
HP35(int)–7	30/29	0.069	12.72	-0.590	[-1.127;-0.053]
HP35(int)–8	26/31	0.082	12.31	1.249	[0.658; 1.841]
HP35(int)–overall	*209/224*	*0.051*	*100*	*0.148*	[*-0.292; 0.589*][b]
HP35(N)–1	22/25	0.090	12.08	0.858	[0.249; 1.468]
HP35(N)–2	35/22	0.072	12.80	0.002	[-0.544; 0.547]
HP35(N)–3	23/24	0.101	11.70	-1.335	[-1.995;-0.675]
HP35(N)–4	20/17	0.105	11.58	-0.211	[-0.888; 0.467]
HP35(N)–5	26/30	0.070	12.89	0.100	[-0.444; 0.645]
HP35(N)–6	31/30	0.064	13.14	0.072	[-0.444; 0.588]
HP35(N)–7	28/31	0.067	13.01	0.317	[-0.214; 0.848]
HP35(N)–8	31/24	0.072	12.80	-0.172	[-0.720; 0.377]
HP35(N)–overall	*216/203*	*0.040*	*100*	*-0.035*	[*-0.425; 0.355*][b]

[a] Numbers given in the order metaphase/nocodazole
[b] p-values: HP35(int) = 0.509 (n.s.), HP35(N) = 0.861 (n.s.)

4 Discussion

4.1 Quantitative kinetochore imaging requires specifically adapted experimental design

4.1.1 Kinetochore forces are best quantified by ratiometric FRET

Several methods for the quantification of Förster resonance energy transfer (FRET) have been developed, each with their own advantages and disadvantages. Fluorescence-lifetime imaging microscopy (FLIM) has the power of directly providing FRET efficiencies and being independent of fluorophore concentrations. The major disadvantage of this method, however, is the high number of photons necessary for reliable fitting and lifetime calculation. Even in bright samples, a total recording time of 50 seconds is necessary to yield sufficient photon counts on our setup. Such exposure times are only possible if the sample neither moves, nor shows significant photobleaching during acquisition; dim and fast moving KTs as imaged in this study fulfill none of these criteria.

Besides FLIM-FRET, intensity based methods like sensitized emission or acceptor photobleaching also allow the determination of actual FRET efficiencies, but again require the acquisition of several images. In applications with fixed stoichiometry of donor and acceptor fluorophores, however, intensity based approaches can be reduced to ratiometric FRET. On systems that allow simultaneous recording of the donor and acceptor emission channels, FRET ratios can be quantified after a single round of donor excitation.

The FRET pair used in this study was made of the yellow and red fluorescent proteins YPet and mCherry. As alternatives, mCerulean3–YPet, a FRET pair commonly used in intensity based setups, was tested. With this FRET pair, however, automated KT thresholding was not possible, as KTs could not be reliably discriminated from autofluorescent vesicles in the mCerulean3 channel. I thus decided to maintain the YPet–mCherry fluorophore combination, which was well established in the lab and also used during calibration of the HP35 and HP35st TSMs.

4.1.2 The applied experimental design is robust against intermolecular FRET

FRET can not only occur between donor and acceptor fluorophore of a single TSM, but also between neighboring biosensors which is known as intermolecular FRET. Intermolecular FRET levels cannot be expected to be identical between internally and C- or N-terminally integrated TSMs, and direct FRET comparison between a biosensor and the zero-force control requires prior quantification of the respective intermolecular FRET levels. Such quantifications can be obtained by measuring FRET in cells that co-express donor- and acceptor-only constructs. In the case of KTs, however, the reliability of intermolecular FRET quantification by this method is questionable due to the low number of protein copies per KT and the therefore high stochastic variation between the number of incorporated donor- and acceptor-only constructs within each KT. Furthermore, it cannot be expected that both constructs would be expressed at exactly the same levels, making the reliability of such intermolecular FRET measurements even more questionable when overall copy numbers are very low.

As alternative approach, an experimental setup that does not rely on the direct comparison of internal and N-terminal biosensors (and is thus robust against variations of intermolecular FRET) was realized by the parallel analysis of cells in metaphase and after nocodazole treatment. At the applied concentration of 5 µM, nocodazole completely depolymerizes the mitotic spindle, thus creating an additional zero-force control for each individual biosensor (internal ones as well as N-terminal zero-force constructs). As the levels of intermolecular FRET predominantly depend on the location of the TSM within the targeted protein, intermolecular FRET can be expected to add a constant term towards the total FRET ratio at metaphase cells and nocodazole treated cells alike. Following this approach, metaphase cells of each cell line could be compared to nocodazole treated cells of the same cell line and the quantified parameter was the change in FRET ratio between both conditions within a single cell line.

Prior to conducting actual force analyses, it was confirmed that nocodazole alone does not affect donor fluorescence or image quantification by comparing the bleedthrough of DMSO and nocodazole treated donor-only cells (fig. 3.13).

4.2 Development of a new 3–5 pN tension sensor module

By the time this project was initiated, three calibrated TSMs were available at our lab. The F40 module is based on the flagelliform peptide and sensitive to forces ranging from 1–6 pico Newton (pN) [Grashoff et al., 2010]. The two sensors based on the villin headpiece, HP35 and HP35st, display highest sensitivity in the range of 6–8 and 9–11 pN, respectively

[Austen et al., 2015]. Based on *in vitro* experiments (discussed in sec. 1.5.2), forces across KT proteins were expected to be in the lower single pN range and I thus decided to use the F40 sensor in combination with HP35.

After analysis of these biosensors (discussed in sec. 4.5), it became evident that an additional biosensor with increased sensitivity $< 6\,\mathrm{pN}$ would be helpful to confirm the observations of the F40 sensor and learn more about CENP-T force transduction. As biosensors can be best compared when their structures are highly similar, five mutants of the HP35 peptide were tested for their potential as linker peptides. Cytosolic expression of the new TSMs, however, revealed that neither of the tested candidates was promising because they either did not fold efficiently, or were most likely not sufficiently destabilized in relation to the existing HP35 sensor (fig. 3.17).

Next, two alternative peptides were tested for their suitability as force sensitive linkers: a *de novo* designed FL fold domain and a Ca^{2+} insensitive EF-hand motive. Both linkers showed promising results when expressed cytosolically (fig. 3.18) and after integration into the well characterized focal adhesion protein talin (fig. 3.19). Due to its higher starting FRET and predicted dynamic range, the FL–TSM was selected for calibration by single-molecule force spectroscopy, which revealed a very narrow sensitivity profile with a mid-transition force of 4.2 pN (fig. 3.20). Calibration furthermore demonstrated that the new sensor was insensitive to forces $< 3\,\mathrm{pN}$, and showed an almost digital force response between 3 and 5 pN.

4.3 Ndc80 biosensors lacked biological functionality

Based on its prominent role as KT–MT force coupler and its elongated structure with distinct binding domains for MTs and inner KT proteins, the Ndc80 complex is one of the the most obvious targets for TS integration. Three putative biosensors were generated (fig. 3.1) and tested for functionality in HeLa cells. Despite the formation of morphologically normal spindles (fig. 3.2) and loss of the spindle assembly checkpoint protein Mad1 from KTs after chromosome congression (fig. 3.3), cells expressing the internal biosensor had significant problems to enter anaphase (fig. 3.4). Furthermore, several attempts to generate stable biosensor cell lines failed, while it was no problem to stably express fluorescently tagged histone H2B using the same retroviral system. All this indicated that the generated Ndc80 biosensors lacked full biological functionality and that their expression eventually caused cell death due to mitotic errors or sustained checkpoint activation.

A few years later, the successful integration of a TSM into Ndc80 of *S. cerevisiae* was published by Suzuki et al. [2016]. Their strain was viable despite homozygous expression of the biosensor from the endogenous locus, thus clearly demonstrating biological function-

ality of the generated construct. It has to be noted, however, that a total of six different integration sites was tested, and the reported strain was the only one viable (Aussie Suzuki, personal communication, December 6, 2016), which confirms that Hec1/Ndc80 generally does not tolerate disturbance by tension sensor integration at many regions of the protein.

The report of a viable biosensor in yeast Ndc80/Hec1 raised the question whether the homologous integration site in human Hec1 was also viable. Nevertheless, I decided against resuming the Hec1 project for two reasons. First, a clear and easy system for evaluating Hec1 functionality in mammalian cells was still not available to me. And more importantly, the reported integration site resides within the coiled-coil domain of Ndc80/Hec1, making it in my opinion questionable whether the change in FRET observed by Suzuki et al. is solely caused by increased fluorophore separation, or rather a consequence of rotational confinement coinciding with a change in FRET towards the expected effect.

4.4 CENP-T biosensors compensate loss of wild type CENP-T

The Ndc80 complex is anchored to centromeric DNA either via the KMN network and CENP-C, or directly via CENP-T (fig. 1.7). CENP-C and CENP-T each comprise a globular head domain and an elongated, presumably disordered tail, making both proteins suitable candidates for TSM integration. Within KTs of HeLa cells, however, only about 40 % of all CENP-C molecules recruit a KMN network and thus are potentially under force, while each human CENP-T recruits ∼2 Ndc80 complexes [Suzuki et al., 2015a]. I therefore decided to target CENP-T for the generation of KT biosensors.

As data can be quantified more precisely from a pure biosensor population, experiments should best be performed on a CENP-T knockout background. Due to the essential role of CENP-T, however, a direct knockout without replacement leads to cell death. The lab of Tatsuo Fukagawa addressed this issue by generation of a tetracycline inducible CENP-T knockout in DT40 cells, a cell line which originated from a chicken B-cell lymphoma [Hori et al., 2008]. For the generation of biosensor cell lines, CENP-T$^{\text{tet-off}}$ cells were stably transfected with CENP-T biosensor cDNA. Exposure to tetracycline or the variant doxycycline then eliminated expression of wtCENP-T, allowing to directly test the biological functionality of the biosensor as well as its analysis in the absence of wtCENP-T.

While CENP-T$^{\text{tet-off}}$ cells died within a few days after doxycycline was administered (fig. 3.5), all CENP-T biosensor expressing cell lines were viable despite long term exposure to doxycycline and grew at the same rates as cells expressing wtCENP-T (fig. 3.8, 3.16 B, and 3.21 B). Furthermore, the biosensors localized to kinetochores and the cells formed morphologically normal spindles (fig. 3.9, 3.16 A, and 3.21 A), demonstrating biological functionality of CENP-T biosensors.

4.5 CENP-T's upper force limit is above 3 but below 6 pN

4.5.1 CENP-T(364) biosensors are functional and report low pN forces

Due to its sensitivity already to very low forces and relatively broad force spectrum, F40 was the first TSM that was integrated into CENP-T. As no structural data of the CENP-T tail were available, insertion sites were chosen on the basis of (1) low conservation in BLAST analysis, (2) structural prediction, and (3) local aa composition. Based on these information, the TSM was integrated at two alternative sites withing the CENP-T tail, namely after aa 282 and 364. Furthermore, an N-terminal zero force control was generated.

Initial FRET analysis of the two internal biosensors and the N-terminal control showed a nocodazole dependent FRET increase when the F40 module was placed after aa 364, but no statistically significant difference could be observed for integration site 282 and the N-terminal control. As this first set of experiments has been performed at room temperature, it was repeated at a similar setup which could be equilibrated to 37 °C (this setup was also used for all subsequent experiments). This second, completely independent data set confirmed the observations of the first data set.

At this point, there were two possible explanations for the observed results: Either, none of the sensors reported force and the decreased FRET observed for metaphase CENP-T–F40(364) cells was caused by an artifact. Or alternatively, the TSM at aa 364 indeed showed reduced FRET due to force-dependent linker elongation, while at the same time similar forces could not be measured at position 282.

To test which of the two above mentioned hypotheses holds true, the F40 TSM was replaced by the stiffer HP35 module. As both biosensors are highly similar except for the 35 to 40 aa long linker peptide, any unspecific artifacts are likely to occur with both TSMs. However, no significant FRET decrease could be detected in metaphase cells expressing an internal HP35 biosensors at aa 364, thus supporting the hypothesis that the decreased FRET observed with the F40 module is indeed due to forces that are sufficient to elongate the F40 module, but not high enough to cause a significant FRET decrease with the stiffer HP35 module.

To further test this hypothesis and, if true, better quantify the forces experienced by CENP-T, a new TSM based on the FL linker peptide was generated. Single-molecule calibration of this TSM revealed a very sharp sensitivity profile ranging from 3–5 pN. The results obtained after integration of this new module into CENP-T further supported the hypothesis that the protein indeed experiences forces at aa 364, which, however, do not exceed 6 pN.

This raises the question why only one of the internal sensors was functional. Without comprehensive knowledge of the CENP-T tail structure and all its interaction partners,

it can only be speculated. However, multiple criteria have to be met to get a functional biosensor and violation of any of these can make the sensor non-functional. The three most important prerequisites are that (1) forces along the integration site have to act in a direction parallel to the force sensitive linker, (2) the local environment and associated protein complexes must not form crosslinks that restrain the linker from elongating or share the load, and (3) the fluorophores must be able to freely rotate, as FRET is also determined by the relative angle between both fluorophores. Until now, no protein complex has been found to bind to the CENP-T tail in the vicinity of aa 282; however, is has to be noted that recruitment of the KMN network to human CENP-T has also been discovered only recently, after it had been commonly accepted for many years that CENP-T acts independently of the KMN network [Rago et al., 2015].

4.5.2 Combination of three tension sensors allows the estimation of a lower and an upper force limit

Like a macroscopic spring scale, each individual TSM covers only a limited force range, making it insensitive to forces below that range, while forces exceeding the upper limit will not be resolved. This behavior has important implications for data interpretation, in particular of ensemble measurements. First, if a tension sensors does not report force, it could also be that forces are present but below the lower sensitivity threshold of the respective sensor. In case of the F40 sensor, however, this is unlikely, as this module is sensitive to forces as low as a single pN. And second, the direct translation of an average FRET efficiency into force per molecule is not always possible, in particular if the distribution of forces that individual proteins experience is broad. In these cases, the average force is usually underestimated due to a combination of forces too low to be detected, and forces that exceeded the sensor's sensitivity and thus cannot be resolved anymore.

The combination of several TSMs covering different force regimes each, however, allows the estimation of upper and lower force limits. In the context of this thesis, the application of the FL sensor demonstrated that forces along the CENP-T tail can reach at least 3 pN, since this module is insensitive to lower forces. At the same time, however, CENP-T forces do not exceed 6 pN, as the HP35 module was largely insensitive to CENP-T forces. The F40 sensor supports these conclusions by providing additional evidence that the FRET reduction seen with the FL TSM is indeed due to force dependent linker elongation.

4.6 Statistical analysis of tension measurements

Pooled statistics and bootstrap analysis

The results obtained from three different TSMs complement each other to support a common hypothesis. The FRET changes observed for each particular sensor, however, are rather small on absolute scale as well as in relation to the variance observed for individual measurements of a particular cell line and condition. This raises the importance to thoroughly test whether the force dependent FRET reductions are statistically significant and biologically relevant.

To reduce the risk of data over-interpretation, statistical analysis was conducted following conservative approaches. Besides applying the nonparametric Mann-Whitney U test on pooled data, bootstrap analysis was performed to exclude the possibility that the observed overall differences were caused by only a few but extreme values. Z-score histograms of 20 000 bootstrap samples, however, showed uniform distributions and the experimental Z-score from the actual data mapped to the histogram peaks (fig. 3.23), demonstrating that the differences observed with pooled data were inherent characteristics of the entire data set.

Confidence intervals

Even though bootstrap analysis confirmed uniform effects when averaging across all experimental days, the calculation of 95 % confidence intervals revealed high variances between the absolute FRET ratios of individual experimental days. At the same time, the relative differences between distinct constructs and treatments within individual experimental days were comparatively constant (fig. 3.24). As KTs are very small and dim, low signal-to-noise ratios constituted a particular experimental challenge and small fluctuations in instrument performance entailed quite significant effects on FRET ratios. Under such conditions, simple pooling of data from different experimental days can be problematic since large and systematic between-day variances may partially mask smaller between-condition variances. An alternative approach for combining data across several experimental days which is robust against such systematic day-to-day variances is provided by meta-analysis.

Meta-analysis

Meta-analysis is a statistical tool for the quantification of a common effect that has been measured within individual studies; however, each time with a certain error. Depending on the expected source of errors, either a fixed- or random-effects model can be applied. The fixed-effects model assumes that each study attempted to measure the very same common effect and variations are solely caused by measurement errors. The random-effects model, on the other hand, assumes a common trend between all studies; however, the specific effect

size can be more pronounced in some studies than in others. In addition, it has to be mentioned that the more complex random-effects model reduces to the simpler fixed-effects model in cases where the in-between study variance turns out to be trivial compared to the within-study variance. It is therefore always safe to apply the random-effects model, as done in this study.

Meta-analysis revealed that none of the N-terminal zero-force controls shows significant changes in FRET upon nocodazole treatment. Regarding the internal biosensors, the F40– and FL–TSMs showed a significantly decreased FRET ratio during metaphase as compared to nocodazole treated cells, but this effect could not be seen for the stiffer HP35 module (fig. 3.25). The results of the meta-analysis are thus consistent with the statistical analysis of pooled data.

An additional advantage of meta-analysis is the conversion of raw data into a common effect size, which revealed that – despite the small absolute differences observed on the level of FRET ratios – the effect of nocodazole treatment on F40 and FL biosensors is classified as "large". (On the effect scale, nocodazole treatment of HP35 biosensors also had a "small" effect, but the p-value of 0.509 indicates that this effect is far from being significant.)

Intuitively, it is surprising that the small differences observed in the raw data gave raise to large effects. It has to be considered, however, that YPet bleedthrough alone contributes about half of the total raw FRET ratio of metaphase and nocodazole treated cells alike. As the effect size is calculated on the basis of the relative difference of two values in relation to the data spread, such constant addends have no influence on the effect scale.

4.7 The results of this study in the light of existing literature

Ye et al. [2016] recently published a KT force sensor in *D. melanogaster* S2 cells by targeting CENP-C, which is the only known connector of the outer KT and the CCAN in this cell type (see sec. 1.2.3.3). Using the F40 TSM, the authors calculated an average CENP-C force of ∼1.2–1.4 pN. This value is two to three times lower than the value of at least 3 pN reported in this thesis, but besides the different cell type and target protein, two conceptual differences between their study and this thesis have to be pointed out. First, Ye et al. calculated an average force, whereas this study argues that at least some molecules must experience forces > 3 pN. And second, Ye et al. performed their experiments in a wild type background, which potentially underestimates forces due to the coexpression of the biosensor and wtCENP-C.

On first glance, reporting an average force per molecule might appear more informative than the statement that a least some molecules must be under forces higher than a cer-

tain threshold. It has to be noted, however, that movements due to thermal fluctuations alone can result in mechanical noise of ∼1 pN (Alexander Mehlich, personal communication, 16.9.2017). Two hypotheses for how forces of on average ∼1 pN can yet generate a mechanobiological effect can be postulated: Either, many molecules are exposed to a low but directed force simultaneously and exert the effect through their cooperative action. Or alternatively, a few molecules bear forces significantly higher than the calculated average, while many other molecules are not actively engaged in force transduction at all. Potential causes of such non-uniform distributions might be that poleward and antipoleward moving KTs do not simultaneously experience force, or that at any give moment, not all molecules which localize to KTs actually establish connections to MTs. The latter scenario is particularly likely when biosensors are expressed on top of endogenous protein or at levels higher than endogenous expression.

In vitro experiments showed that purified yeast Ndc80 alone can support forces up to 3 pN [Powers et al., 2009]. Furthermore, isolated yeast KT particles supported up to 11 pN and showed a catch-bond behavior for forces in range of 1–5 pN [Akiyoshi et al., 2010]. In light of these *in vitro* data, CENP-T forces of 3–6 pN as measured in this study are reasonable.

4.8 Fraction of actively engaged molecules

Inspired by the previous paragraph, it would be interesting to determine the fractions of opened and closed FL biosensors within a cell. In fact, a manuscript of our lab presenting a method for exactly this kind of analysis of FL biosensors has just been accepted for publication [Ringer et al., 2017b]. The method was established for the focal adhesion molecule talin and is based on a biexponential fitting procedure of FLIM data. As discussed in 4.1.1, FLIM analysis of KTs appeared to be out of reach for many years, but this recently changed with the publication of a protocol by Yoo and Needleman [2016]. The authors used Bayesian analysis with a reduced number of free parameters to perform FLIM-FRET measurements at KTs. Even though Yoo et al. thus far used an Aurora B phosphorylation sensor [Fuller et al., 2008] which likely localizes to KTs at higher copy numbers than endogenous centromere proteins, it will hopefully become possible in the future to combine their method with ours, finally allowing to determine the opened and closed fractions of FL-based KT biosensors.

Until then, only indirect hints allow some speculation about the open fraction of KT biosensors. As shown in fig. 3.21 D, the total relative difference between FRET ratios from metaphase cells vs. nocodazole treated cells is only a little above 3 %. As the FL–TSM shows an almost digital behavior of being either fully closed or fully opened, four factors can theoretically explain why the FRET ratios differ only so little between force and no-force

conditions. These four factors are (1) residual intramolecular FRET even if the sensor is open, (2) high level of donor bleedthrough, (3) intermolecular FRET, and (4) a low fraction of open sensors. Calibration of the new FL module revealed a contour length increase of 25–30 nm between the closed and the open state; accordingly, FRET rates drop to zero if the peptide is unfolded [Ringer et al., 2017b, fig. 1]. Further, the contribution of YPet bleedthrough to the absolute FRET ratio was quantified to be ∼50 % of the total FRET ratio (fig. 3.12 and 3.13). And finally, a study looking at the yeast KT found only low levels of intermolecular FRET between KT proteins [Aravamudhan et al., 2015]. It hast to be noted, of course, that the results obtained from yeast cannot be directly transferred to the chicken CENP-T biosensors used in this thesis, but it indicates that intermolecular FRET is unlikely to be a major contributor to the total FRET ratio measured with our sensors. Thus, neither insufficient length increase of the FL biosensor, nor YPet bleedthrough or extremely high levels of intermolecular FRET are likely to be the main reason for the small difference in FRET ratios and it can be speculated that only a small fraction of all CENP-T biosensors experiences forces > 3 pN.

4.9 Direct comparison of metaphase vs. anaphase forces

One of the most intriguing applications of KT tension sensors would be the direct comparison of forces between metaphase and anaphase. Such an analysis was indeed intended but had to be stopped due to experimental difficulties. Within the first minute after anaphase onset, KTs formed two clusters that were much brighter than individual KTs. The differences in brightness were such pronounced that the limited dynamic range of the detectors did not allow settings producing images of metaphase KTs bright enough for quantification, and at the same time not leading to detector saturation when imaging KT clusters during anaphase. This hurdle could theoretically be overcome by imaging exclusively cells within the first minute of anaphase and therefore before KT clustering was observed. Imaging an amount of cells that is sufficient for statistical analysis, however, was experimentally not feasible in a reasonable amount of time, as the probability of finding a cell exactly within the crucial moment is very low.

4.10 Concluding remarks and future perspectives

Two main challenges accompanied this project throughout all phases. The first one was set by the size and nature of KTs themselves, which are projected as almost diffraction limited spots that contain no more than two or three dozens of CENP-T molecules. The second challenge was the biological system in which this study was carried out.

Initial experiments in HeLa cells had pointed out the importance of functionality tests that reach beyond correct protein localization and the loss of individual spindle assembly checkpoint markers. The conditional DT40 CENP-T knockout cell line was thus a welcome tool to test protein functionality; furthermore, it allowed to perform measurements in the absence of wtCENP-T. Chicken cells, however, are rarely used as model organism and commercial antibodies that bind chicken isoforms are usually not available. This increased, for example, the hurdles for small interfering RNA (siRNA) screenings to test how loss of certain KT components effects CENP-T force transduction.

Since the initialization of this project, CRISPR/Cas started a remarkable procession and even homozygous integration of a TSM directly into the genomic locus of a more commonly used model organism came into reach. In fact, targeting constructs for TSM integration into mouse CENP-T have already been cloned.

Difficulties that arise from low fluorescent intensities will be harder to tackle. However, a change of model organism might be beneficial also in this respect, since protein copy numbers per KT seem to be higher in HeLa cells (and thus potentially in other mammalian cell types as well) as compared to DT40 cells [Johnston et al., 2010, Suzuki et al., 2015a].

FRET quantification by the ratiometric method had the advantages of being very fast and not requiring the acquisition of multiple images of a fast bleaching sample. The drawbacks of this method, however, are that no actual FRET efficiencies can be obtained and that small differences may be masked by the constant level of bleedthrough contained within the FRET ratio. While other intensity based methods like sensitized emission and acceptor photobleach generally allow the calculation of FRET efficiencies, such quantifications require complicated correction and normalization procedures, again limiting their accuracy. FLIM-FRET, the gold standard for quantitative FRET experiments, was considered out of reach for years, but this recently changed with the protocol published by Yoo and Needleman [2016].

Bibliography

Abad, M. A., Zou, J., Medina-Pritchard, B., Nigg, E. A., Rappsilber, J., Santamaria, A., and Jeyaprakash, A. A. (2016). Ska3 ensures timely mitotic progression by interacting directly with microtubules and ska1 microtubule binding domain. *Scientific Reports*, 6:34042.

Akiyoshi, B., Sarangapani, K. K., Powers, A. F., Nelson, C. R., Reichow, S. L., Arellano-Santoyo, H., Gonen, T., Ranish, J. A., Asbury, C. L., and Biggins, S. (2010). Tension directly stabilizes reconstituted kinetochore-microtubule attachments. *Nature*, 468(7323):576–579.

Alberts, B., Johnson, A., Lewis, J., Raff, M., Roberts, K., and Walter, P. (2007). *Molecular Biology of the Cell, 5th Edition*. Garland Science.

Alushin, G. M., Ramey, V. H., Pasqualato, S., Ball, D. A., Grigorieff, N., Musacchio, A., and Nogales, E. (2010). The Ndc80 kinetochore complex forms oligomeric arrays along microtubules. *Nature*, 467(7317):805–810.

Amaro, A. C., Samora, C. P., Holtackers, R., Wang, E., Kingston, I. J., Alonso, M., Lampson, M., McAinsh, A. D., and Meraldi, P. (2010). Molecular control of kinetochore-microtubule dynamics and chromosome oscillations. *Nature Cell Biology*, 12(4):319–329. 10.1038/ncb2033.

Aravamudhan, P., Goldfarb, A. A., and Joglekar, A. P. (2015). The kinetochore encodes a mechanical switch to disrupt spindle assembly checkpoint signalling. *Nature Cell Biology*, 17(7):868–879.

Armond, J. W., Harry, E. F., McAinsh, A. D., and Burroughs, N. J. (2015). Inferring the forces controlling metaphase kinetochore oscillations by reverse engineering system dynamics. *PLOS Computational Biology*, 11(11):1–26.

Asbury, C. (2017). Anaphase A: Disassembling microtubules move chromosomes toward spindle poles. *Biology*, 6(1):15.

Asbury, C. L., Gestaut, D. R., Powers, A. F., Franck, A. D., and Davis, T. N. (2006). The dam1 kinetochore complex harnesses microtubule dynamics to produce force and movement. *Proceedings of the National Academy of Sciences*, 103(26):9873–9878.

Asbury, C. L., Tien, J. F., and Davis, T. N. (2011). Kinetochores' gripping feat: conformational wave or biased diffusion? *Trends in Cell Biology*, 21(1):38–46.

Auckland, P., Clarke, N. I., Royle, S. J., and McAinsh, A. D. (2017). Congressing kinetochores progressively load Ska complexes to prevent force-dependent detachment. *The Journal of Cell Biology*.

Austen, K., Kluger, C., Freikamp, A., Chrostek-Grashoff, A., and Grashoff, C. (2013). *Cell-Cell Interactions*, volume 1066 of *Methods in Molecular Biology*, chapter 15: Generation and analysis of biosensors to measure mechanical forces within cells, pages 169–184. Humana Press, Totowa, NJ.

Austen, K., Ringer, P., Mehlich, A., Chrostek-Grashoff, A., Kluger, C., Klingner, C., Sabass, B., Zent, R., Rief, M., and Grashoff, C. (2015). Extracellular rigidity sensing by talin isoform-specific mechanical linkages. *Nature Cell Biology*, 17(12):1597–1606.

Barisic, M., Silva e Sousa, R., Tripathy, S. K., Magiera, M. M., Zaytsev, A. V., Pereira, A. L., Janke, C., Grishchuk, E. L., and Maiato, H. (2015). Microtubule detyrosination guides chromosomes during mitosis. *Science*, 348(6236):799–803.

Biggins, S. (2013). The composition, functions, and regulation of the budding yeast kinetochore. *Genetics*, 194(4):817–846.

Borenstein, M., Hedges, L. V., Higgins, J. P., and Rothstein, H. R. (2010). A basic introduction to fixed-effect and random-effects models for meta-analysis. *Research Synthesis Methods*, 1(2):97–111.

Borenstein, M., Hedges, L. V., Higgins, J. P. T., and Rothstein, H. R. (2009). *Introduction to Mta-Analysis*, chapter Effect sizes based on means, pages 21–32. John Wiley & Sons, Ltd.

Borenstein, M., Hedges, L. V., and Rothstein, H. R. (2007). Meta-analysis – fixed effects vs. random effects. www.meta-analysis.com.

Burbank, K. S., Groen, A. C., Perlman, Z. E., Fisher, D. S., and Mitchison, T. J. (2006). A new method reveals microtubule minus ends throughout the meiotic spindle. *The Journal of Cell Biology*, 175(3):369–375.

Chacón, J. M., Mukherjee, S., Schuster, B. M., Clarke, D. J., and Gardner, M. K. (2014). Pericentromere tension is self-regulated by spindle structure in metaphase. *The Journal of Cell Biology*, 205(3):313–324.

Cheeseman, I. M. (2014). The kinetochore. *Cold Spring Harbor Perspectives in Biology*, 6(7).

Cheeseman, I. M., Chappie, J. S., Wilson-Kubalek, E. M., and Desai, A. (2006). The conserved KMN network constitutes the core microtubule-binding site of the kinetochore. *Cell*, 127(5):983 – 997.

Cheeseman, I. M., Hori, T., Fukagawa, T., and Desai, A. (2008). Knl1 and the CENP-H/I/K complex coordinately direct kinetochore assembly in vertebrates. *Molecular Biology of the Cell*, 19(2):587–594.

Cheeseman, I. M., Niessen, S., Anderson, S., Hyndman, F., Yates, J. R., Oegema, K., and Desai, A. (2004). A conserved protein network controls assembly of the outer kinetochore and its ability to sustain tension. *Genes & Development*, 18(18):2255–2268.

Cieśliński, K. and Ries, J. (2014). The yeast kinetochore — structural insights from optical microscopy. *Current Opinion in Chemical Biology*, 20:1 – 8. Molecular imaging.

Ciferri, C., Pasqualato, S., Screpanti, E., Varetti, G., Santaguida, S., Reis, G. D., Maiolica, A., Polka, J., Luca, J. G. D., Wulf, P. D., Salek, M., Rappsilber, J., Moores, C. A., Salmon, E. D., and Musacchio, A. (2008). Implications for kinetochore-microtubule attachment from the structure of an engineered Ndc80 complex. *Cell*, 133(3):427 – 439.

Civelekoglu-Scholey, G., He, B., Shen, M., Wan, X., Roscioli, E., Bowden, B., and Cimini, D. (2013). Dynamic bonds and polar ejection force distribution explain kinetochore oscillations in PtK1 cells. *The Journal of Cell Biology*, 201(4):577–593.

Cost, A.-L., Ringer, P., Chrostek-Grashoff, A., and Grashoff, C. (2015). How to measure molecular forces in cells: A guide to evaluating genetically-encoded fret-based tension sensors. *Cellular and Molecular Bioengineering*, 8(1):96–105.

DeLuca, K. F., Lens, S. M. A., and DeLuca, J. G. (2011). Temporal changes in hec1 phosphorylation control kinetochore–microtubule attachment stability during mitosis. *Journal of Cell Science*, 124(4):622–634.

Dong, Y., Vanden Beldt, K. J., Meng, X., Khodjakov, A., and McEwen, B. F. (2007). The outer plate in vertebrate kinetochores is a flexible network with multiple microtubule interactions. *Nature Cell Biology*, 9(5):516–522.

Drpic, D., Pereira, A., Barisic, M., Maresca, T., and Maiato, H. (2015). Polar ejection forces promote the conversion from lateral to end-on kinetochore-microtubule attachments on monooriented chromosomes. *Cell Reports*, 13(3):460 – 468.

Dumont, S., Salmon, E. D., and Mitchison, T. J. (2012). Deformations within moving kinetochores reveal different sites of active and passive force generation. *Science*, 337(6092):355–358.

Elting, M. W., Hueschen, C. L., Udy, D. B., and Dumont, S. (2014). Force on spindle microtubule minus ends moves chromosomes. *The Journal of Cell Biology*, 206(2):245–256.

Engler, A. J., Sen, S., Sweeney, H. L., and Discher, D. E. (2006). Matrix elasticity directs stem cell lineage specification. *Cell*, 126(4):677 – 689.

Espeut, J., Cheerambathur, D. K., Krenning, L., Oegema, K., and Desai, A. (2012). Microtubule binding by KNL-1 contributes to spindle checkpoint silencing at the kinetochore. *The Journal of Cell Biology*, 196(4):469–482.

Etemad, B., Kuijt, T. E. F., and Kops, G. J. P. L. (2015). Kinetochore-microtubule attachment is sufficient to satisfy the human spindle assembly checkpoint. *Nature Communications*, 6:8987.

Fang, J., Mehlich, A., Koga, N., Huang, J., Koga, R., Gao, X., Hu, C., Jin, C., Rief, M., Kast, J., Baker, D., and Li, H. (2013). Forced protein unfolding leads to highly elastic and tough protein hydrogels. *Nature Communications*, 4:2974.

Ferraro-Gideon, J., Sheykhani, R., Zhu, Q., Duquette, M. L., Berns, M. W., and Forer, A. (2013). Measurements of forces produced by the mitotic spindle using optical tweezers. *Molecular Biology of the Cell*, 24(9):1375–1386.

Finch-Edmondson, M. and Sudol, M. (2016). Framework to function: mechanosensitive regulators of gene transcription. *Cellular & Molecular Biology Letters*, 21(1):28.

Foley, E. A. and Kapoor, T. M. (2013). Microtubule attachment and spindle assembly checkpoint signalling at the kinetochore. *Nature Reviews Molecular Cell Biology*, 14(1):25–37.

Forth, S. and Kapoor, T. M. (2017). The mechanics of microtubule networks in cell division. *The Journal of Cell Biology*, 216(6):1525–1531.

Franck, A. D., Powers, A. F., Gestaut, D. R., Gonen, T., Davis, T. N., and Asbury, C. L. (2007). Tension applied through the Dam1 complex promotes microtubule elongation providing a direct mechanism for length control in mitosis. *Nature Cell Biology*, 9(7):832–837.

Frank, B. S., Vardar, D., Buckley, D. A., and McKnight, C. J. (2002). The role of aromatic residues in the hydrophobic core of the villin headpiece subdomain. *Protein Science*, 11(3):680–687.

Fredericson, M., Chew, K., Ngo, J., Cleek, T., Kiratli, J., and Cobb, K. (2007). Regional bone mineral density in male athletes: a comparison of soccer players, runners and controls. *British Journal of Sports Medicine*, 41(10):664–668.

Freikamp, A., Cost, A.-L., and Grashoff, C. (2016). The piconewton force awakens: Quantifying mechanics in cells. *Trends in Cell Biology*, 26(11):838 – 847. Special Issue: Future of Cell Biology.

Freikamp, A., Mehlich, A., Klingner, C., and Grashoff, C. (2017). Investigating piconewton forces in cells by FRET-based molecular force microscopy. *Journal of Structural Biology*, 197(1):37 – 42. Molecular Forces to Cellular Function.

Fuller, B. G., Lampson, M. A., Foley, E. A., Rosasco-Nitcher, S., Le, K. V., Tobelmann, P., Brautigan, D. L., Stukenberg, P. T., and Kapoor, T. M. (2008). Midzone activation of Aurora B in anaphase produces an intracellular phosphorylation gradient. *Nature*, 453(7198):1132–1136.

Gadella, T., editor (2009). *FRET and FLIM Techniques*, volume 33 of *Laboratory techniques in biochemistry and molecular biology*. ELSEVIER SCIENCE & TECHNOLOGY.

Glotzer, M. (2016). Cytokinesis in metazoa and fungi. *Cold Spring Harbor Perspectives in Biology*.

Grashoff, C., Hoffman, B. D., Brenner, M. D., Zhou, R., Parsons, M., Yang, M. T., McLean, M. A., Sligar, S. G., Chen, C. S., Ha, T., and Schwartz, M. A. (2010). Measuring mechanical tension across vinculin reveals regulation of focal adhesion dynamics. *Nature*, 466(7303):263–266.

Grishchuk, E. L. and McIntosh, J. R. (2006). Microtubule depolymerization can drive poleward chromosome motion in fission yeast. *The EMBO Journal*, 25(20):4888–4896.

Hori, T., Amano, M., Suzuki, A., Backer, C. B., Welburn, J. P., Dong, Y., McEwen, B. F., Shang, W.-H., Suzuki, E., Okawa, K., Cheeseman, I. M., and Fukagawa, T. (2008). CCAN makes multiple contacts with centromeric DNA to provide distinct pathways to the outer kinetochore. *Cell*, 135(6):1039 – 1052.

Howell, B., McEwen, B., Canman, J., Hoffman, D., Farrar, E., Rieder, C., and Salmon, E. (2001). Cytoplasmic dynein/dynactin drives kinetochore protein transport to the spindle poles and has a role in mitotic spindle checkpoint inactivation. *The Journal of Cell Biology*, 155(7):1159–1172.

Huis in 't Veld, P. J., Jeganathan, S., Petrovic, A., Singh, P., John, J., Krenn, V., Weissmann, F., Bange, T., and Musacchio, A. (2016). Molecular basis of outer kinetochore assembly on CENP-T. *eLife*, 5:e21007.

Hynes, R. O. (2002). Integrins: Bidirectional, allosteric signaling machines. *Cell*, 110(6):673 – 687.

Ingber, D. (2003). Mechanobiology and diseases of mechanotransduction. *Annals of Medicine*, 35(8):564–577. PMID: 14708967.

Jeyaprakash, A., Santamaria, A., Jayachandran, U., Chan, Y., Benda, C., Nigg, E., and Conti, E. (2012). Structural and functional organization of the Ska complex, a key component of the kinetochore-microtubule interface. *Molecular Cell*, 46(3):274 – 286.

Joglekar, A. (2016). A cell biological perspective on past, present and future investigations of the spindle assembly checkpoint. *Biology*, 5(4):44.

Joglekar, A. P., Bloom, K., and Salmon, E. (2009). In vivo protein architecture of the eukaryotic kinetochore with nanometer scale accuracy. *Current Biology*, 19(8):694–699.

Joglekar, A. P., Bouck, D. C., Molk, J. N., Bloom, K. S., and Salmon, E. D. (2006). Molecular architecture of a kinetochore-microtubule attachment site. *Nature Cell Biology*, 8(6):581–585.

Johnston, K., Joglekar, A., Hori, T., Suzuki, A., Fukagawa, T., and Salmon, E. (2010). Vertebrate kinetochore protein architecture: protein copy number. *The Journal of Cell Biology*, 189(6):937–943.

Kajtez, J., Solomatina, A., Novak, M., Polak, B., Vukušić, K., Rüdiger, J., Cojoc, G., Milas, A., Šumanovac Šestak, I., Risteski, P., Tavano, F., Klemm, A. H., Roscioli, E., Welburn, J., Cimini, D., Gluncić, M., Pavin, N., and Tolić, I. M. (2016). Overlap microtubules link sister k-fibres and balance the forces on bi-oriented kinetochores. *Nature Communications*, 7:10298.

Khodjakov, A. and Pines, J. (2010). Centromere tension: a divisive issue. *Nature Cell Biology*, 12(10):919–923.

Khodjakov, A. and Rieder, C. L. (1996). Kinetochores moving away from their associated pole do not exert a significant pushing force on the chromosome. *The Journal of Cell Biology*, 135(2):315–327.

Källberg, M., Wang, H., Wang, S., Peng, J., Wang, Z., Lu, H., and Xu, J. (2012). Template-based protein structure modeling using the RaptorX web server. *Nature Protocols*, 7(8):1511–1522.

Laband, K., Stefanutti, M., and Dumont1, J. (2016). An atypical mechanism of chromosome segregation in the C. elegans oocyte. volume 27, pages 3947–P1904.

Lakowicz, J. R. (2006). *Principles of Fluorescence Spectroscopy*, chapter 13 Energy Transfer. Springer-Verlag New York Inc.

Lam, A. J., St-Pierre, F., Gong, Y., Marshall, J. D., Cranfill, P. J., Baird, M. A., McKeown, M. R., Wiedenmann, J., Davidson, M. W., Schnitzer, M. J., Tsien, R. Y., and Lin, M. Z. (2012). Improving FRET dynamic range with bright green and red fluorescent proteins. *Nature Methods*, 9(10):1005–1012.

Lampert, F., Hornung, P., and Westermann, S. (2010). The Dam1 complex confers microtubule plus end–tracking activity to the Ndc80 kinetochore complex. *The Journal of Cell Biology*, 189(4):641–649.

Lampson, M. and Grishchuk, E. (2017). Mechanisms to avoid and correct erroneous kinetochore-microtubule attachments. *Biology*, 6(1):1.

Lodish, H., Berk, A., Kaiser, C. A., Krieger, M., Scott, M. P., Bretscher, A., Ploegh, H., and Matsudaira, P. T. (2007). *Molecular Cell Biology*. W.H.Freeman & Co Ltd.

London, N. and Biggins, S. (2014). Signalling dynamics in the spindle checkpoint response. *Nature Reviews. Molecular Cell Biology*, 15(11):736–748.

Magidson, V., He, J., Ault, J. G., O'Connell, C. B., Yang, N., Tikhonenko, I., McEwen, B. F., Sui, H., and Khodjakov, A. (2016). Unattached kinetochores rather than intrakinetochore tension arrest mitosis in taxol-treated cells. *The Journal of Cell Biology*, 212(3):307–319.

Maiato, H., Gomes, A., Sousa, F., and Barisic, M. (2017). Mechanisms of chromosome congression during mitosis. *Biology*, 6(1):13.

Maresca, T. J. and Salmon, E. D. (2009). Intrakinetochore stretch is associated with changes in kinetochore phosphorylation and spindle assembly checkpoint activity. *The Journal of Cell Biology*, 184(3):373–381.

Maresca, T. J. and Salmon, E. D. (2010). Welcome to a new kind of tension: translating kinetochore mechanics into a wait-anaphase signal. *Journal of Cell Science*, 123(6):825–835.

McCleland, M. L., Gardner, R. D., Kallio, M. J., Daum, J. R., Gorbsky, G. J., Burke, D. J., and Stukenberg, P. T. (2003). The highly conserved Ndc80 complex is required for kinetochore assembly, chromosome congression, and spindle checkpoint activity. *Genes & Development*, 17(1):101–114.

McEwen, B. F., Dong, Y., and VandenBeldt, K. J. (2007). Using electron microscopy to understand functional mechanisms of chromosome alignment on the mitotic spindle. In *Cellular Electron Microscopy*, volume 79 of *Methods in Cell Biology*, pages 259 – 293. Academic Press.

McIntosh, J. (1991). Structural and mechanical control of mitotic progression. *Cold Spring Harbor Symposia on Quantitative Biology*, 56(0):613–619.

McIntosh, J. R. (2016). Mitosis. *Cold Spring Harbor Perspectives in Biology*, 8(9).

McIntosh, J. R., O'Toole, E., Zhudenkov, K., Morphew, M., Schwartz, C., Ataullakhanov, F. I., and Grishchuk, E. L. (2013). Conserved and divergent features of kinetochores and spindle microtubule ends from five species. *The Journal of Cell Biology*, 200(4):459–474.

McKinley, K. L. and Cheeseman, I. M. (2016). The molecular basis for centromere identity and function. *Nature Reviews. Molecular Cell Biology*, 17(1):16–29.

Meraldi, P., McAinsh, A. D., Rheinbay, E., and Sorger, P. K. (2006). Phylogenetic and structural analysis of centromeric dna and kinetochore proteins. *Genome Biology*, 7(3):R23.

Miller, M. P., Asbury, C. L., and Biggins, S. (2016). A TOG protein confers tension sensitivity to kinetochore-microtubule attachments. *Cell*, 165(6):1428–1439.

Musacchio, A. (2015). The molecular biology of spindle assembly checkpoint signaling dynamics. *Current Biology*, 25(20):R1002 – R1018.

Musacchio, A. and Desai, A. (2017). A molecular view of kinetochore assembly and function. *Biology*, 6(1):5.

Nagpal, H. and Fukagawa, T. (2016). Kinetochore assembly and function through the cell cycle. *Chromosoma*, 125(4):645–659.

Nicklas, R. B. (1965). Chromosome velocity during mitosis as a function of chromosome size and position. *The Journal of Cell Biology*, 25(1):119–135.

Nicklas, R. B. (1969). CHROMOSOME MICROMANIPULATION: III. spindle fiber tension and the reorientation of mal-oriented chromosomes. *The Journal of Cell Biology*, 43(1):40–50.

Nicklas, R. B. (1983). Measurements of the force produced by the mitotic spindle in anaphase. *The Journal of Cell Biology*, 97(2):542–548.

Nicklas, R. B. (1988). The forces that move chromosomes in mitosis. *Annual Review of Biophysics and Biophysical Chemistry*, 17(1):431–449.

Nishino, T., Rago, F., Hori, T., Tomii, K., Cheeseman, I. M., and Fukagawa, T. (2013). CENP-T provides a structural platform for outer kinetochore assembly. *The EMBO Journal*, 32(3):424–436.

Pavin, N. and Tolić, I. M. (2016). Self-organization and forces in the mitotic spindle. *Annual Review of Biophysics*, 45(1):279–298. PMID: 27145873.

Perpelescu, M. and Fukagawa, T. (2011). The abcs of cenps. *Chromosoma*, 120(5):425.

Pesenti, M. E., Weir, J. R., and Musacchio, A. (2016). Progress in the structural and functional characterization of kinetochores. *Current Opinion in Structural Biology*, 37:152 – 163.

Petrovic, A., Keller, J., Liu, Y., Overlack, K., John, J., Dimitrova, Y. N., Jenni, S., van Gerwen, S., Stege, P., Wohlgemuth, S., Rombaut, P., Herzog, F., Harrison, S. C., Vetter, I. R., and Musacchio, A. (2016). Structure of the MIS12 complex and molecular basis of its interaction with CENP-C at human kinetochores. *Cell*, 167(4):1028 – 1040.e15.

Pfaltzgraff, E. R., Roth, G. M., Miller, P. M., Gintzig, A. G., Ohi, R., and Bader, D. M. (2016). Loss of CENP-F results in distinct microtubule-related defects without chromosomal abnormalities. *Molecular Biology of the Cell*, 27(13):1990–1999.

Phillip, J. M., Aifuwa, I., Walston, J., and Wirtz, D. (2015). The mechanobiology of aging. *Annual Review of Biomedical Engineering*, 17(1):113–141. PMID: 26643020.

Pivetti, C. D., Yen, M.-R., Miller, S., Busch, W., Tseng, Y.-H., Booth, I. R., and Saier, Jr., M. H. (2003). Two families of mechanosensitive channel proteins. *Microbiology and Molecular Biology Reviews*, 67(1):66–85.

Powers, A. F., Franck, A. D., Gestaut, D. R., Cooper, J., Gracyzk, B., Wei, R. R., Wordeman, L., Davis, T. N., and Asbury, C. L. (2009). The Ndc80 kinetochore complex forms load-bearing attachments to dynamic microtubule tips via biased diffusion. *Cell*, 136(5):865 – 875.

Rago, F., Gascoigne, K., and Cheeseman, I. (2015). Distinct organization and regulation of the outer kinetochore KMN network downstream of CENP-C and CENP-T. *Current Biology*, 25(5):671 – 677.

Ribeiro, S. A., Gatlin, J. C., Dong, Y., Joglekar, A., Cameron, L., Hudson, D. F., Farr, C. J., McEwen, B. F., Salmon, E. D., Earnshaw, W. C., and Vagnarelli, P. (2009). Condensin regulates the stiffness of vertebrate centromeres. *Molecular Biology of the Cell*, 20(9):2371–2380.

Rieder, C. L., Cole, R. W., Khodjakov, A., and Sluder, G. (1995). The checkpoint delaying anaphase in response to chromosome monoorientation is mediated by an inhibitory signal produced by unattached kinetochores. *The Journal of Cell Biology*, 130(4):941–948.

Ringer, P., Colo, G., Fässler, R., and Grashoff, C. (2017a). Sensing the mechano-chemical properties of the extracellular matrix. *Matrix Biology*. epub ahead of print.

Ringer, P., Weißl, A., Cost, A.-L., Freikamp, A., Sabass, B., Mehlich, A., Tramier, M., Rief, M., and Grashoff, C. (2017b). Multiplexing molecular tension sensors reveals piconewton force gradient across talin-1. *Nat Meth*, advance online publication.

Ross, M. H. and Pawlina, W. (2006). *Histology: A Text and Atlas*. Lippincott Williams & Wilkins, 5th edition.

Rothenberg, K. E., Neibart, S. S., LaCroix, A. S., and Hoffman, B. D. (2015). Controlling cell geometry affects the spatial distribution of load across vinculin. *Cellular and Molecular Bioengineering*, 8(3):364–382.

Rubinstein, B., Larripa, K., Sommi, P., and Mogilner, A. (2009). The elasticity of motor–microtubule bundles and shape of the mitotic spindle. *Physical Biology*, 6(1):016005.

Samejima, I., Spanos, C., Alves, F. d. L., Hori, T., Perpelescu, M., Zou, J., Rappsilber, J., Fukagawa, T., and Earnshaw, W. C. (2015). Whole-proteome genetic analysis of dependencies in assembly of a vertebrate kinetochore. *The Journal of Cell Biology*, 211(6):1141–1156.

Schleiffer, A., Maier, M., Litos, G., Lampert, F., Hornung, P., Mechtler, K., and Westermann, S. (2012). Cenp-t proteins are conserved centromere receptors of the ndc80 complex. *Nature Cell Biology*, 14(6):604–613.

Schmidt, J., Arthanari, H., Boeszoermenyi, A., Dashkevich, N., Wilson-Kubalek, E., Monnier, N., Markus, M., Oberer, M., Milligan, R., Bathe, M., Wagner, G., Grishchuk, E., and Cheeseman, I. (2012). The kinetochore-bound ska1 complex tracks depolymerizing microtubules and binds to curved protofilaments. *Developmental Cell*, 23(5):968–980.

Scholey, J., Civelekoglu-Scholey, G., and Brust-Mascher, I. (2016). Anaphase B. *Biology*, 5(4):51.

Sharp, D. J., Rogers, G. C., and Scholey, J. M. (2000). Cytoplasmic dynein is required for poleward chromosome movement during mitosis in drosophila embryos. *Nature Cell Biology*, 2(12):922–930.

Sikirzhytski, V., Magidson, V., Steinman, J. B., He, J., Le Berre, M., Tikhonenko, I., Ault, J. G., McEwen, B. F., Chen, J. K., Sui, H., Piel, M., Kapoor, T. M., and Khodjakov, A. (2014). Direct kinetochore–spindle pole connections are not required for chromosome segregation. *The Journal of Cell Biology*.

Simunić, J. and Tolić, I. M. (2016). Mitotic spindle assembly: Building the bridge between sister k-fibers. *Trends in Biochemical Sciences*, 41(10):824–833.

Skibbens, R. V., Skeen, V. P., and Salmon, E. D. (1993). Directional instability of kinetochore motility during chromosome congression and segregation in mitotic newt lung cells: a push-pull mechanism. *The Journal of Cell Biology*, 122(4):859–875.

Smith, C. A., McAinsh, A. D., and Burroughs, N. J. (2016). Human kinetochores are swivel joints that mediate microtubule attachments. *eLife*, 5:e16159.

Sun, Z., Guo, S. S., and Fässler, R. (2016). Integrin-mediated mechanotransduction. *The Journal of Cell Biology*, 215(4):445–456.

Sundin, L. J., Guimaraes, G. J., and DeLuca, J. G. (2011). The NDC80 complex proteins Nuf2 and Hec1 make distinct contributions to kinetochore–microtubule attachment in mitosis. *Molecular Biology of the Cell*, 22(6):759–768.

Sutradhar, S. and Paul, R. (2014). Tug-of-war between opposing molecular motors explains chromosomal oscillation during mitosis. *Journal of Theoretical Biology*, 344:56 – 69.

Suzuki, A., Badger, B., Wan, X., DeLuca, J., and Salmon, E. (2014). The architecture of CCAN proteins creates a structural integrity to resist spindle forces and achieve proper intrakinetochore stretch. *Developmental Cell*, 30(6):717 – 730.

Suzuki, A., Badger, B. L., Haase, J., Ohashi, T., Erickson, H. P., Salmon, E. D., and Bloom, K. (2016). How the kinetochore couples microtubule force and centromere stretch to move chromosomes. *Nature Cell Biology*, 18(4):382–392.

Suzuki, A., Badger, B. L., and Salmon, E. D. (2015a). A quantitative description of Ndc80 complex linkage to human kinetochores. *Nature Communications*, 6:8161.

Suzuki, A., Hori, T., Nishino, T., Usukura, J., Miyagi, A., Morikawa, K., and Fukagawa, T. (2011). Spindle microtubules generate tension-dependent changes in the distribution of inner kinetochore proteins. *The Journal of Cell Biology*, 193(1):125–140.

Suzuki, K., Sako, K., Akiyama, K., Isoda, M., Senoo, C., Nakajo, N., and Sagata, N. (2015b). Identification of non-ser/thr-pro consensus motifs for cdk1 and their roles in mitotic regulation of c2h2 zinc finger proteins and ect2. *Scientific Reports*, 5:7929.

Takeuchi, K. and Fukagawa, T. (2012). Molecular architecture of vertebrate kinetochores. *Experimental Cell Research*, 318(12):1367 – 1374. Special Review Issue: Chromosome Biology, 2012.

Tanaka, K., Kitamura, E., Kitamura, Y., and Tanaka, T. U. (2007). Molecular mechanisms of microtubule-dependent kinetochore transport toward spindle poles. *The Journal of Cell Biology*, 178(2):269–281.

Tauchman, E. C., Boehm, F. J., and DeLuca, J. G. (2015). Stable kinetochore-microtubule attachment is sufficient to silence the spindle assembly checkpoint in human cells. *Nature Communications*, 6:10036.

Theodosiou, M., Widmaier, M., Böttcher, R. T., Rognoni, E., Veelders, M., Bharadwaj, M., Lambacher, A., Austen, K., Müller, D. J., Zent, R., and Fässler, R. (2015). Kindlin-2 cooperates with talin to activate integrins and induces cell spreading by directly binding paxillin. *eLife*, 5:e10130.

Thomas, W. (2008). Catch bonds in adhesion. *Annual Review of Biomedical Engineering*, 10(1):39–57. PMID: 18647111.

Tien, J. F., Umbreit, N. T., Gestaut, D. R., Franck, A. D., Cooper, J., Wordeman, L., Gonen, T., Asbury, C. L., and Davis, T. N. (2010). Cooperation of the Dam1 and Ndc80 kinetochore complexes enhances microtubule coupling and is regulated by aurora B. *The Journal of Cell Biology*, 189(4):713–723.

Uchida, K. S., Takagaki, K., Kumada, K., Hirayama, Y., Noda, T., and Hirota, T. (2009). Kinetochore stretching inactivates the spindle assembly checkpoint. *The Journal of Cell Biology*, 184(3):383–390.

Valente, L. P., Silva, M. C. C., and Jansen, L. E. T. (2012). Temporal control of epigenetic centromere specification. *Chromosome Research*, 20(5):481–492.

van Hooff, J. J., Tromer, E., van Wijk, L. M., Snel, B., and Kops, G. J. (2017). Evolutionary dynamics of the kinetochore network in eukaryotes as revealed by comparative genomics. *EMBO reports*.

Volkov, V. A., Grissom, P. M., Arzhanik, V. K., Zaytsev, A. V., Renganathan, K., McClure-Begley, T., Old, W. M., Ahn, N., and McIntosh, J. R. (2015). Centromere protein F includes two sites that couple efficiently to depolymerizing microtubules. *The Journal of Cell Biology*, 209(6):813–828.

Volkov, V. A., Zaytsev, A. V., Gudimchuk, N., Grissom, P. M., Gintsburg, A. L., Ataullakhanov, F. I., McIntosh, J. R., and Grishchuk, E. L. (2013). Long tethers provide high-force coupling of the Dam1 ring to shortening microtubules. *Proceedings of the National Academy of Sciences*, 110(19):7708–7713.

Walczak, C. E., Cai, S., and Khodjakov, A. (2010). Mechanisms of chromosome behaviour during mitosis. *Nature Reviews. Molecular Cell Biology*, 11(2):91–102.

Wan, X., O'Quinn, R. P., Pierce, H. L., Joglekar, A. P., Gall, W. E., DeLuca, J. G., Carroll, C. W., Liu, S.-T., Yen, T. J., McEwen, B. F., Stukenberg, P. T., Desai, A., and Salmon, E. (2009). Protein architecture of the human kinetochore microtubule attachment site. *Cell*, 137(4):672–684.

Wei, S. C. and Yang, J. (2016). Forcing through tumor metastasis: The interplay between tissue rigidity and epithelial–mesenchymal transition. *Trends in Cell Biology*, 26(2):111 – 120.

Wendell, K., Wilson, L., and Jordan, M. (1993). Mitotic block in HeLa cells by vinblastine: ultrastructural changes in kinetochore-microtubule attachment and in centrosomes. *Journal of Cell Science*, 104(2):261–274.

Westermann, S. and Schleiffer, A. (2013). Family matters: structural and functional conservation of centromere-associated proteins from yeast to humans. *Trends in Cell Biology*, 23(6):260 – 269.

Wilson, M. (2016). Microscope resolution: Concepts, factors and calculation. http://www.leica-microsystems.com/science-lab/microscope-resolution-concepts-factors-and-calculation/.

Wilson-Kubalek, E. M., Cheeseman, I. M., Yoshioka, C., Desai, A., and Milligan, R. A. (2008). Orientation and structure of the Ndc80 complex on the microtubule lattice. *The Journal of Cell Biology*, 182(6):1055–1061.

Xiao, S., Bi, Y., Shan, B., and Raleigh, D. P. (2009). Analysis of core packing in a cooperatively folded miniature protein: The ultrafast folding villin headpiece helical subdomain. *Biochemistry*, 48(21):4607–4616. PMID: 19354264.

Ye, A. A., Cane, S., and Maresca, T. J. (2016). Chromosome biorientation produces hundreds of piconewtons at a metazoan kinetochore. *Nature Communications*, 7:13221.

Yoo, T. Y. and Needleman, D. J. (2016). *The Mitotic Spindle*, chapter Studying Kinetochores In Vivo Using FLIM-FRET, pages 169–186. Methods and Protocols. Springer New York, New York, NY.

Yu, C., Redemann, S., Wu, H., Yoo, T., Müller-Reichert, T., and Needleman, D. (2016). Microtubules push chromosomes apart in anaphase. In *Molecular Biology of the Cell*, volume 27, pages 3947–P1022.

Zaytsev, A. V., Mick, J. E., Maslennikov, E., Nikashin, B., DeLuca, J. G., and Grishchuk, E. L. (2015). Multisite phosphorylation of the NDC80 complex gradually tunes its microtubule-binding affinity. *Molecular Biology of the Cell*, 26(10):1829–1844.

Zaytsev, A. V., Sundin, L. J., DeLuca, K. F., Grishchuk, E. L., and DeLuca, J. G. (2014). Accurate phosphoregulation of kinetochore–microtubule affinity requires unconstrained molecular interactions. *The Journal of Cell Biology*, 206(1):45–59.

Žoldák, G., Stigler, J., Pelz, B., Li, H., and Rief, M. (2013). Ultrafast folding kinetics and cooperativity of villin headpiece in single-molecule force spectroscopy. *Proceedings of the National Academy of Sciences*, 110(45):18156–18161.

Acknowledgments

Even though I am presenting this document as *my* thesis, many people supported this work with essential contributions over the past years.

First and foremost, I want to thank Dr. Carsten Grashoff for his continuous support and supervision over the past years. Thank you not only for initiating the project and establishing an interdisciplinary environment, but also for your permanently open door and plenty of hours filled with discussion. I further want to thank Prof. Reinhard Fässler for providing a great infrastructure and access to all facilities of his department.

I also want to thank Prof. Klaus Förstemann and Prof. Ulrike Gaul for taking on the task of being my "Doktorvater/Doktormutter" even though I was – as an external student – not available to them.

Since the biological aspects of my project were quite distinct from what all other people of my group and department were working on, the input of my Thesis Advisory Committee was of particular value for me. I therefore want to thank my TAC members Prof. Zuzana Storchová, Dr. Günther Woehlke, and Dr. Wolfgang Zachariae not only for their scientific input, but also for their commitment which included easy and fast scheduling of the meetings (sounds trivial, but makes a PhD student's life *a lot* easier!). In addition, I want to thank Dr. Günther Woehlke for his emails sent in the aftermath of the meetings about things that came a little short and for further accompanying my project until the very end by serving as 2nd referee and being a member of my defense committee. I further want to thank the other committee members Dr. Franz Herzog, Prof. Stefan Zahler, Prof. Ralf Jungmann, and Prof. Karl-Peter Hopfner.

Besides those who were involved in the formal infrastructure surrounding this project, a number of people contributed less formally bot not less significantly.

First of all, I want to thank Dr. Christoph Klingner for the kinetochore analysis software package. Even though you generously wrote "by: Andrea Freikamp, Carleen Kluger, Christoph Klingner" in the program header, I am totally aware that the whole program was your work – and one of the two legs of the project.

The other leg was the CENP-T$^{tet\text{-}off}$ cell line generated by Tatsuo Fukagawa and his lab and kindly shared with us. Changing the system to an established knockout cell line was an important turning point of this project and I am grateful for this opportunity.

I further want to thank all members of the Grashoff lab as well as a number of people form other labs who supported me with advice and company – scientifically as well as aside of science. I want to specifically mention Dr. Anna Chrostek-Grashoff for helping with all the daily lab work and Anna-Lena Cost and Dr. Carleen Kluger for the FLIM analysis software. Besides that, I will forego an extensive list of details and hope that I already showed you my thankfulness and appreciation though my words and actions during the past years! (And if I missed that, a reference in the acknowledgments section could not make up for it anyway...)

I also want to thank Dr. Armin Lambacher and all former and present staff of the MPI-B Imaging Facility. Besides keeping the various equipment in good condition, you always had (or took) time for my numerous questions and interesting discussions during which I learned a lot about my favorite laboratory technique.

The burden of being mainly noticed when they are absent is shared by Lidia Wimmer and Klaus Weber. Thank you for taking care of all daily and exceptional needs and making our lives so comfortable!

Scientific education does not end at the lab's door sill and I was so fortunate to be part of two great programs: the International Max Planck Research School for Molecular Life Sciences (IMPRS-LS) and the PhD fellowship program of the Boehringer Ingelheim Fonds (BIF). I want to say a cordial *Thank You!* to all staff members of both institutions (and their sponsoring bodies ;-)) for enabling me to attend conferences, workshops and summer schools, but also for your great and wholehearted personal support!

I also want to thank Roland for supporting my development to a developer (well, I know, calling myself a software developer is an overstatement, but the duck was hungry ...) and showing me the benefits and functions of revision-control tools that I don't want to miss anymore.

Last but not least (and it won't come as a surprise to them) I am certainly *not* thanking my parents for helping me to get independent by teaching me how to walk (which anyway is completely useless if you spent most of your time sitting at a microscope, a cell culture bench, or in front of a keyboard and monitor ...). But I *do* say thank you for once again going through the effort of finding all (or most of) my tyops. ;-)

Contact details

Affiliation	Max Planck Institute of Biochemistry Group of Molecular Mechanotransduction Direct supervisor: Dr. Carsten Grashoff Am Klopferspitz 18, 81252 Martinsried, Germany
Personal contact	andrea.freikamp@gmx.de

Publications

Ringer, P., Weißl, A., Cost, A.-L., **Freikamp, A.**, Sabass, B., Mehlich, A., Tramier, M., Rief, M., and Grashoff, C. (2017). Multiplexing molecular tension sensors reveals force gradient across talin-1. *Nature Methods*, advance online publication.

Freikamp, A., Mehlich, A., Klingner, C., and Grashoff, C. (2017). Investigating piconewton forces in cells by FRET-based molecular force microscopy. *Journal of Structural Biology*, 197(1):37 – 42. Molecular Forces to Cellular Function.

Freikamp, A., Weißl, A., Rief, M., and Grashoff, C. (2016). Molecular force measurements across the kinetochore protein CENP-T. *Molecular Biology of the Cell*, 27(25):3947–P1068.

Freikamp, A.*, Cost, A.-L.*, and Grashoff, C. (2016). The piconewton force awakens: Quantifying mechanics in cells. *Trends in Cell Biology*, 26(11):838 – 847. Special Issue: Future of Cell Biology.
* equal contribution

Freikamp, A. and Grashoff, C. (2016). Das kleine Kräftemessen – molekulare Kraftmikroskopie in lebenden Zellen. *BIOspektrum*, 22(1):30–32.

Austen, K.*, Kluger, C.*, **Freikamp, A.***, Chrostek-Grashoff, A., and Grashoff, C. (2013). Chapter 15: *Generation and Analysis of Biosensors to Measure Mechanical Forces Within Cells*, pages 169–184. Humana Press, Totowa, NJ.
* equal contribution

Zink, S., Grosse, L., **Freikamp, A.**, Bänfer, S., Müksch, F., and Jacob, R. (2012). Tubulin detyrosination promotes monolayer formation and apical trafficking in epithelial cells. *Journal of Cell Science*, 125(24):5998–6008.